

**Analysis and Visualization of 3D pore networks in Pleistocene reef cores  
from Shurayrah Island (Al Wajh, N Red Sea)**

Thesis by  
Michael Oyinloye

In Partial Fulfillment of the Requirements  
For the Degree of  
Master of Science

King Abdullah University of Science and Technology  
Thuwal, Kingdom of Saudi Arabia

July, 2021

## **EXAMINATION COMMITTEE PAGE**

The thesis of Michael Oyinloye is approved by the examination committee.

Committee Chairperson: Prof. Abdulkader Alafifi

Committee Members: Prof Volker Vahrenkamp, Prof. Shuyu Sun

© July 2021

Michael Oyinloye  
All Rights Reserved

## **ABSTRACT**

Analysis and Visualization of 3D pore networks in Pleistocene reef cores from Shurayrah  
Island (Al Wajh, N Red Sea)

Michael Oyinloye

### **Motivation for the research and hypothesis tested.**

The characterization of petrophysical properties such as porosity and permeability of carbonate reservoirs for understanding their heterogeneous nature is essential to enhance reservoir modelling and exploration. In the early development stages of carbonate rocks, early diagenesis features fundamental changes in the porosity and permeability systems which will likely yield enormous influence on the subsequent diagenesis, and hence the petrophysical properties of potential limestone reservoirs.

### **Research approach and methods.**

Using petrographic image analysis of thin sections, laboratory measurements of porosity and permeability and x-ray computed tomography (CT) of core plugs and whole core sections, the pore types, pore network and pore connectivity were identified, analyzed and visualized in 2D and 3D.

### **Description of the key results.**

Analyzed x-ray CT scan images reveal the pore types, pore network and pore connectivity in 3D. A separate in-depth facies and diagenesis study using thin section images coupled

with x-ray CT image analysis, shows lithofacies and microfacies types control most of the early diagenesis hence porosity and permeability.

**Significance of the study - why are these results important in carbonate research?**

This thesis hopes to open a pathway to understanding pore and pore throat structures as well as the porosity-permeability relationship in young carbonate rocks before deep burial to enhance reservoir modelling and characterization of analogues.

## ACKNOWLEDGEMENTS

I would like to thank my dear PI Prof. Volker Vahrenkamp for accepting me as his student. Thank you for believing in me. Special thanks to my committee chair, Prof. Abdukadir AlAfifi, and my committee members, Prof Volker and Prof. Shuyu Sun, for their guidance and support to this research.

I will like to thank my family and my late uncle Elder G.S.A Oyinloye for always being supportive and being my motivation in doing more. Thanks to my flatmate, Ryan Maxwell who became my brother, for his supports. My appreciation also goes to my all my friends home and abroad, especially, Oge Chibogu, Ifeoluwa Mibiola, Omolola Alfred, Francis Ajadioni, William Mankata, Ammar Aboalsaud, Teyyuba Adigozolova, Praise Eromosele, Maria Alexandra and Regina Iakusheva who believed that I could achieve this. Special thanks goes to all my colleagues, the department faculty and laboratory staff of ANPERC your support was highly enriching.

I will extend my special appreciation to my ever patient, encouraging and intelligent supervisors, Dr Petrovic Alexander and Dr Viswasanthi Chandra. The period I spent at King Abdullah University of Science and Technology would have been incomplete without their efforts and unwavering supports. I also want to extend my gratitude to the entire Modern Analogues Carbonates Research team, CaResS team and Tojo Chirakal for his invaluable collaborative efforts and the for their unending encouragement and teamwork spirit to see this through. My gratitude goes to my Faith in God, which I hold dear, and to my supportive mentor Prof. Thomas Finkbeiner and his family for always setting the bars high and encouraging me.

## TABLE OF CONTENTS

	Page
<b>EXAMINATION COMMITTEE PAGE .....</b>	<b>2</b>
<b>ABSTRACT .....</b>	<b>4</b>
<b>ACKNOWLEDGEMENTS .....</b>	<b>6</b>
<b>TABLE OF CONTENTS.....</b>	<b>7</b>
<b>LIST OF ABBREVIATIONS .....</b>	<b>9</b>
<b>LIST OF SYMBOLS .....</b>	<b>10</b>
<b>LIST OF FIGURES .....</b>	<b>11</b>
<b>LIST OF TABLES .....</b>	<b>13</b>
<b>Chapter 1: Introduction .....</b>	<b>14</b>
1.1 Porosity and Permeability in limestones and their characteristic heterogeneity.....	14
1.2 Objectives and scopes of the study .....	18
1.3 Structuration of the thesis .....	19
<b>Chapter 2: Geological Setting.....</b>	<b>20</b>
2.1 Environmental and Geological Setting of Al Wajh Platform .....	20
2.1.1 Study Area .....	23
2.2 DIBH006 Core Overview .....	24
2.2.1 Lithofacies Types.....	25
2.2.2 Microfacies Types (MFT).....	28
2.2.3 Diagenesis .....	31
<b>Chapter 3: Methodology.....</b>	<b>33</b>
3.1 Porosity and Permeability Measurements.....	33
3.1.1 Sample preparation .....	33
3.1.2 Pore volume determination.....	35
3.1.3 Permeability determination.....	37
3.2 X-ray Computed Tomography (CT) .....	41
3.2.1 Whole core CT imaging.....	43

3.2.2 Core plug CT imaging .....	44
3.2.3 CT image processing.....	46
<b>Chapter 4: Results.....</b>	<b>53</b>
4.1 Petrophysical measurements.....	53
4.1.1 Porosity .....	53
4.1.2 Permeability .....	53
4.2 Porosity-Permeability relationship.....	55
4.3 CT image Results.....	57
4.3.1 Core and Grayscale images.....	57
4.4 3D Visualization of pores, pore types and pore network models. ....	63
4.4.1 Sample 1 (5.27 – 5.44 m): subsection T, Lithofacies - 2 – Plug 01.....	63
4.4.2 Sample 2 (10 – 10.2 m): subsection T, Lithofacies - 3 – Plug 05.....	66
4.4.3 Sample 3 (13.7 – 10.2 m): subsection L, Lithofacies -4 – Plug 06.....	70
<b>Chapter 5: Discussion.....</b>	<b>73</b>
5.1 Facies vs. Poroperm.....	73
5.2 3D visualization of Pore Types.....	76
5.2.1 Intraparticle and touching vugs porosity (Sample 1 and Sample 2 .....	77
5.2.2 Interparticle - Separate vugs porosity (Sample 3).....	81
5.3 Pore Morphology .....	82
<b>Chapter 6: Conclusions .....</b>	<b>84</b>
<b>REFERENCES.....</b>	<b>86</b>
<b>APPENDICES.....</b>	<b>93</b>
A Image acquisition methodology .....	93
B 3D images of processed CT images of samples from DIBH006 .....	95
C Thin section images of investigated coreplugs (Diameter 2.5 cm).....	98
D Cementation Features (16.1 m) (Chirakal, in prep.) .....	103

## LIST OF ABBREVIATIONS

BHC	Beam hardening correction
COR	Center of rotation
C & P	Choquette and Pray
CT	Computed Tomography
FFT	Fast Fourier Transform
FOV	Field of view
HMC	High magnesium calcite
LFT	Lithofacies Type
LMC	Low magnesium calcite
MFT	Microfacies Type
MIS	Marine Isotope stage
MR	Metarock
PNM	Pore network model
REV	Representative elementary volume
SDD	Subject detector distance
SEM	Scanning electron Microscopy
SOD	Subject object distance

## LIST OF SYMBOLS

- $\mu$  Greek letter Miu characterizes the chemical composition of a material also represent permeability and the unit for micro measurements
- $\epsilon$  Greek letter epselom for characterizing elements of a subset
- $\Phi$  Greek letter fi is used to characterize porosity.
- K latin letter for measuring permeability
- Q latin letter, used to quantify the flow rate at atmospheric condition

## LIST OF FIGURES

Figure 1.1 Sample imaging and quantitative methods for carbonate rocks.....	16
Figure 2.1 The location of the Red Sea.....	22
Figure 2.2 The Al Wajh carbonate platform and the Shurayrah Island.....	23
Figure 2.3 Red Sea sea-level curve extending to the last 400 ka.....	24
Figure 2.4 Lithofacies types (LFT) and fossil abundance trends for DIBH006.....	27
Figure 2.5 Microfacies Types for DIBH006.....	30
Figure 2.6 Thin section showing diagenetic features in core DIBH006.....	32
Figure 3.1 Pore Volume Porosimeter equipment.....	34
Figure 3.2 Helium Porosimeter schematic.....	35
Figure 3.3 Gas Permeameter equipment.....	38
Figure 3.4 Schematic for general gas Permeameters.....	39
Figure 3.5 Principle used in x-ray fluorescence tomography.....	42
Figure 3.6 Schematics for tomographic imaging for the cone-beam setup.....	42
Figure 3.7 X-ray CT Scan Coreholders.....	45
Figure 3.8 Projection images normalization and Center of rotation correction.....	47
Figure 3.9 Center of rotation (COR) correction.....	48
Figure 3.10 Determining optimum Beam Hardening Correction coefficient.....	49
Figure 3.11 Work flow for the image processing and Analysis PerGeos and Avizo.....	51
Figure 4.1 Petrophysical Measurement for DIBH006.....	54
Figure 4.2 Porosity, Permeability vs Facies Types Cross-plots.....	56
Figure 4.3 Core image of lithofacies.....	59
Figure 4.4 Pore and Pore types visualization methodology (5.27 – 5.4 m).....	64
Figure 4.5 Pore space representation of pores segmented subplug from plug 01.....	65
Figure 4.6 Pore size and Pore throat size distribution for plug 01.....	65
Figure 4.7 Pore and pore types visualization methodology (10- 10.20 m).....	68
Figure 4.8 Pore space representation of pores segmented subplug from plug 05.....	69
Figure 4.9 Pore size and pore throat size distribution for DIBH006 plug 05.....	69
Figure 4.10 Pore and Pore types visualization methodology (13.6 – 13.80 m).....	71
Figure 4.11 Pore space representation of pores segmented subplug from plug 05.....	72
Figure 4.12 Pore size and pore throat size distribution for DIBH006 Plug 06.....	72
Figure 5.1 Images of Porites Sp. and Milepora Sp.).....	75
Figure 5.2 3D rendering of Corals (Porites Sp.).....	76
Figure 5.3 3D cross section of investigated core plugs showing porosity.....	77
Figure 5.4 Sample 1 (plug 1) showing the internal structure of Corals ( <i>Porites Sp.</i> ).....	79
Figure 5.5 Sample 2 (plug 2) showing the internal structure of Corals ( <i>Millepora Sp.</i> )...	80
Figure 5.6 Pore morphology.....	81
Figure 5.7 Pore shapes and interconnectivity.....	83
Figure A.1 General X-ray Imaging window in Acquila.....	93
Figure A.2 CoreTOM Hardware Filters.....	94
Figure B.1 Pore structure and pore connectivity at 16.90 m.....	95
Figure B.2 Pore structure and effective connectivity simulation of subplug (16.90 m)...	95
Figure B.3 Pore radius distribution for plug at 16.90 m.....	96
Figure B.4 Pore shapefactor distribution for plug at 16.90 m.....	96

Figure B.5 Multiscale pore imaging of core section 5.75 m.....97  
Figure C Thin section images of investigated coreplugs.....98  
Figure D Cementation features .....103

**LIST OF TABLES**

Table 3.1 Acquisition parameters for whole core CT images.....	44
Table 3.2 Acquisition parameters for core plug CT images .....	46
Table 4.1 Numerical porosimetry of Plug sample.....	66
Table D.1 Diagenetic features from thin section analysis.....	104

## **Chapter 1**

### **Introduction**

#### **1.1 Porosity and Permeability in limestones and their characteristic heterogeneity**

Modern carbonate platforms have been extensively studied over the last few decades for the understanding of their spatial and petrophysical heterogeneities (Betzler & Eberli, 2019; Gischler et al., 2013; Reijmer et al., 2015; Purkis et al., 2015; Grammer et al., 2001). These studies have been used as analogues for better reservoir modelling and characterization. The Red Sea is characterized by such modern carbonate platforms on its margins (Montaggioni et al., 1986) and has been a location for continuous research.

Porosity, permeability and pore characteristics are among the primary factors driving fluid flow in the subsurface. Their quantification and description have a tremendous impact on reservoir characterization (Lucia, 1983; Antonellini & Aydin, 1994; Lucia, 1995), which directly influences exploration methods, development strategies, and petroleum economics (Shouxiang Ma, 1996; Yang & Aplin, 2007; Taslimi et al., 2008). However, due to their dominantly biological origin, and their high sensitivity to diagenetic alterations, carbonate reservoirs are often characterized by a high degree of petrophysical and pore network heterogeneities (e.g. Algive et al., 2012). This is manifested in a wide range of pore shapes and geometries that can appear in carbonates (e.g. Choquette & Prey, 1970; Lucia, 1995). Several studies have shown that the initial composition (mineralogy) and fabric of deposited sediments control primary porosity formation while the variability in the sea

level with time and other diagenetic factors are the main drivers controlling secondary pore formation/destruction, and connectivity in limestone successions (Harbaugh, 1967; Choquette & Pray, 1970).

Different techniques are used nowadays to characterize pores and pore networks in carbonate rocks, in order to understand the geometrical and topological representation of their internal and external pore structures (Vergés et al., 2011). They are ranging from standard methods such as visual inspection at the outcrop (Fig. 1.1A) to 2D thin section analysis using light microscopy (Fig. 1.1B) (Leighton & Pendexter, 1962), to 3D scanning electron microscopy (SEM) (Wang & Sun, 2021) and analytical methods like mercury injection capillary pressure (MICP) (Theologou et al., 2015; Rios et al., 2015) (see Fig. 1.1). More advanced imaging and quantification techniques are; focused ion beam scanned electron microscopy (FIB-SEM) (Sok et al., 2010), confocal laser scanning microscopy (CLSM) (Hassan et al., 2017; Hassan et al., 2020), (see Fig. 1.1). One of the most widely used methods for pore network visualization is high-resolution 3D computed tomography (up to micron scale) for digital rock imaging using x-rays. This method has proven to have advantages over the enumerated previous methods such as improved recovery processes, fluid flow modeling and wettability evaluation and core log reconciliation (Flannery et al., 1987; Hall et al., 2017; Blunt et al., 2013; Blunt, 2017). Other advantages of the x-ray tomographic imaging method for carbonate rocks are summarized by Jing et al. (2017) and Blunt et al. (2013), such as the possibility to visualize pores and pore networks in three dimension. The acquired data help in deriving and understanding petrophysical properties such as the shape factor, coordination number of the pores and other multiphase flow properties of the imaged carbonate rock. The acquired data can also be used for predictive

pore scale modelling for better understanding of the subsurface flow properties (Hazlett, 1995). The effects of rock structure on the relationship between porosity and permeability in carbonate rock formations have been widely reported in published studies (Chandra et al., 2015; J.-B. Regnet et al., 2015; El Husseiny & Vanorio, 2017; J. B. Regnet et al., 2019; Chandra et al., 2021). Algive et al., (2012) extensively discussed the impact of diagenetic alterations on the petrophysical and flow properties of carbonate rocks.

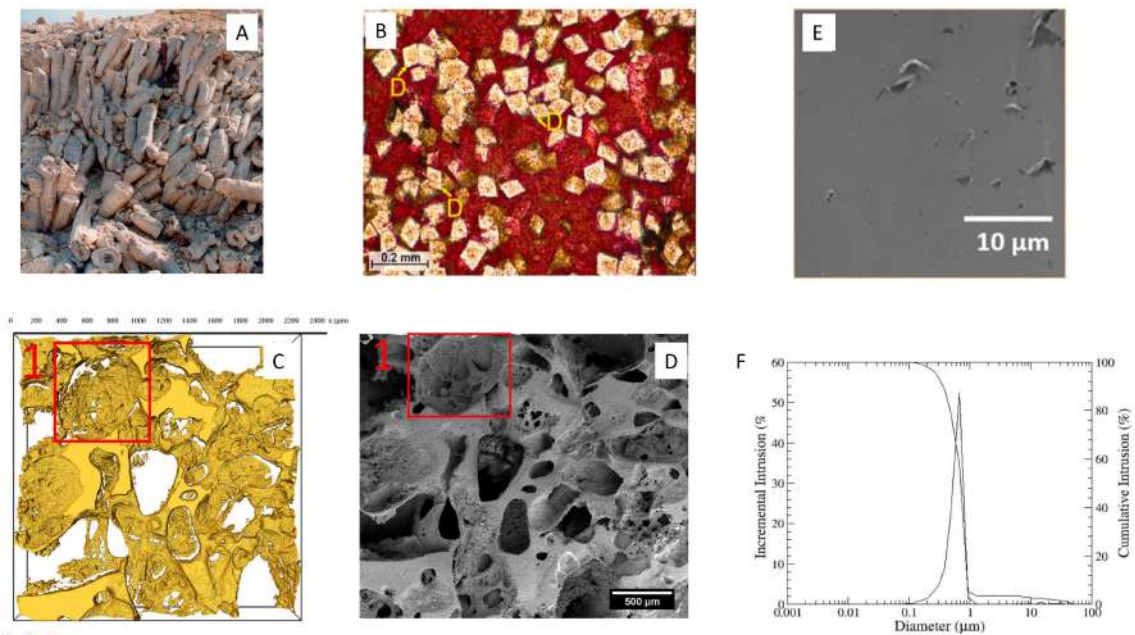


Figure 1.1- Sample imaging and quantitative methods for carbonate rocks : (A) Outcrop image of rudists from a Late Cretaceous reef in Oman (Flügel, 2010). (B) Image of a thin section from an optical microscope showing rhombic dolomite crystals in a carbonate mudstone (Chandra et al., 2021). Pore cast CLSM (C) and SEM (D) images of an Indiana limestone (Hassan et al., 2017). (E) FIB-SEM image of a dolomite thin section. (F) MICP plot for a carbonate mudstone (Sok et al., 2010).

Porosity and permeability have a general trend of reduction with depth (Halley & Schmoker, 1983). Most reservoirs with abundant petrophysical data are located at depths

below 2 km (Ehrenberg et al., 2009). The petrophysical properties of young limestone layers however, are understudied.

In order to investigate the pore-network development during early diagenesis, this thesis aims to study the pore network of a 17 m reefal core of Late Pleistocene (MIS5e) age. The analyzed core (DIBH006) originates from the central part of a carbonate island (Shuraya Island) that is located within the modern Al Wajh carbonate platform lagoon, NE Red Sea. Al Wajh platform is a modern analogue for a land-attached rimmed carbonate platform in a rift basin (Wright, 1996; Bosence, 2005). The platform is situated in the northern Red sea in a hot, arid climate. Present day precipitation rates are low (about 16 – 70 mm/yr) and preventing any significant influx of siliciclastics through rivers (Riegl et al., 2012; Sheppard et al., 1992). However, since the deposition of this sediments in the late Pleistocene, several pluvial periods have been proposed (Burns et al., 2001; Fleitmann et al., 2011; Nicholson et al., 2020). The late Pleistocene reefal carbonate sequences deposited during the last interglacial sea-level highstand (MIS5e), represent an excellent example to investigate early stage pore network development formed under dominantly arid conditions. Within these temporary pluvial periods (Burns et al., 2001; Fleitmann et al., 2011; Nicholson et al., 2020) the impact of exposure during the sea level lowstand of the last glacial period can also be studied. In comparison, most of the previous studies with focus on pore networks in Pleistocene rocks were carried out in humid to tropical zones (Vollbrecht & Meischner, 1993; Melim et al., 1995; Jones & Pemberton, 1988; Liu et al., 2019; Harris & Purkis, 2020).

The objectives and scope of this thesis are further elaborated in the following section.

## 1.2 Objectives and scopes of the study

The aim of this study is to improve the understanding of early pore network development of Late Pleistocene carbonate island reef rocks under dominantly arid conditions with intermittent pluvial periods.

These objectives will be achieved by:

- A quantification of the porosity and permeability of the carbonate core DIBH006 using standardized laboratory equipment; porosimeters and permeameters, as well as digital evaluation of CT data using industry software including AVIZO and PerGeos.
- The visualization and analysis the 3D pore network of the selected core (DIBH006) and high resolution images from the core plugs
- The establishment of a workflow for CT image acquisition and processing for carbonate rock samples;
- The investigation, identification and understanding of the main primary depositional and diagenetic factors controlling the petrophysical properties (porosity and permeability) of the selected core from the Al Wajh carbonate platform. This aspect of the study has been conducted in collaboration with MS candidate Tojo Chirakal from the University of Tübingen.

### **1.3 Structuration of the thesis**

#### **Chapter 2: Geological setting**

The section focuses on the description of the environmental and geologic setting of the investigated area as well as the overview of the investigated core.

#### **Chapter 3: Methodology**

This section presents the detailed protocols and standardized methodology for the Al Wajh platform's data collection, processing and analysis of obtained results.

#### **Chapter 4 : Results**

This chapter shows all the obtained, processed and analyzed results from petrographic images of 28 thin sections, laboratory measured porosity and permeability of 38 core plugs and acquired CT data of whole core sections and core plugs.

#### **Chapter 5: Discussion**

This chapter elaborates, discusses and derived conclusion from the observed trends in the presented and processed results of the petrophysical measurement of 28 plugs, petrographic images of 28 thinsections, 2D and 3D renderings of processed and analyzed CT images.

#### **Chapter 6: Conclusion**

This chapter summarizes the main findings from the analysis and discussion of the results from the preceding chapter.

## Chapter 2

### Geological Setting

#### 2.1 Environmental and Geological Setting of Al Wajh Platform

The Red Sea is a 2000 km elongated body of water spanning across a 355 km maximum width and maximum depth of about 3 km (Touliabah et al., 2010), resulting from the continental rifting of the African and Arabian plate margins (Martinez & Cochran, 1988). Rich in thousands of islands, shoals and lagoons, the Red Sea is bounded by nine countries (Fig. 2.1) (Rasul et al., 2015). Located in the northeastern part of the Red Sea, Al Wajh is a land-attached and nearly rectangular carbonate platform that has a length of around 55 km at the ocean-facing side (70 km at the coast). The platform has a width of 30 km in the NW and 23 km in the SW (Fig. 2.2A). The platform is almost completely rimmed by a coral reef belt (Rowlands et al., 2012). Water flow across the reef rim and three inlet channels connect the lagoon to the deep sea and facilitate water exchange between the open sea and the lagoon. The main inlet channel is approximately 400 m wide and divides the platform into northern and southern parts (Fig. 2.2A). The platform's interior is characterized by carbonate islands, patch reefs, and a deep lagoon (max. -42 m; Fig. 1.5A), while the shoreline is dominated by gravel to sand-sized siliciclastics (Petrovic et al., accepted). The modern platform is shaped by the carbonates grown during the late Pleistocene (MIS5e) sea-level high stand, when the sea level was about 9 m above present day (Strasser et al., 1992; Manaa et al., 2016; Evan et. al., 2021). Most of the former MIS5e reefs nowadays form elevated terraces on carbonate islands on the outer rim and in the

lagoon. Since deposition they experienced a prolonged period of exposure during the sea-level low stand associated with the last glaciation and reflooding to modern sealevel during the subsequent Holocene sea-level rise 9 (Fig 2.3).

Al Wajh is situated in an arid climate condition with precipitation rates less than 70 mm/yr (Sheppard et al., 1992; Riegl et al., 2012). Evaporation rate is higher than the net annual precipitation by 2 m (Hamylton, 2012). Water surface temperature ranges from 22°C in the winter to about 32°C in summer (Yao et al., 2014). This makes the Red Sea one of the world's warmest and most saline (35 psu) water bodies. Similar to the Red Sea, the predominant wind direction in the Al Wajh area is the northwest. These strong northwest winds are sourced from the Eastern Mediterranean and are often occasionally extended reaching the south (Langodan et al., 2017; Bruckner et al., 2013). The winds are also alternated seasonally coming from the Northwest during the Northeast monsoon to coming from the south southeast during the Southwest monsoon (Jiang et al., 2009). These winds generate significant waves up to 2 m in height (Langodan et al., 2016) which are major factors affecting sedimentation and sediments distribution on the platform (Petrovic et al., (accepted). Wind speeds ranges from 7-13 km/hr and occasionally, streams of westward wind generated by land-sea breezes (Langodan et al., 2016) jet through the valleys and mountain gaps on the northeastern margin of the Red Sea. These westward winds occur during winter (November –March) and blow into the platform carrying significant quantities of dust plumes ((Jiang et al., 2009). Storm activities are observed though minimally for the Al Wajh area (Manaa et al., 2016). The 24hr cycle tide observation of the Northern Red Sea is about 0.6 m (Bruckner et al., 2013).

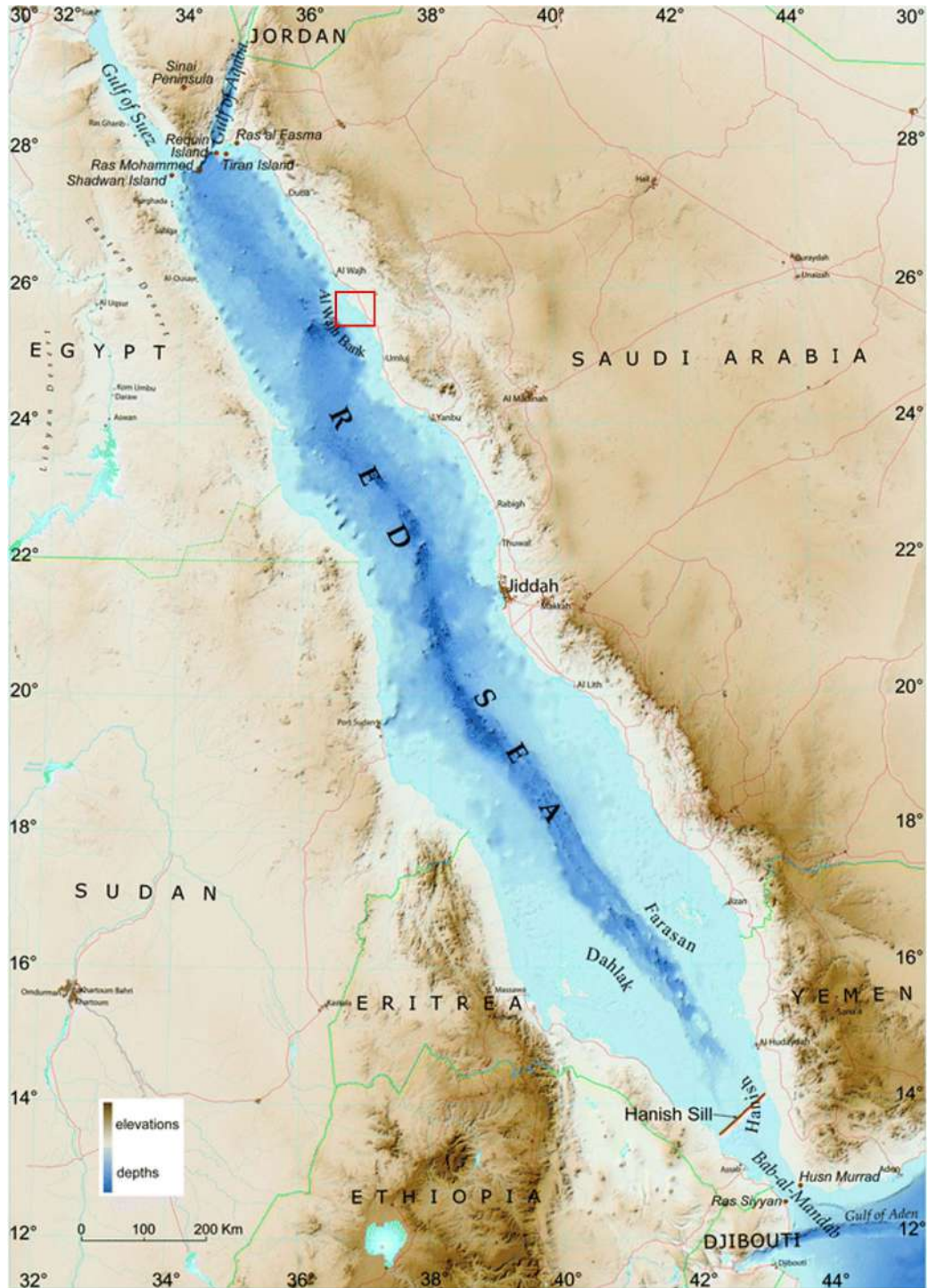


Figure 2.1 - The Red Sea is located between Africa and the Arabian Peninsula. The Red box marks the location of Al Wahj carbonate platform (Rasul et al., 2015).

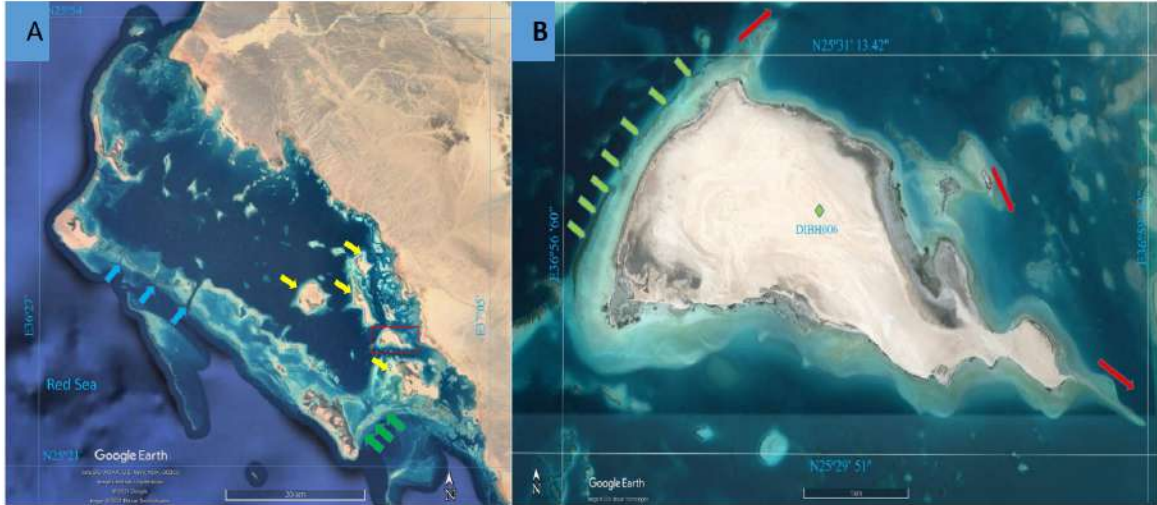


Figure 2.2 - The Al Wajh carbonate platform and the Shurayrah Island (Red box). The yellow arrows indicate main islands in the southern part of the platform; the green arrows shows the sand shoals deposits and the blue arrow shows the main in-let channels. (B)

Location of core DIBH006 on Shurayrah Island (Green diamond). The Island is characterized by a large reef towards the Northwestern section (Green arrows), and island spits (Red arrows) indicating the dominant wind direction. (*Modified GoogleEarth images*)

### 2.1.1 Study Area

The investigated core DIBH006 was drilled at the central part of Shurayrah Island (Fig. 2.2B). The carbonate island is located in the southeastern inner lagoon of the Al Wajh carbonate platform (Petrovic et al., accepted) and was formed during the MIS5e sea-level highstand (Manaa et al., 2016). Shurayrah Island has an approximate size of 3 km by 4 km covered with unconsolidated sediments of about 5 m of vertical elevation. It is characterized by barrier reefs to the northwest, and sediment spits to the southeast indicating the dominant regional wind direction (Fig 2.2B) from the northwest (Rasul et al., (2015) and Yao et al., (2014) .

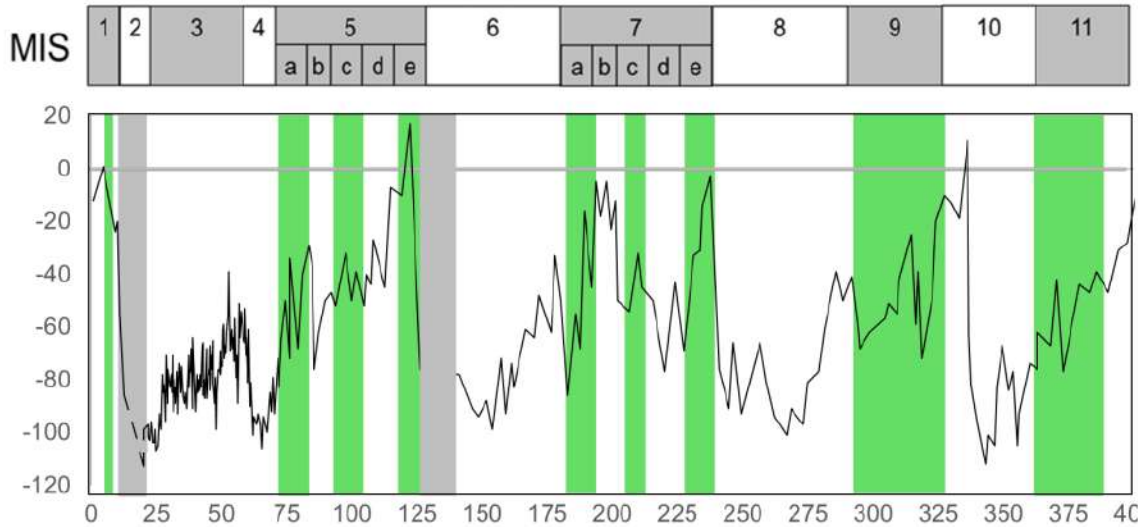


Figure 2.3 - Red Sea sea-level curve extending to the last 400 ka. Marine Isotope stages (MIS) are shown in the top image. The vertical green bars represent humid periods according to (Nicholson et al., 2020) indicating that the MIS5e limestones which are the subject of this study have been exposed for most of their existence and experienced three humid periods with rainfall and fresh-water diagenesis.

*(Image modified by PhD candidate Indah Perbawa)*

## 2.2 DIBH006 Core Overview

The limestone core DIBH006 contains discontinuous fossiliferous sections of coral fragments, coralline red algae, gastropods, bivalves and shows evidence of bioturbation (Fig. 2.4). Coralline Red algae encrustations are observed all through the core. The core can be divided into three sub-sections: Top (T), Center (C) and Lower (L) (Fig. 2.4H). Section L is characterized by an abundance of red algae and bivalve shell fragments, which decreases towards the top. Section C contains coral fragments, bivalve shells and a higher amount of coralline red algae in comparison with the other identified fossils. The upper section T, is characterized by an abundance of coral fragments. Detailed petrographic thin section analysis by MS candidate Tojo Chirakal (University of Tuebingen) point to a

dominantly high magnesium calcite (HMC) and low magnesium calcite (LMC) mineralogy, accompanied by a minor occurrence of aragonite needles.

### 2.2.1 Lithofacies Types

Based on the component assemblages, seven lithofacies (Fig. 2.4A-G) have been identified; Bioclastic wackestones – packstones (LFT1), Coral Rudstones (LFT2), Bioclastic floatstone- rudstones (LFT3), Coral Floatstone-rudstone (LFT4), Red Algae bindstone (LFT5), Coral framestone (LFT6), algae-coral framestones (LFT7), and The depositional environment is interpreted to represent a backreef area of a barrier reef.

*Bioclastic wackestones – Packstones (LFT1)*: This facies occurs dominantly in the subsections C (6.5 m) to T (8.1 m, 9.5 m and 12.5 m) and is characterized by bioclasts (e.g. mollusks shells) intraclasts of coral and RA fragments, and is minorly bioturbated. The facies is dominated by interparticle porosity (Fig. 2.4A).

*Coral Rudstones (LFT2)*: the facies occurs only in section T at depths of 7.5 m and contain mostly of poorly sorted coral fragments that are common thinly encrusted by RA (Fig 2.4B). The facies shows dominantly interparticle and intraparticle porosity.

*Coral Floatstone-Rudstone (LFT3)*: This facies occurs in section T between 8.2 - 8.5 m and is composed of corals fragments thinly encrusted by RA (Fig 2.4C). Moldic vuggy porosity related to leaching of aragonitic corals characterizing this facies.

*Coral – Red Algae Floatstone – Rudstone (LFT4)*: Characterized by coral fragments, thick crusted rhodolites and strong bioturbations, this facies occur in the subsection C between 11 - 12 m. The facies shows dominantly interparticle porosity (Fig. 2.4D).

*Red Algae Bindstone (LFT5)*: The facies occurs in subsection L between 15.5 and 16.9 m depth, and is dominated by fracture porosity. Coralline red algae, benthic forams (milliolid), minor shells and corals are characterizing this facies (Fig 2.4E).

*Coral Framestone (LFT6)*: The facies occurs in section C at around 13 m. This facies is predominantly characterized by large frames of coral fragments (up to 6 cm in length) that are encrusted by red algae (RA). Fragments of RA and sediment filling of cavities is also observed (Fig. 2.4F). This facies are predominantly show interparticle and intraparticle porosity.

*Bioclastic floatstone-Rudstone (LFT7)*: This facies occurs in the subsection C at 12.6 - 13.2 m (Fig. 2.4G). Dominated by excessively leached mollusk shell fragments (mostly bivalves) forming moldic porosity.

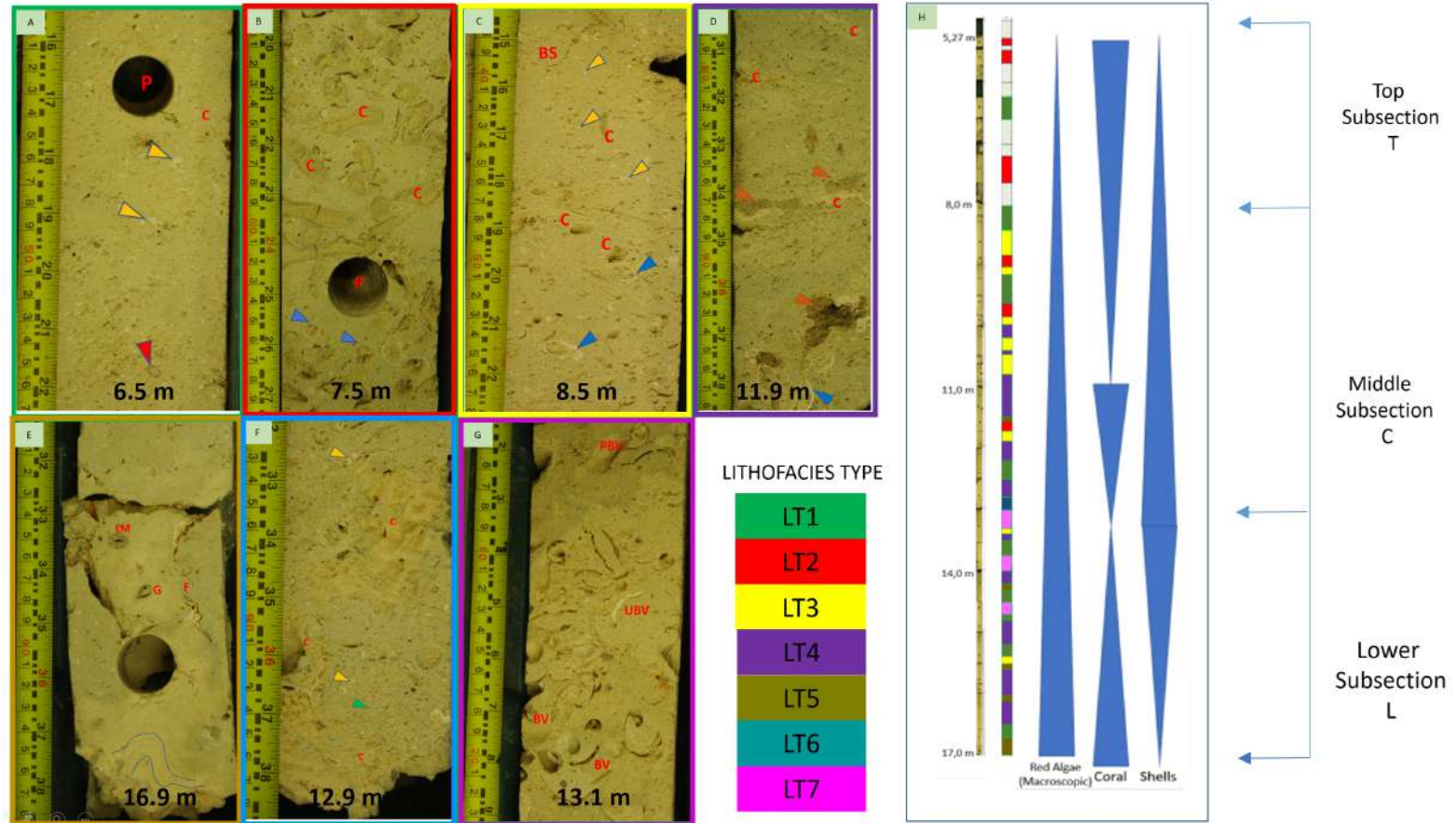


Figure 2.4 - Lithofacies types (LFT) and fossil abundance trends for DIBH006. A) Bioclastic wackestone – grainstone (LFT1). B) Coral Rudstone (LFT2). C) Coral floatstone – Rudstone (LFT3). D) Coral – Red algae floatstone-rudstone (LFT4). E) Red algae Bindstone (LFT5). F) Coral Framestone (LFT6). G) Bioclastic floatstone – Rudstone (LFT7). H) Core image and facie distribution including abundance trends for corals, red algae and shells along the core. C – Coral P – Plug hole, BS – Bivalve shell, LM – Large Milliolid, G – Gastropod, F – Fracture, BV – Bivalve shell, UBV – Undissolved bivalve shell, PBV – Partially dissolved bivalve shell. (Orange triangles indicate Red algae fragments, blue triangles indicate red algae coral encrustation, red triangle indicate bioclasts, brown triangle indicate bioturbation, green triangles indicate sediment filling and wavy lines indicate lamination of red algae (Rhodolith). (Courtesy Tojo Chirakal, University of Tübingen)

### 2.2.2 Microfacies Types (MFT)

Five main microfacies types were identified based on the microfacies types defined by Chirakal, et al (in prep.): Porites Framestone (MFT2), Encrusted sediments covered coral framestone (MFT3), Encrusted coral rudstone (MFT4), Encrusted coral framestone (MFT5), Bioclastic packstone (MFT11).

*Porites framestone (MFT2):* This MFT contains mainly organic rigid coral frameworks with a calcitic mineralogy, and occurs only in subsection L at 16.9 m depths (Fig. 2.5A-B). It dominated by touching vug porosity (F Jerry Lucia, 1995) or growth framework porosity according to, Choquette and Pray (1970)

*Encrusted sediments covered coral framestone (MFT3):* . This MFT occurs in subsection T and C at depth ranging from 5 - 6 m, 11 – 12 m and 13 m. This MFT is characterized by corals (porites sp.), coralline red algae, bivalves, benthic forams, echinoidal spines, bryozoans, ostracods and barnacles (Fig 2.5C-D). It has a dominantly calcitic mineralogy with a low aragonitic and quartz content (<1%). The matrix has grain sizes ranging from 0.01 - 2 mm and are very poorly sorted. It is dominated by touching vugs porosity.

*Encrusted coral Rudstone (MFT4):* The facies occurs in the in all sections of the core. This facies is characterized by corals (Merulinidae , Porites sp.), coralline red algae, benthic foraminifera, ostracods, barnacles, bryozoans and echinoid spines. Mineralogy is dominantly calcitic and very limited aragonite and quartz content (<1%). It is strongly bioturbated and poorly sorted, while the dominant grain size is > 2 mm (Fig. 2.5E-F). The dominated by interparticle, separate and touching vugs porosity.

*Encrusted coral framestone (MFT5)*: This MFT occurs in all subsection but mostly in the subsection L. This MFT contains coralline red algae, benthic foraminifera, ostracods, barnacles, bryozoans and echinoid spines. The dominant matrix grain size is  $> 2\text{mm}$ , while the sediment is poorly sorted and rarely bioturbated. Grains are often encrusted by red algae. Mineralogy is mainly calcitic with very few aragonitic and quartz ( $<1\%$ ) content (Fig. 2.5G-H). It is dominated by touching vugs porosity.

*Bioclastic Packstone (MFT11)*: The facies occurs in subsection C at 12.4m and 13.9 m depth. This MFT contains mainly bioclastic detritus of unknown origin and include benthic forams, bryozoans, gastropod shells, bivalve shell fragments, echinoid spines and encrusting coralline red algae (Fig 2.5I-J) which range from loose to dense packing. It is a grain dominated and bioturbated packstone with grain sizes ranging from 0.01 – 1.9 mm and are very poorly sorted. The mineralogy is calcitic and aragonitic.

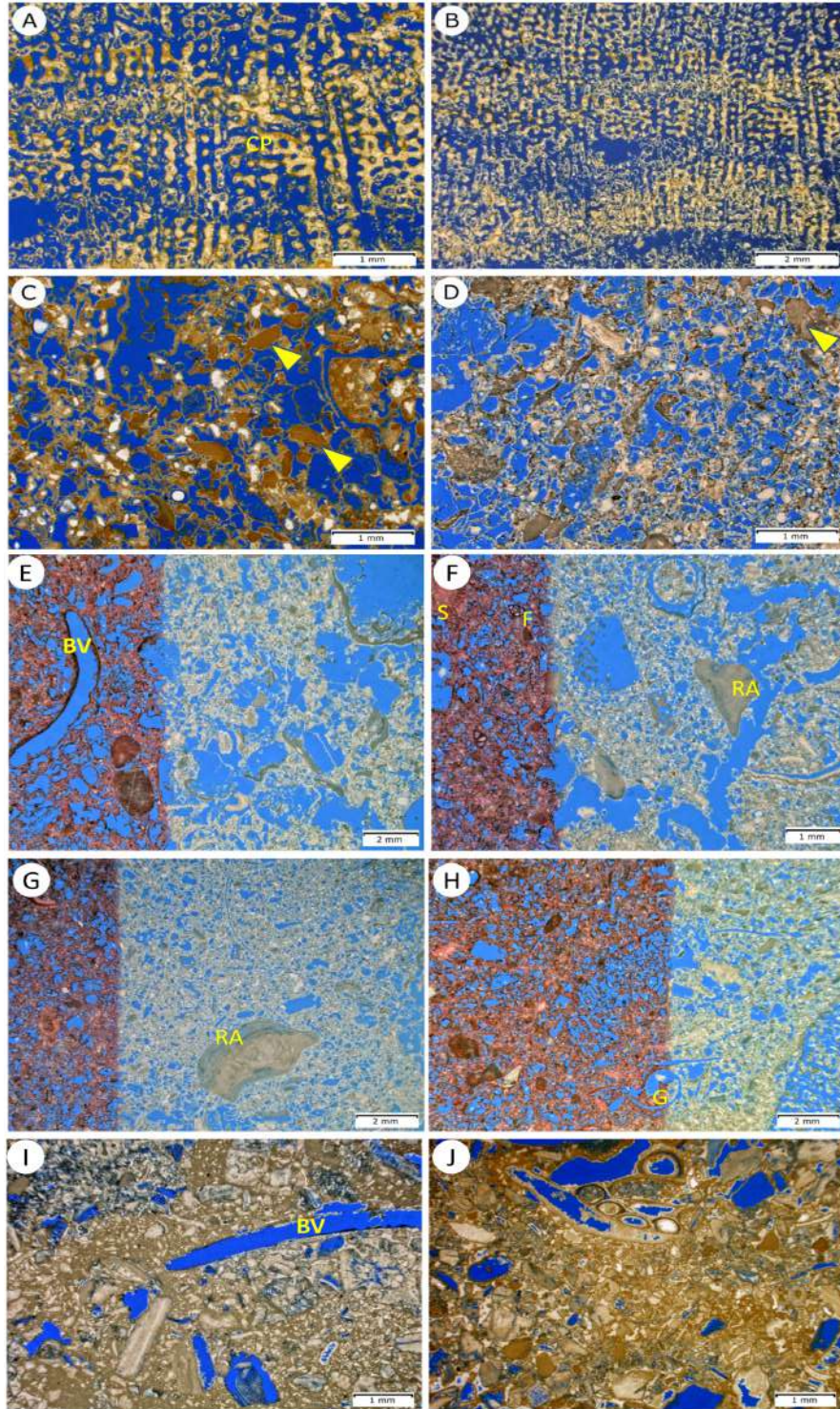


Figure 2.5 - Thinsections of Microfacies Types for DIBH006 (porosity in blue). A & B (MFT2) represent Porites framestone showing rigid coral skeletal framework. C & D (MFT3) – Encrusted sediments covered coral framestone showing sediments filling. E & F (MFT4) – Encrusted coral rudstone showing partially dissolved coral fragment. G & H (MFT5) – Encrusted coral framestone showing coralline red algae and its distinctive irregular shape. I & J (MFT11) - Bioclastic Packstone showing grain dominated matrix with high cementation. CP – Corals *Porites* sp., BV – Bivalve, RA – coralline red algae, S – Echinoid spine, F – Benthic Forams, and Triangles indicating sediments filling. (Courtesy of Tojo Chirakal, University of Tübingen)

### 2.2.3 Diagenesis

As established in 1.2.1 and 1.4 according to the climate data and the result of the above lithofacies and microfacies' description based on (Chirakal et al in prep), the paragenetic sequence is as follows: The deposited carbonate sediments underwent micritization during the MIS 5e sea level highstand during which the platform was flooded. Precipitation of aragonitic fibrous cements and subsequently bladed cements occurred shortly after.

After MIS5e, sea level decreased significantly until it reached its lowest level (-120 m) during the Last Glacial Maximum, while this period was accompanied by humid periods in MIS5a and c (Nicholson et al., 2020). As a consequence, the studied reef was exposed, leading to phreatic meteoric diagenetic sequence including dissolution of aragonitic components and the formation of equant and drusy calcite cements (dogthooth). During the glacial period (MIS2) (Siddall et al., 2003), the climate was arid hence, there is a limited vadose meteoric diagenetic impact on the studied reef and the formation of meniscus cements and geopetal imprints. The platform was flooded again during the Holocene MIS1 sea-level highstand leading to the formation of secondary marine bladed cements (Fig. 2.6).

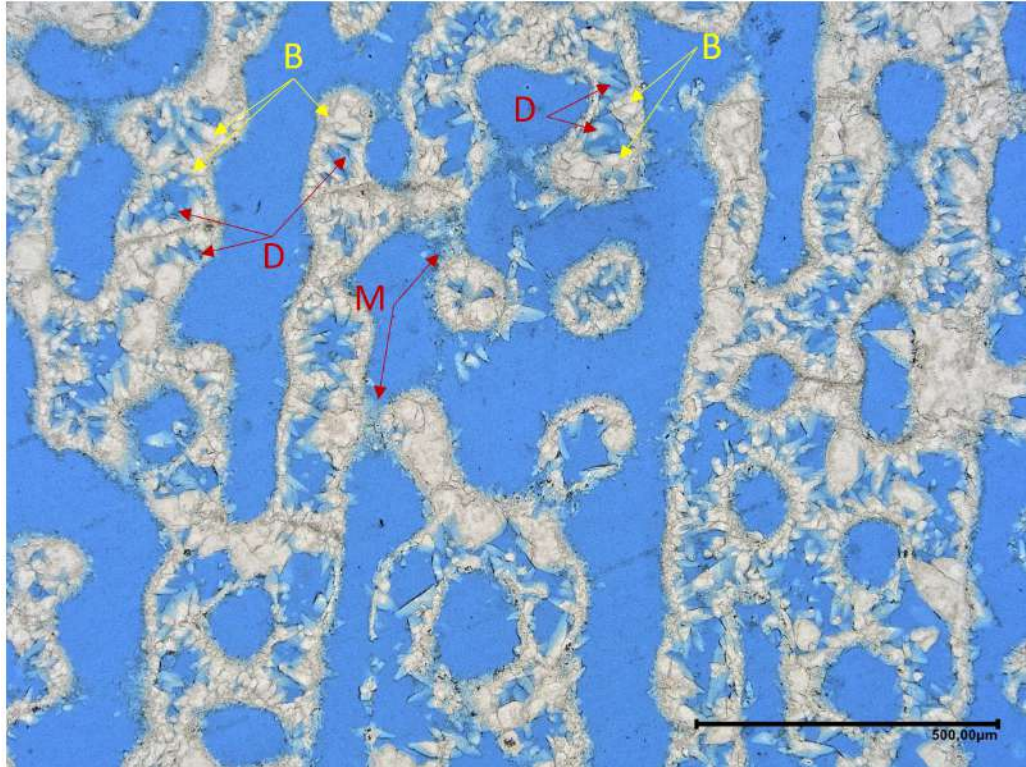


Figure 2.6 - Thin section showing diagenetic features in core DIBH006. The image shows secondary bladed cements overlaying dogtooth cements. *B* – bladed cements, *D* – dogtooth cement, *M*- meniscus cements. (Image Courtesy, Tojo Chirakal)

## **Chapter 3**

### **Methodology**

The primary material used in this study was a 17 m long Late Pleistocene carbonate core, namely DIBH006, from the Shurayrah Island (Al Wajh platform). 28 one-inch diameter core plugs and 54 thin sections for petrographic imaging and analysis were obtained from the trim ends of the drilled core plugs. Petrophysical properties including porosity and permeability of the plugs were measured using a helium porosimeter (MR PDP-300 systems) and a multi-cell cleaning system and gas permeameter, respectively. X-ray Micro CT scanning was done for whole core sections and core plug using Tescan's CoreTOM CT scanner. The image acquisition and reconstruction was done with Tescan's Acquila™ software. Image processing and analysis workflows were executed with AVIZO™, PerGeos™ and Panthera™ software.

### **3.1 Porosity and Permeability Measurements**

#### **3.1.1 Sample preparation**

The samples selected for the measurement were thoroughly cleaned and oven dried to remove all fluids. The shape of the sample is very critical and important, hence, the sample should be very regular to reduce errors in the pore volume calculation and increase accuracy of the porosity data. The topology of the plug samples used was made as close as possible to a perfect cylindrical shape using the Struers Discoplan -TS and the CSG-618 Manual hand feed milling instrument.

The diameter (cm) and length (cm) of each sample was measured using a digital Vernier caliper while the weight (g) was determined using a Metler Toledo MS204S digital weighing scale with a 0.1 milligram precision. The sample was placed in an autoclave (Loading model 100-800) for 10-30 minutes at a temperature of 40° C to evaporate any remaining fluids.



Figure 3.1 - Pore Volume Porosimeter equipment. A) Metarock PDP-300 porosimeters, B) corresponding one inch diameter core plug holder (matrix cup) for holding and confining plug samples, C) one inch diameter steel billets of standardized and predetermined weights for filling unoccupied spaces by plugs.

*(Courtesy ANPERC labs, KAUST).*

### 3.1.2 Pore volume determination

Helium-gas porosities of the plugs were measured using a twin cell porosimeter (MR-PDP-300 systems, Fig. 3.1A). Generally, porosity ( $\phi$ ) is calculated using the equation (3.1) below as a ratio between volumes. Hence, it is dimensionless or expressed in percentages:

$$\Phi = \frac{V_p}{V_b} = c = \frac{V_p}{V_p + V_g}; \quad (3.1)$$

$V_b$  is the bulk volume of the sample,  $V_p$  and  $V_g$  are the pore volume and grain volume respectively (McPhee et al., 2015). The porosimeter calculates the pore space volume using Boyle's law for ideal gas, which means the product of the pressure and the volume of the gas in a closed system is constant assuming constant temperature.

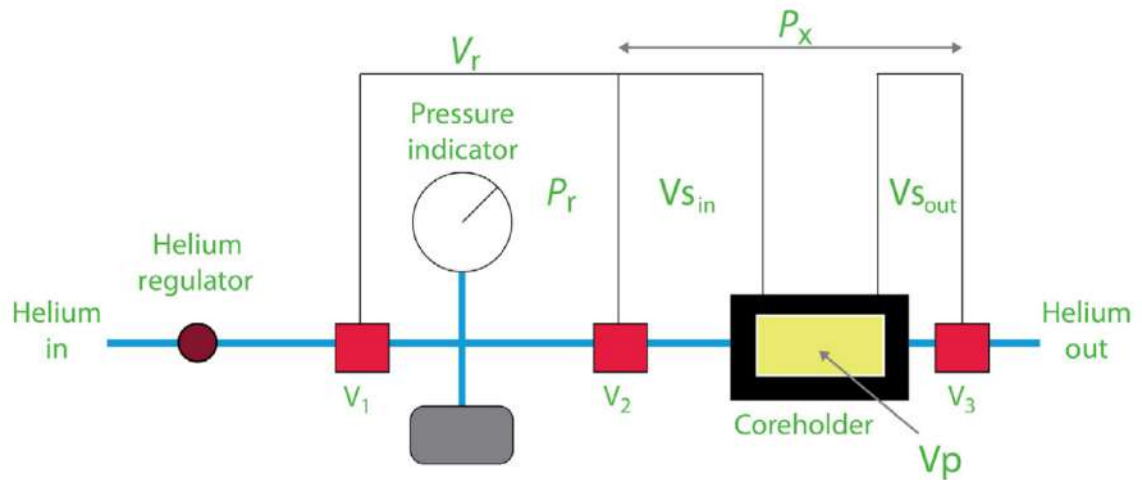


Figure 3.2 - Helium Porosimeter schematic (McPhee et al., 2015).

$$P_1 V_1 = P_2 V_2 = \dots P_n V_n, n \in \mathbb{R}; \quad (3.2)$$

Where  $P_1$  and  $P_2$  are initial and final pressures and  $R$  is any real number

According to Figure 3.2, we can re write the equation as ;

$$P_r V_r = P_x (V_r + V_{s_{in}} + V_{s_{out}} + V_p) ; \quad (3.3)$$

The equation can further be re-written as given below to calculate the pore volume  $V_p$ :

$$V_p = \frac{P_r V_r}{P_x} - V_r + V_{s_{in}} + V_{s_{out}} = \frac{P_r V_r - P_x (V_r + V_{s_{in}} + V_{s_{out}})}{P_x} ; \quad (3.4)$$

Where  $V_p$ ,  $V_r$ ,  $V_{s_{in}}$  and  $V_{s_{out}}$  are the pore volume, the reference volume, volume at the inlet to the matrix cup and volume exiting the matrix cup respectively.  $P_r$  is the reference pressure and  $P_x$  is the final expanded pressure.

The plug was placed into a matrix cup (Fig 3.1B) and billets of known volumes were placed in the cup to fill up the spaces unfilled by the plug. Air in the system was removed by vacuuming the matrix cup and passing helium gas through to flush out the residual air. The matrix cup was inserted and confined, leading to the closure of valves V2 and V3. All parameters were cross examined to confirm the functionality of each component of the porosimeter. The pressure was set to 100 psi and valve V1 was opened so helium was passed into the matrix cup at the set pressure. Helium gas was allowed to expand in the coreholder by opening valve V2 (closing V3 and V1), while monitoring the expanded pressure until stability is attained. Depending on the permeability of the plugs, the stability time can vary from a few seconds to tens of minutes. The device determines the pore volume automatically after obtaining  $V_p$  and solving equation (3.1). The porosity measured at the pressure stability point is the final porosity measurement of the plug..

### 3.1.3 Permeability determination

Absolute permeability of the plugs were measured using a Metarock SSK-400 Gas permeameter and a Metarock (MR) Multi-cell system (Fig. 3.3A-B). Permeability ( $k$ ) is determined according to Darcy's fluid flow equation for incompressible fluids (Dejam et al., 2017) written below;

$$Q = \frac{kA(P_1 - P_2)}{\mu L}; \quad (3.5)$$

Darcy's equation can be re-written in terms of  $k$ , the permeability in equation 2.6

$$k = \frac{QA\mu L}{(P_1 - P_2)}; \quad (3.6)$$

Permeability is measured in Darcy ( $10^{-12} \text{ m}^2$ ).  $A$  is the cross sectional area ( $\text{cm}^2$ ) of the sample,  $P_1$  and  $P_2$  are the initial and final pressures (atm),  $\mu$  (cP) is the viscosity of the permeating fluid,  $L$  is the length of the sample (cm), and  $Q$  ( $\text{cm}^3/\text{s}$ ) is the rate of flow of the permeating fluid).

Figure 3.3 - 3.4 show the main components of all gas permeameters which include, a coreholder that can be confined with endcaps and sleeves for sample. This couple is also called Hassler cell (Fig. 3.3C- D). The endcaps have thin holes for inlet ( $P_1$  measurement) and outlet ( $P_2$  measurement) of the permeating gas. The sample, when placed in the sleeve and into the coreholder, is confined at isostatic loading conditions to prevent the gas from flowing outside the sleeve. The system must have a pressure source or pump to apply pneumatic or hydraulic pressure. Further, the system must also be equipped with pressure control gauges and pressure indicator gauges. Pressure gauges and indicator will measure and control the inlet and outlet pressures individually. The system must consist flow gauges

for a wide range of rates, thermocouple for the temperature of the gas and barometer (Pa) to measure atmospheric conditions during the measurements.



Figure 3.3 - Gas Permeameter equipment. A) Multi-cell cleaning system with 10 cells for operation. B) MR SSK-400 permeameters showing the teflon gas flow lines. C) The core holder showing the top and bottom lids. D) End caps and plug sleeve.

*(Courtesy of ANPERC labs)*

If the experiment is conducted at atmospheric pressure  $P_a$ , the flow rate  $Q_m$  measured is determined by;

$$Q_m = \frac{Q_a P_a}{P_m}; \quad (3.7)$$

$Q_a$  is the flow rate at atmospheric condition,  $P_m$  is the mean pressure  $(P_1 - P_2/2)$ . If the experiment is not measured at atmospheric conditions at an inlet pressure  $P_1$ , the flow rate  $Q_m$  measured is determined by;

$$Q_m = \frac{Q_1 P_1}{P_m}; \quad (3.8)$$

$Q_1$  is the non-atmospheric flow rate,  $P_m$  is the mean pressure  $(P_1 - P_2)/2$

The multi-cell cleaning system houses the core holders, pressure gauges and pneumatics presses, hence the confinement of the Hassler cell is achieved separately from the permeameter.

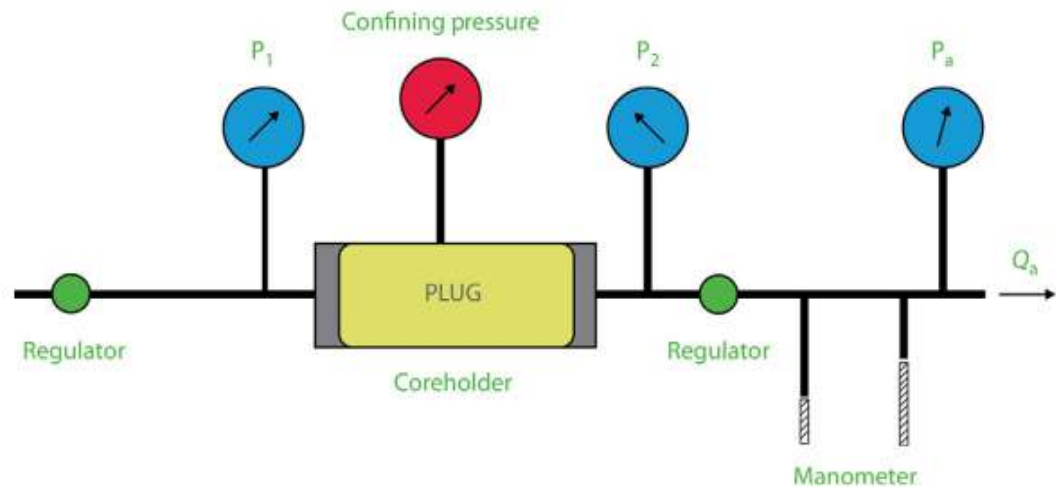


Figure 3.4 - The Schematic for general Gas Permeameters (McPhee et al., 2015).

*( $P_1, P_2, P_a$  and are the inlet, outlet and atmospheric pressures respectively.  $Q_a$  flow rate at the outlet)*

The sample with the fitted endcaps was placed carefully into the coreholder ensuring a perfect vertical alignment and avoiding tilts. The coreholder was filled with mineral oil to the marked circle near its top and closed firmly with the top lid only giving enough torque to open it after the experiment (Fig. 3.3C).

The measured sample dimensions were then inputted into computers of the multi-cell cleaning system and permeameter. The “fill” pressure gauge valve on the multi-cell system was opened and the confining pressure was then set to 500 psi.

The gas injection pressure was set at 100 psi. In this experiment the optimum flow rate  $Q$  ( $\text{cm}^3/\text{min}$ ) was determined to be  $500 \text{ cm}^3/\text{min}$ . The outlet pressure was set to 40 psi. The system was allowed to attain stability, the permeability ( $k$  in mD), was recorded and the outlet pressure was decreased by a factor of 2 until 0. i.e. 20, 10, 5, 2.5, 0. At each of these points, the permeability was recorded giving six points in total. The system automatically records readings periodically after every 20 seconds. The average gas permeability for each back pressure point was computed and compared with the manually observed data points. This is repeated for each of the six points.

The final step in the permeability data acquisition was to apply Klinkenberg's correction for determining liquid phase permeability. Gas slippage occurs at the pore walls due to the dependence of the permeability of a given rock sample to a gas on the molecular weight and pressure applied on the gas. To correct this klinkenberg found relationship between the gas permeability  $K_g$  and the steady state liquid permeability,  $K_l$  which is expressed as;

$$K_g = K_l \left( 1 + \frac{b}{P_m} \right); \quad 3.9$$

Where  $K_l$  is Klinkenberg's permeability (liquid permeability),  $b$  is the correction parameter (a constant for a specific gas in a particular rock type) and  $P_m$  is the mean flowing pressure.. Ideally, a plot between  $K_l$  and mean pressure  $P_m$  should give a straight-line. The  $K_l$  value at after the application of Klinkenberg's correction is the permeability of a gas at infinite pressure or a non-reactive fluid to the investigated sample.

Klinkenberg's correction is typically an important correction for measuring permeability of tight samples. Although the samples investigated in this study are very porous, a few samples exhibited non-darcy flows (due to gas slippage) as the relationship between  $K_l$  and

$P_m$  was non-linear. This was corrected by extrapolating the linear portion of the curve to obtain the liquid permeability.

### 3.2 X-ray Computed Tomography (CT)

In order to understand the pore network development in this young carbonate rock, whole core CT and high-resolution core plug CT-scans are utilized to visualize the pore network, while porosity and permeability measurements of core plugs are carried out to characterize the petrophysical properties. Moreover, high-resolution core plug CT-scans are also used for further visualization and analysis of the pore size and pore throat size frequencies and distributions.

X-rays are electromagnetic radiation generated by directing high energy accelerated electron beams towards atoms (usually Cu and Ga) to release electrons from atomic shells (Kronig, 1925)(See Fig. 3.5). The basic configuration of x-ray imaging includes: an x-ray source, an object and a detector equipped with a detector-scintillator for converting x-rays into visible light. An attenuation coefficient is measured for each pixel on the detector using the Lambert-Beer's exponential attenuation law given in 3.10.

$$\frac{I}{I_0} = e^{-\mu x} ; \quad (3.10)$$

Where  $I$  is the initial intensity,  $I_0$  is the final intensity of the x-ray upon interaction with the object sample,  $\mu$  (1/cm) characterizes the chemical composition of the material and x-ray energy and  $x$  (cm) is the path length of the x-ray through the material.

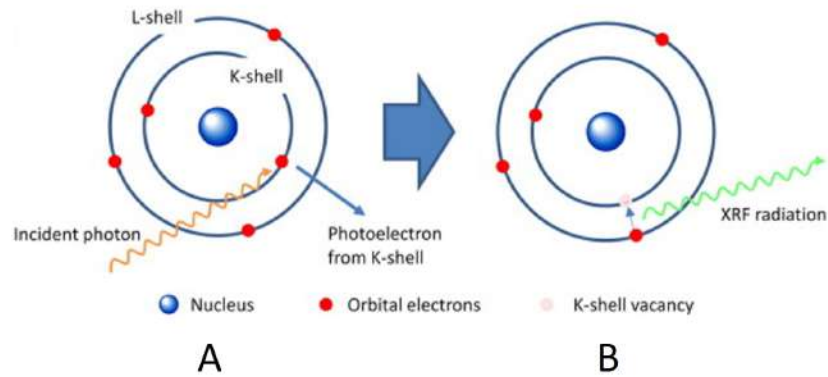


Figure 3.5 - Principle used in x-ray fluorescence tomography. (A) Electron ejection from the K-shell of an atom. (B) Fluorescence emission due to atomic stability and replacement of the K-shell electron by L-shell electron (Wildenschild & Sheppard, 2013)

Image acquisition is done using the cone-beam setup (Fig. 3.6) and the resolution  $R$ , of the CT image acquired is determined by;

$$R = \frac{d}{M} + s\left(1 - \frac{1}{M}\right); \quad (3.11)$$

Where  $d$  is the detector size and pixels,  $M$  is the geometrical magnification, and  $s$  is the X-ray spot size. The magnification  $M$ , is the ratio of the source detector distance (SDD) to the Source object distance (SOD).

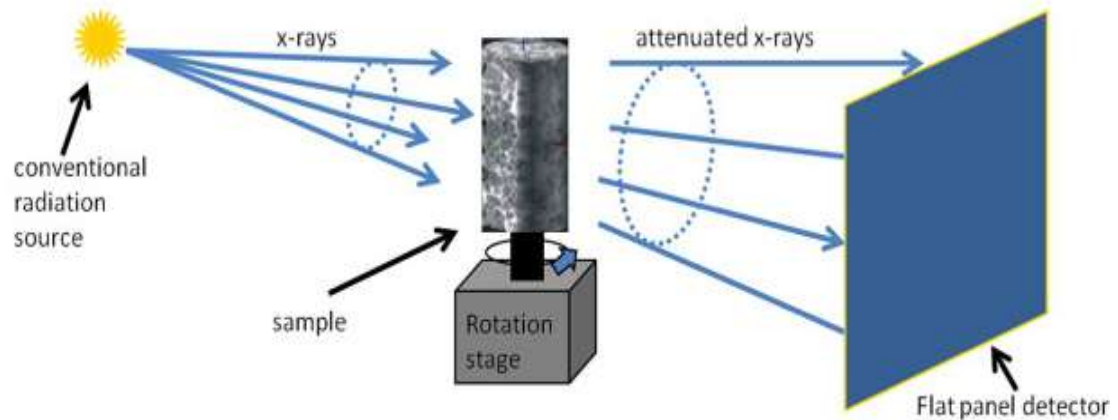


Figure 3.6 - Schematics for tomographic imaging for the cone-beam setup (Wildenschild & Sheppard, 2013).

CT images acquired usually undergo reconstruction and further image processing steps including; the application of beam hardening correction (BHC) for radial averaging of x-ray beam intensities in the images (Jin et al., 2015) and denoising techniques such as Gaussian and non-local mean filters to enhance gray scale image quality (Buades et al., 2005).

### **3.2.1 Whole core CT imaging**

Preparation for whole core section scanning sessions defers from core plug scanning sessions. In preparation for whole core scanning first the dried whole core sections (up to 60 cm) were arranged in specially designed core holders of length 75 cm (Fig. 3.7A). This is to achieve stacked scans of whole core sections. The core holder is a 10 cm diameter reinforced plastic cylinder with a thick base for support. The core holders held multiple broken core sections stacked on each other progressively with increasing depths. The stacking was done with maximum care and precision to avoid tilting of the core sections.

Table 3.1 Acquisition parameters for whole core CT images

Parameter	Value
Hardware (HW)filter	Sn 0.5 mm
Energy level	180kV
Autowatt	115 watts
Number of Averages	2
SDD	700 mm
SOD	268.3 mm
Detector mode	HW2, SW1, Low
Exposure time	55 $\mu$ s
Camera mode	1920 X 1896 pixel

After multiple scans to test the image quality, the optimum acquisition parameters for whole core CT images with 115  $\mu$ m voxel size were determined as follows; the of while using a 0.5 mm Tin (Sn) filter are summarized in Table 3.1;

The average scan time for 20 cm core section at 115- $\mu$ m voxel size and an average of two images is 20 minutes. The acquired images are stored as 960 x 948 pixel 16-bit TIF files.

### 3.2.2 Core plug CT imaging

In preparation for core plug scanning First the cleaned and dried core plugs (according to section 3.1.1) are placed on a carbon stick held vertically in place by the core plug holders, which are fixed to a base plate (Fig. 3.7B). The core plugs are attached firmly to the plug holders using double-sided adhesive waterproof tapes and maintained at a height 10-15 cm above the rotation stage. The plugs were scanned individually without using hardware filters.

The coreholder has a 50 x 50 mm base (Fig. 3.7b) with an adjustable wrench for holding the carbon stand in place. The coreholder is gently placed on the center of the rotation stage in the scanning cabinet. The stage is equipped with a magnet, which keeps the coreholder fixed on the rotating axis. To attain maximum vertical orientation of the plug sample, the coreholder is placed first on a goniometer before attaching it to the rotation stage (Fig. 3.7C). The average scan time for 6 cm core plug at 20- $\mu\text{m}$  voxel size and an average of 20 images is three hours. The acquired images are stored as 2D 1215 x 1269 pixel, 16-bit TIF files.

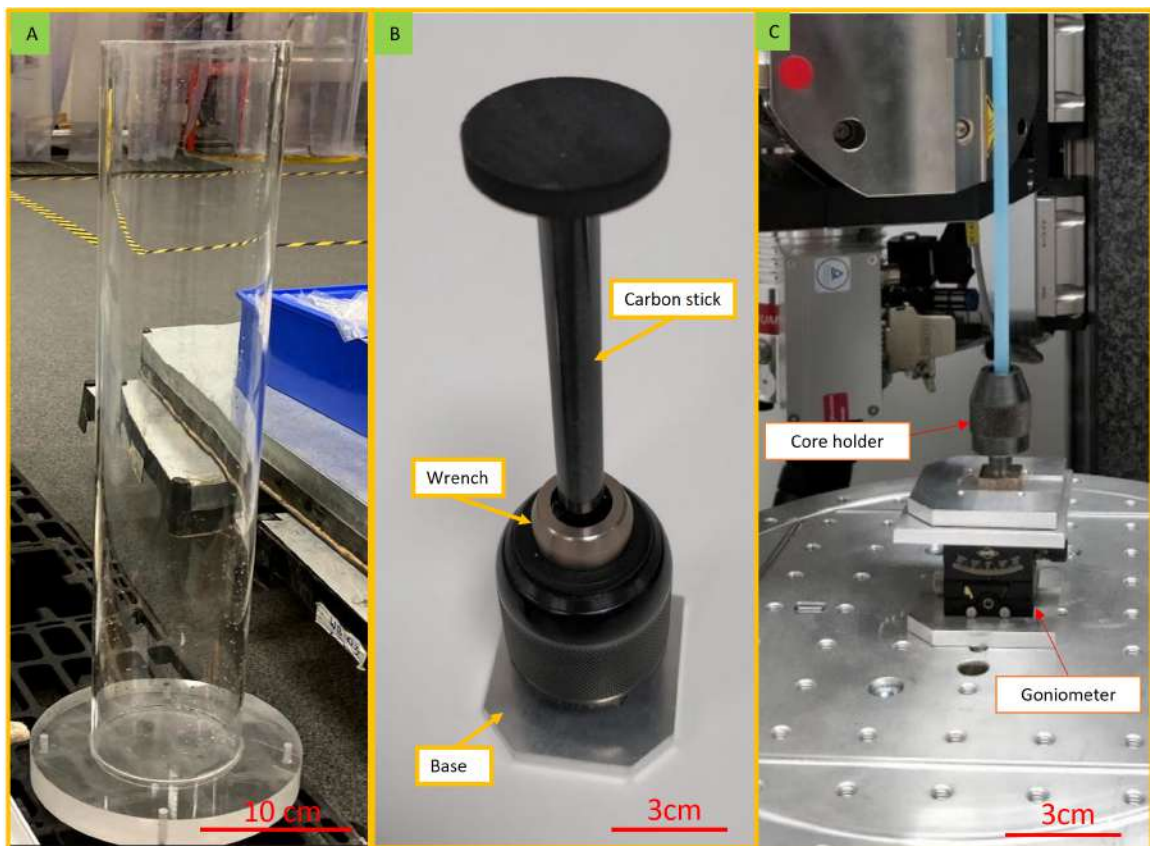


Figure 3.7 - X-ray CT Scan Coreholders. A) Reinforced plastic Coreholder for whole core CT. B) Core holder for plugs showing the carbon stick stand, the wrench and base  
C) core holder for plugs with a goniometer for vertical orientation

*(Courtesy Tescan images & ANPERC labs).*

Table 3.2 - Acquisition parameters for core plug CT images

Parameter	Value
Hardware (HW)filter	-
Energy level	80 kV
Autowatt	20 watts
Number of Averages	20
SDD	825 mm
SOD	55 mm
Detector mode	HW2, SW1, Low
Exposure time	103 $\mu$ s
Camera mode	2856 X 2856 pixel

### 3.2.3 CT image processing

Reconstruction of acquired x-ray CT images was done using Tescan's Acquila™ reconstruction software. As a first step the raw 2D projection data acquired during CT scanning are imported into the reconstruction software. The reconstruction steps that follow include normalization, application of ring filter, beam hardening correction (BHC), pre-calculation of CT- values and optimization of the Center of Rotation (COR) to the images. Due to the limited field of view (FOV) of the x-ray camera and x-ray beams, long samples are scanned in smaller sections which are then stacked to form the whole during CT image reconstruction processes. The reconstruction of multiple image data is called batch reconstruction. Batch reconstruction accesses multiple XRE.txt files attached to each scan for each width of the Field of view (FOV).

The reconstruction steps are described in more detail as follows.

### Normalization

The imported raw images are then normalized using two reference images: (1) A dark field image and (2) a white flat field image (Fig. 3.8A). The flat field image is the image captured when the x-ray is turned off while the white flat field image is the image captured when the x-ray is on but the sample is not in the FOV.

### Ring filter

Ring filter is applied to the imported projections to remove the systematic pixel deviations in the images. These are ring artifacts with ring appearance around the center of rotation caused by the flat panel detector with poor performances (Vidal et al., 2005). The standard value is dependent on the detector type. It is usually greater than or equal to one, however the software places a default value of 0.96 for highly dense materials.

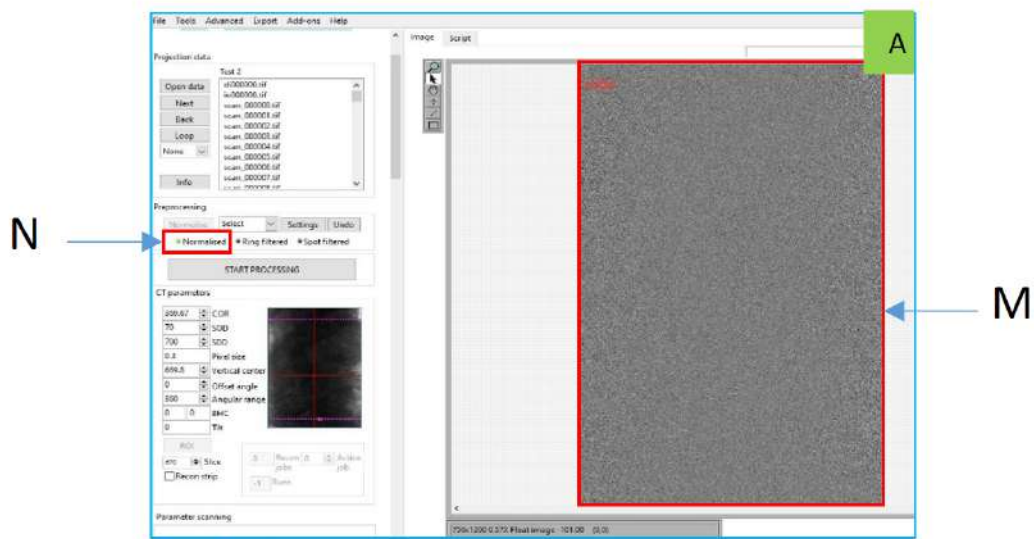


Figure 3.8 - Projection images normalization and Center of rotation correction. (A) N is the location of the normalization function, M is the image display panel.

### *Spot filter*

The spot filter is applied to exclude pixels with different response in the projection images by creating circular masks, which acts as noise in the images. The software by default uses ten. This size is the percentage above which the response is considered different.

### *Center of Rotation*

After the pre-processing procedures, the reconstruction uses a fast Fourier transform (FFT) of all the image slices and a reconstructed slice through the central axis is displayed for reference. The location of the Center of rotation is the horizontal axis equivalent of the rotation axis when the projected on the detector. An error in the COR results in blur double edges. This is found mostly in scan with over 360° rotation. The optimum COR angle is attained by selecting the “Scan par” button in the parameters scanning section, until the step value is less than 0.2 (Fig. 3.9).

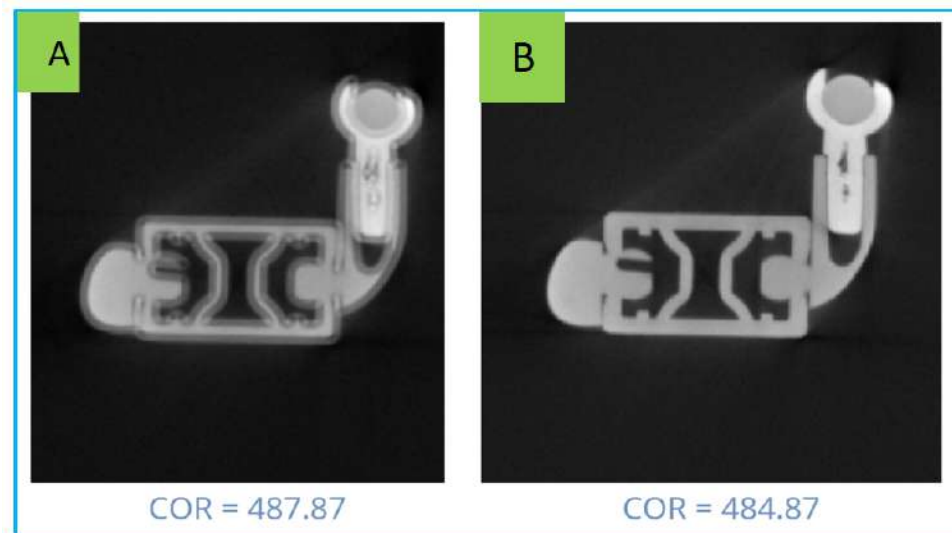


Figure 3.9 - Center of rotation (COR) correction). Illustration of the erratic (on the left) and COR corrected Image (on the right) (*Courtesy Tescan Images*)

### *Beam hardening correction (BHC)*

The optimum BHC coefficient is determined through the “scan with visual inspection” option of the CT parameters section. Ideally the coefficient lies between 0 and 1. As a result, the software displays nine images including a plot with the application corresponding coefficient, while the plot with the flattest profile is the optimum BHC coefficient (Fig. 3.10). Afterwards, the coefficient is inputted in the BHC1 space on the left and the system applies this automatically. During the experiment, BHC was completed using a coefficient of 0.125 for the whole core sections and 0 for the core plug CT images.

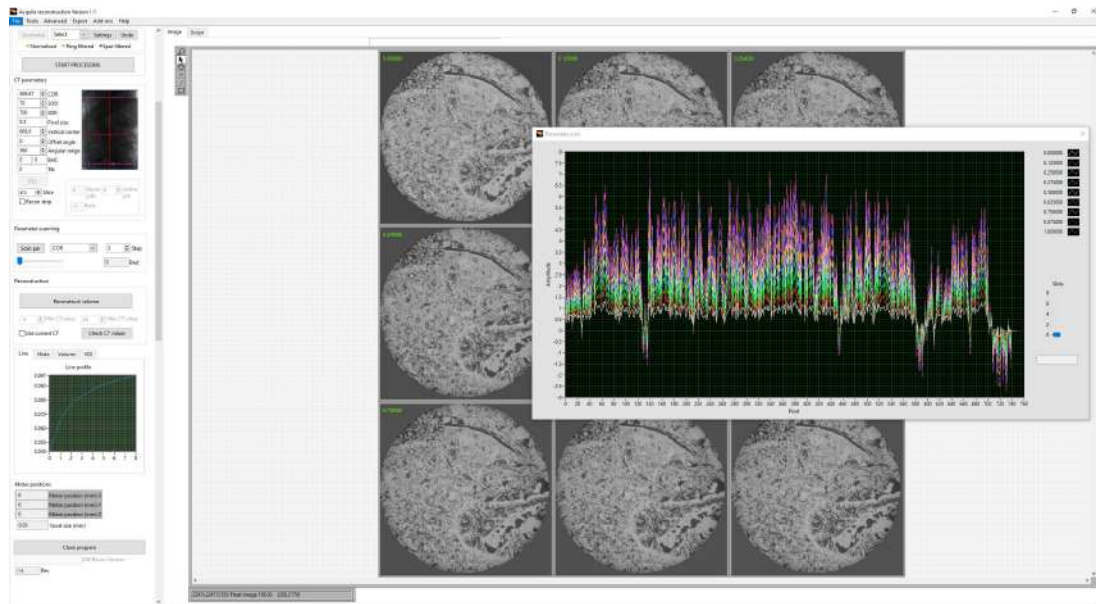


Figure 3.10 - Determining optimum Beam Hardening Correction coefficient.

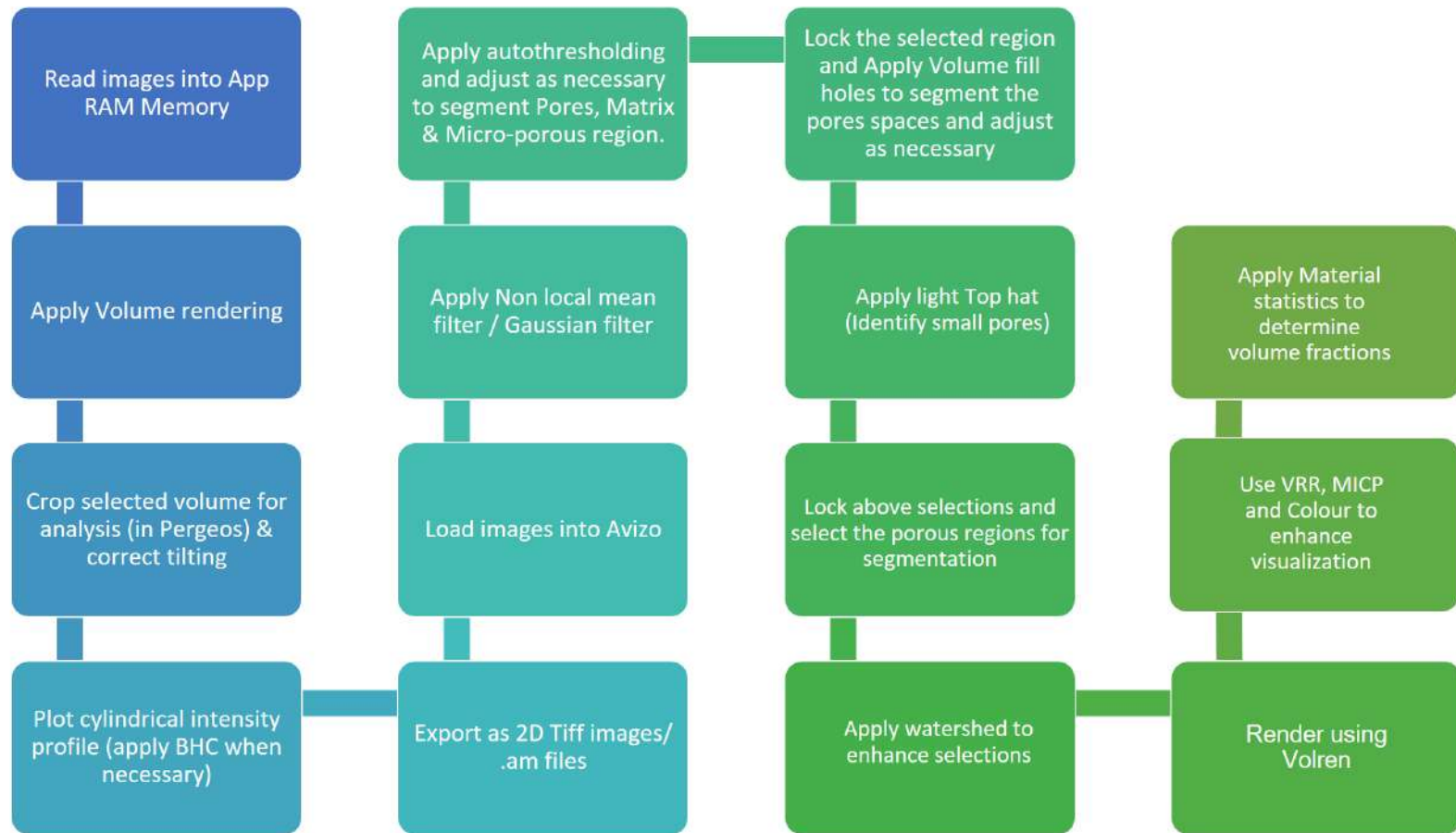
### **3.2.4 Pore network modelling**

ThermoFisher’s PerGeos™ v-2020.2 and AVIZO™ v-2020.2 image processing (IP) software were used for the final CT image 3D visualization, processing and analysis of the reconstructed images. The TIF file slices of the reconstructed CT images were imported

into Avizo™ and PerGeos™ with their corresponding voxel size; 115  $\mu\text{m}$  and 20  $\mu\text{m}$  for the whole core section and core plugs respectively.

Whole core and plug cropping and tilting corrections were completed using PerGeos™, while all segmentations and visualizations were completed using both Avizo™ and PerGeos™. The visualization of the 2D and 3D renderings and petrophysical simulations and modelling, such as pore network modelling, were completed using PerGeos™.

The pore network model of a given regular cubic volume of the investigated sample is represented by a 3D mesh network of lines representing pore throats with branched ends which are the pores to represent an approximate pore-structure of the investigated rock sample. This is done by creating a label image (from separate pore function) and using the extract PNM function. The PNM function of two phase flow is based on 3D voronoi clustering of grains to for the model skeleton. Afterwards, the clusters are grown from the skeleton voxels with three or more grains and centered with near grains with the largest radius. This cluster is then converted to a node with a link. The output result assigns all pores to either a node or a link. This resulting data from the modelling was used for the determination of other petrophysical properties like the absolute permeability. Results obtained include, the pore throat radius, pore radius, coordination number of each pore, pore equivalent diameter. The pore network modelling and image processing methodology are summarized in figure 3.11A and B.



(A)



(B)

Figure 3.11 - Work flow for the image processing and Analysis PerGeos and Avizo (A) methodology for whole core sections.

B) Methodology for core plugs

## Chapter 4

### Results

#### 4.1 Petrophysical measurements

##### 4.1.1 Porosity

Laboratory measured plug porosity was mostly constant in the first 8 m with values ranging from 35 to 48%. The lowest porosity value for the core value 23% is located at core depth 13.72 m. The maximum porosity was 49% for a plug located at 9.9 m depth (Fig. 4.1A). The plug with the highest porosity is composed of cavity filled encrusted *Porites sp.* framestone (MFT3), while the plug with the lowest porosity is composed of encrusted coral rudstone (MFT4), which is the most abundant MFT in the core. The highest porosity values are attributed to the subsection L and with lithofacies LFT3 (Coral Floatstone-Rudstone), while the plug with the lowest porosity value is attributed with subsection T and with LFT1 (bioclastic wackestone-packestone). The average laboratory measured porosity for the entire core is 41.8%. At subsection L, porosity increased significantly reaching 48% at 16.7 m and reduces to 39% at 16.9 m, although the facies is not changing.

##### 4.1.2 Permeability

The permeability measurements ranged from a minimum of 8.4 mD and maximum of 5147 mD, indicating a significant vertical heterogeneity in the pore networks, which caused this variation across 3 orders of magnitude. The plugs with the minimum and maximum measured values were associated with MFT5 (Red algae bindstone) and MFT 4 (encrusted

coral rudstone) microfacies and are located at 13.72 m and 6.5 m respectively (Fig 4.1B). There is an overall permeability reduction with depth along the core and displayed alternating cycles of peaks and troughs. The average measured permeability is 804 mD. At subsection L (Fig. 2.4), permeability increased significantly reaching 659 mD at 16.9 m indicating a possible depositional cyclicity.

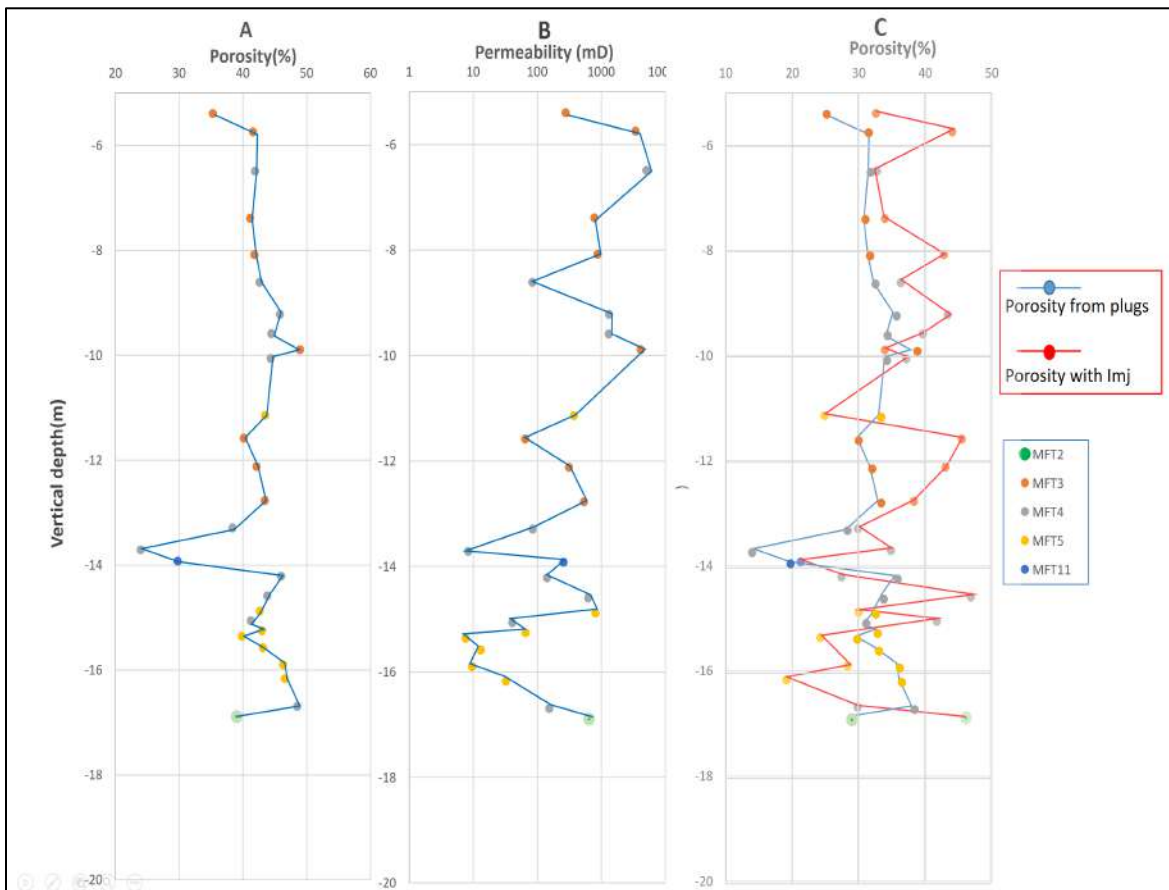


Figure 4.1 - Petrophysical Measurement for DIBH006. A) Laboratory measurement of Porosity with depth. B) Laboratory Measurement of Permeability with depth. C) Laboratory vs Image-J measurement of porosity with depth (Chirakal et al. in prep) (MFTs are described in Chapter 2.2.2)

## 4.2 Porosity-Permeability relationship

With porosity and permeability measured from one inch diameter plugs as representative element volume (REV) for a core section, the porosity-permeability cross-plot (Fig. 4.2A) reveals a broad distribution of permeability values within a narrow range of porosity values. Overall, MFT3 microfacies is associated with high porosity and permeability (dark orange cluster), while MFT5 has high porosity but lowest permeability (light orange cluster in Fig. 4.2A). MFT 4 (gray cluster) is evenly distributed across all porosity and permeability values, and is characterized as a transition facies. MFT2 and MFT11 are rare in the core but show overall higher permeability ( $> 250$  mD), while the porosity is lower compared to the other facies ( $< 40\%$ ).

A cross plot of porosity and permeability, when coloured with lithofacies presents a similar pattern. LFT2 shows the highest permeability values (red cluster), while LFT4 presents the lowest (purple cluster). LFT5 and 7 represent transitional facies (lilac cluster). LFT1 and 3 scatter the most (no cluster) (Fig. 4.2B).

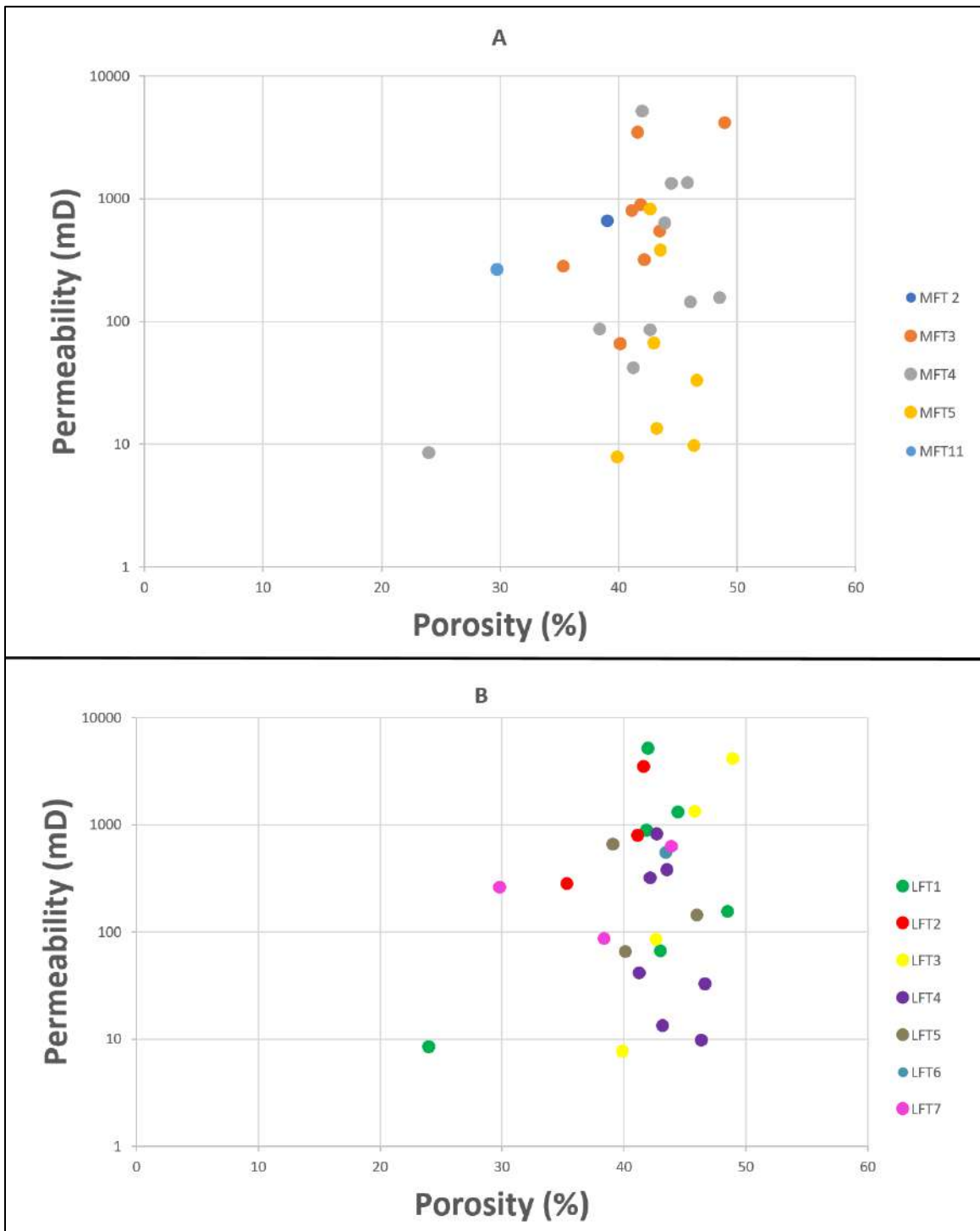


Figure 4.2 – Porosity, Permeability vs Facies Types Cross-plots. A) Cross-plot for microfacies types (MFT) B) Cross-plot for Lithofacies type (LFT) (MFTs & LFTs are described in Chapter 2.2)

### 4.3 CT image Results

The core images and gray scale CT images of the seven identified lithofacies are presented in the figure 3.3. Nine plugs were selected for further analysis, while three of these nine were selected to represent each subsection (T, M, and L) described for detailed pore characterization. The three plugs were selected based on the petrophysical analysis in chapter 4.1. The plugs extracted from 5.4 m and 10.07 m depths are characterized by highest porosity-permeability values while the plug from 13.72 m depth is characterized by the lowest measured porosity and permeability.

#### 4.3.1 Core and Grayscale images

The dark gray to black colour in the CT grayscale images represent porosity (pore space, air, plughole), while all gray to white portions represent grains and the matrix. General visual observation shows the gray scale image of LFT1 (Bioclastic wackestone –packstone; Fig. 4.3A) and LFT4 (Coral redalgae floatstone-rudstone; Fig. 4.3D) show the lowest visible porosity (higher x-ray attenuation) compared to other LFTs. LFT3 (Coral framestone; Fig. 4.3C) and LFT7 (Bioclastic floatstone-rudstone; Fig. 4.3E) have the highest visible pore space representation (lower x-ray attenuation). The predominant pore spaces observed in the LFT7 grayscale image also correspond to the cross section of coral growth framework, which dominates this facies type. This is also observed in Figure 4.3B, LFT2 (Coral Rudstone) with most visible porosity corresponding to the cross-section of the coral (*Porites Sp.*) in the CT image. Dissolved shells and other bioclasts host the pore spaces in LFT6 (Bioclastic floatstone-rudstone) (Figure 4.3F). Elongated vugs (and plughole) observed in Figure 4.3G characterized the visible pore spaces in the grayscale

image. However, the laminated red algae show low intensity as observed in the grayscale CT image and is likely microporous.

From the visual observation, the identified dominant pore types, following Lucia (1995), are interparticle porosity (LFT1 and LFT4), touching vugs porosity (LFT2, LFT3, LFT5, LFT6) and separate vugs (LFT6) porosity. According to Choquette and Pray (1970), the dominant pore types are interparticle porosity (LFT1), intraparticle porosity (LFT2, LFT3, LFT5), mouldic porosity (LFT6), and growth framework porosity (LFT7).

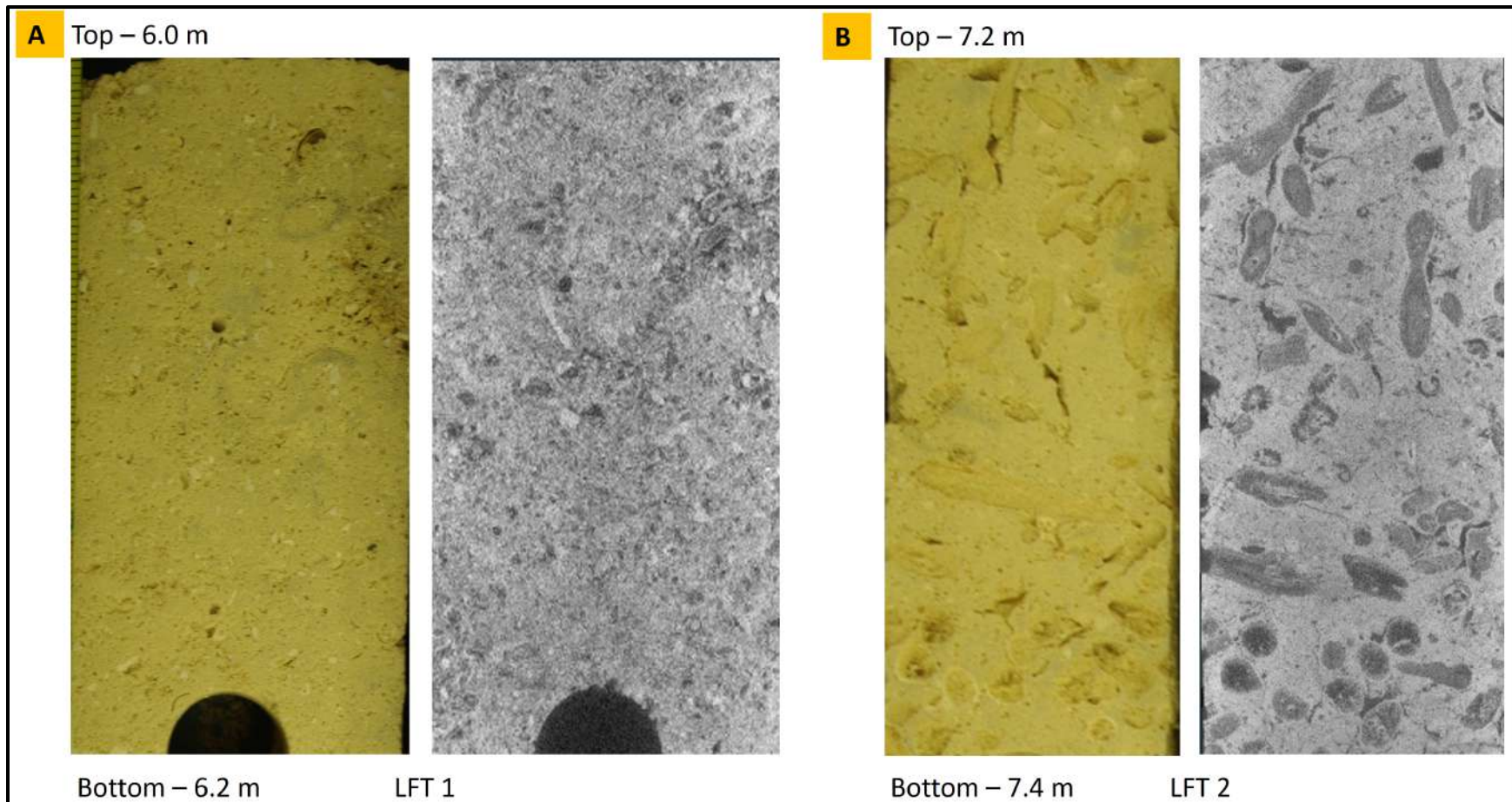


Figure 4.3A-B - (A) LFT1 - Bioclastic wackestones – packstones. (B) LFT2 - Coral rudstones

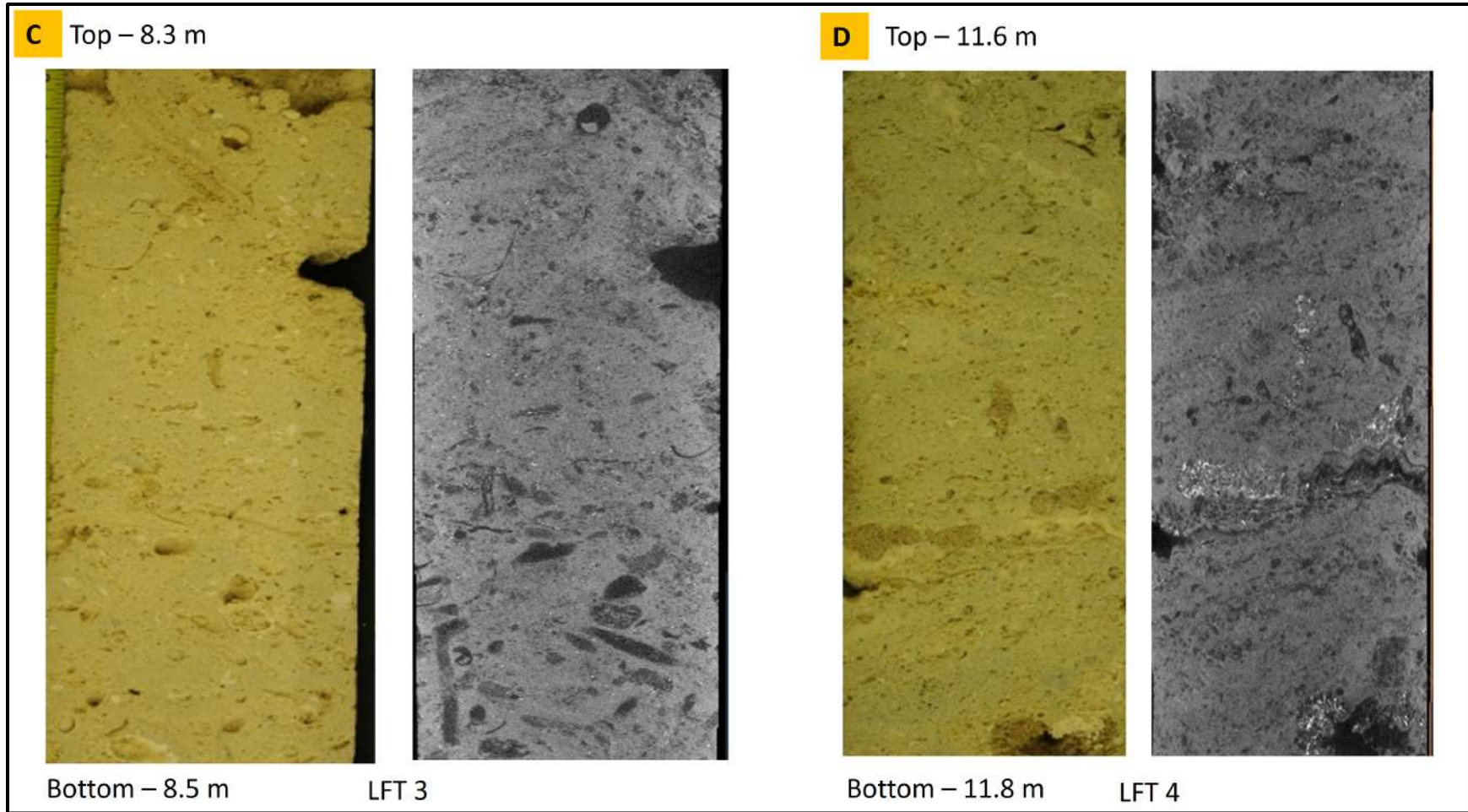


Figure 4.3C-D - (C) LFT 3 - Coral floatstone-rudstone. (D) Coral - Red Algae floatstone - rudstone

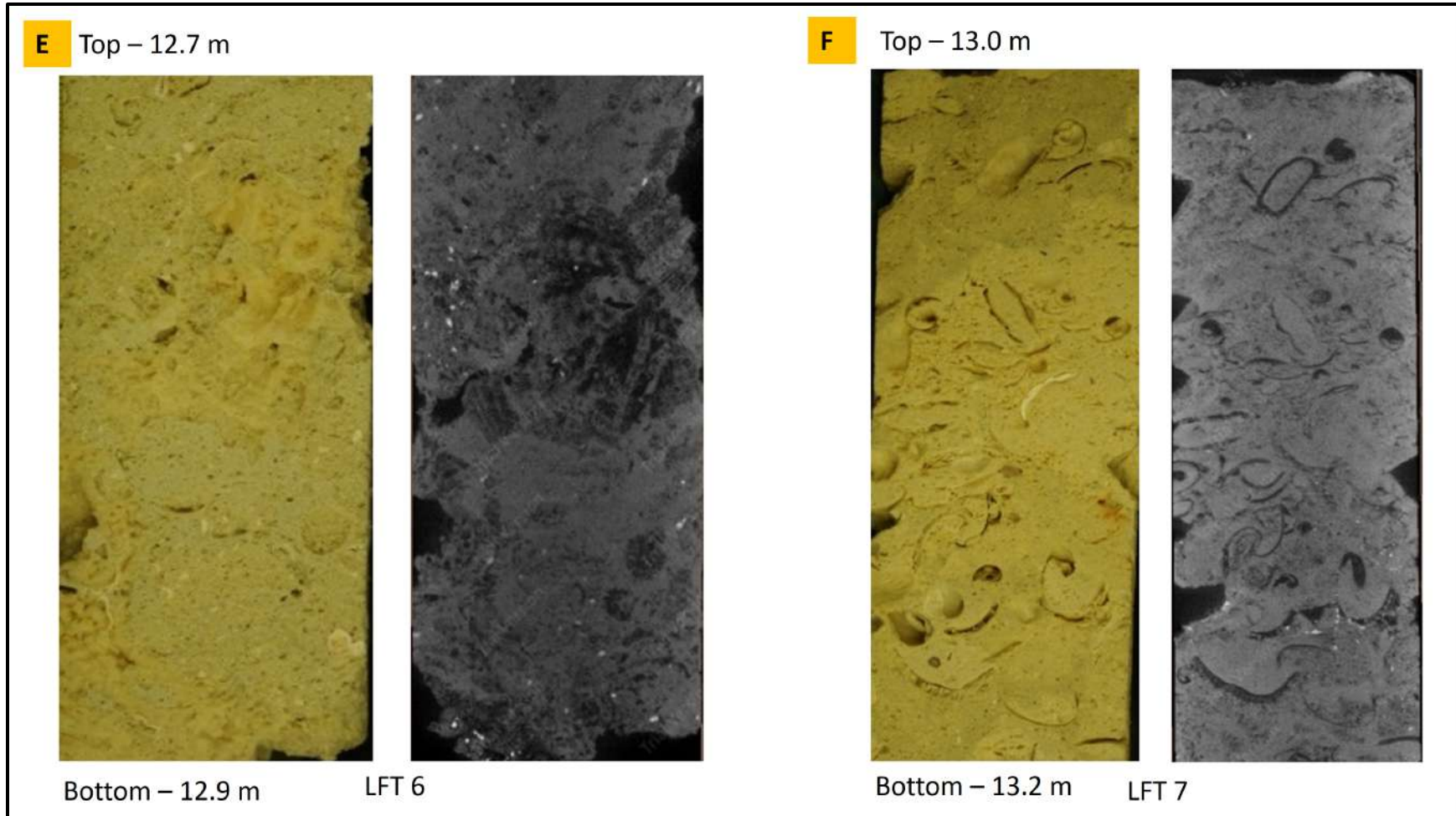
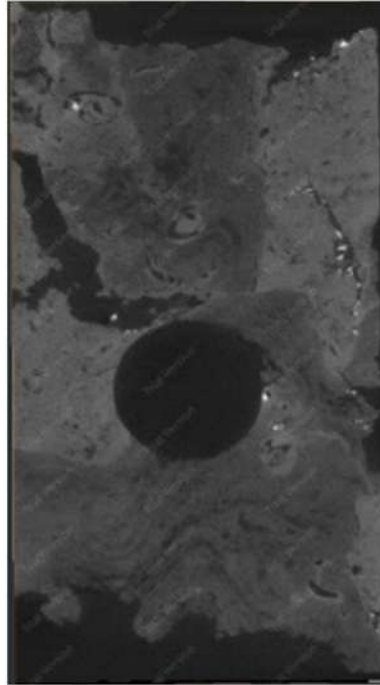
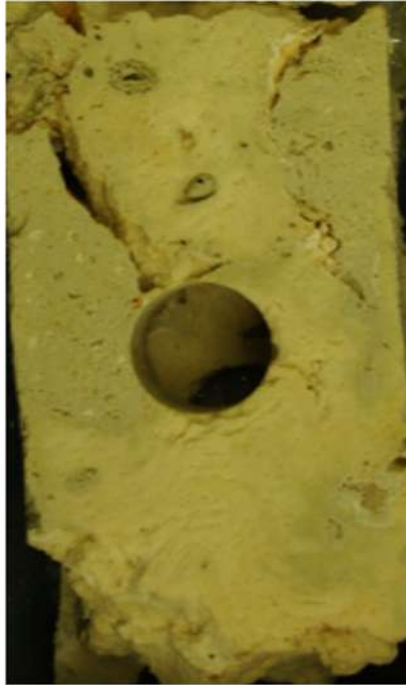


Figure 4.3E-F - (E) LFT6 - Coral framestone. (F) LFT7 - Bioclastic floatstone-rudstone

**G** Top – 16.8 m



Bottom – 16.95 m

LFT 5

Figure 4.3G - LFT5 - Red algae bindstone

#### 4.4 3D Visualization of pores, pore types and pore network models.

##### 4.4.1 Sample 1 (5.27 – 5.44 m): subsection T, Lithofacies - 2 – Plug 01

Most of the porosity (blue) corresponds to the coral frameworks (*Porites Sp.*). Their random mesh of network dominates the top and bottom parts of the investigated core section while being sparse at the core plug's location. These highly porous fingerlike coral features have lengths reaching 6 cm (Fig. 4.4C) and accounts for most of the macro porosity seen in the image. Due to the high-resolution data more matrix related porosity is observed in the plug (Fig. 4.4D). A subplug is extracted from a section of the matrix where the impact of the coral feature is minimum (Fig. 4.4E) and dominated by interparticle porosity. The subplug is characterized by mainly touching vugs porosity with radius ranging four orders of magnitudes. Pore radius and pore throat sizes range from 0.26  $\mu\text{m}$  to 473  $\mu\text{m}$  and 0.01  $\mu\text{m}$  to 230  $\mu\text{m}$  respectively (Fig. 4.5). Most of the pores throats have a radius of 17.5  $\mu\text{m}$  and the average radius is 28.3  $\mu\text{m}$  (Fig. 4.6). The dominant pore radius for the investigated subplug is approximately 40  $\mu\text{m}$  and the average pore radius size is 58.5  $\mu\text{m}$ .

Two main pore classes are observed in the pore size distribution plot according to the pore classification modification of Choquette and Pray (1970) made by Moore and Wade (2013), micropores (< 62.5  $\mu\text{m}$ ) and mesopores (62.5  $\mu\text{m}$  – 4mm; Fig. 4.6). The third class of pores are observed in figure 4.3B-C, which are megapores (> 4 mm). The measured porosity from the CT subplug is 29.7% and has pore connectivity of about 94 % (Fig. 4.3B-D).

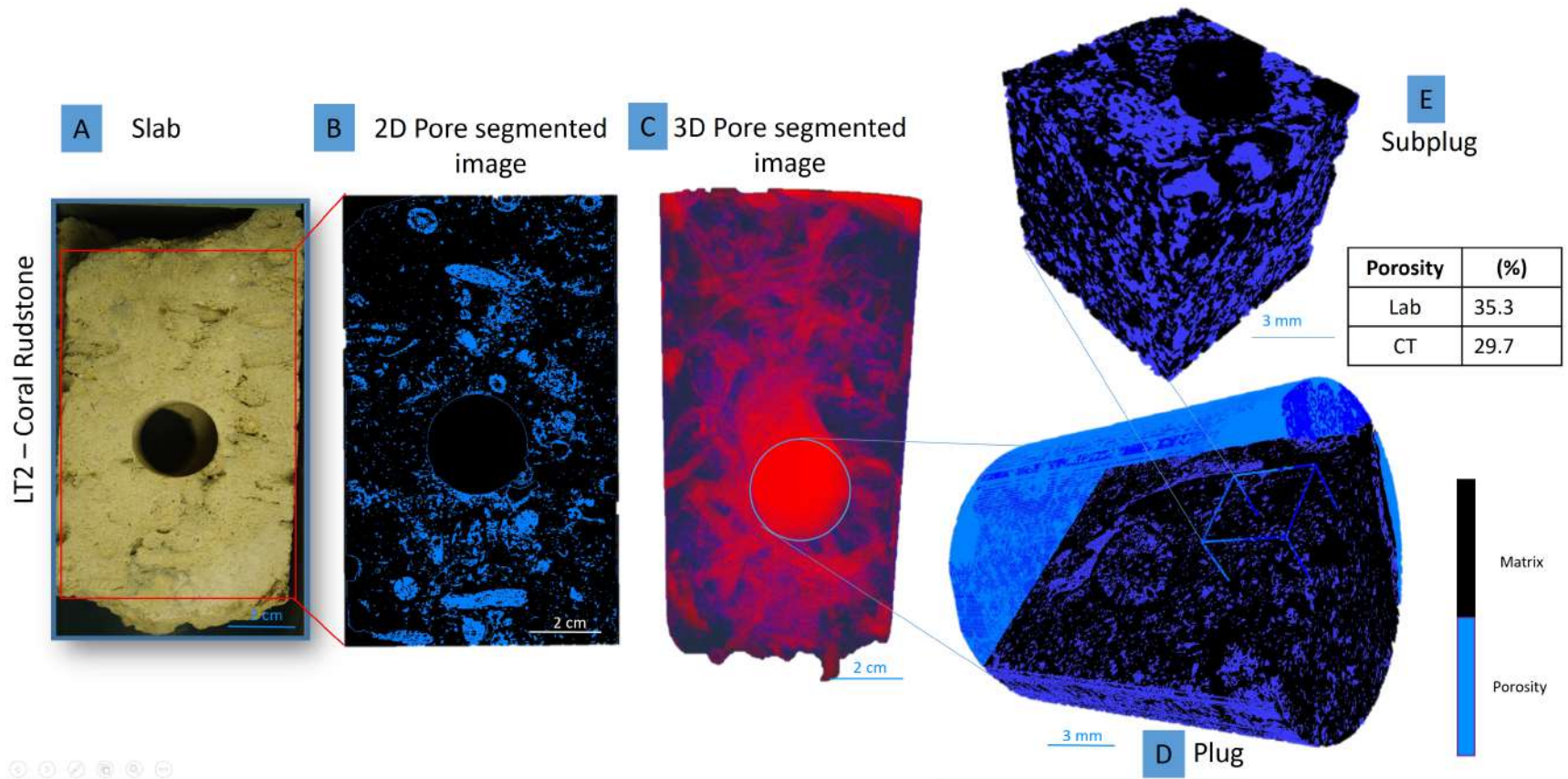


Figure 4.4 – Pore and pore types visualization methodology. Example with core section (5.27-5.44m) showing the resulting images; (A) Photograph of slabbed core. (B) Shows coral dominated 2D CT slice with segmented pore spaces (blue). (C) 3D rendering of segmented pore spaces. (D) 3D plug rendering with segmented pores. (E) Subplug from plug for pore network modelling. *(The whole core sections were scanned at 115  $\mu\text{m}$  resolution while the plug and subplug images were scanned at a resolution of 20  $\mu\text{m}$ . All features highlighted in blue represents porosity except image C; porosity is rendered in red for better visualization of pore network)*

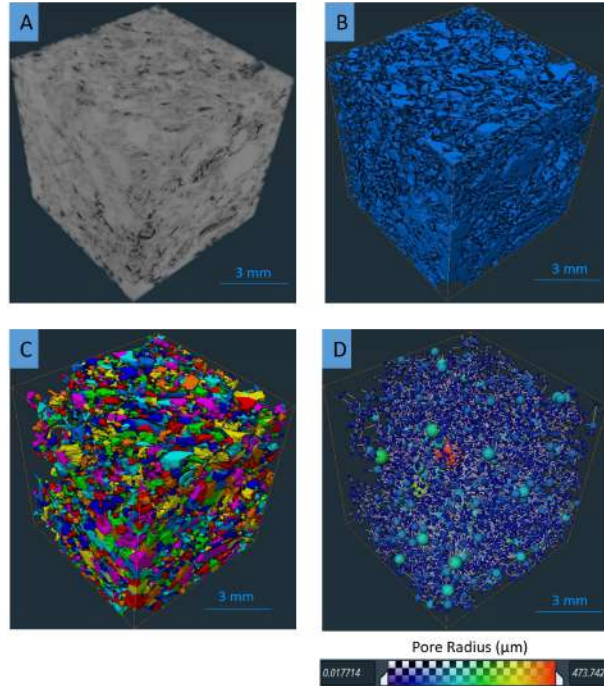


Figure 4.5 – Pore space representation of pores segmented from extracted 300 x 300 x 300 pixel subplug from DIBH006 Plug 1. (A) Grayscale rendering of subplug. (B) 3D rendering of all segmented pore spaces of subplug. (C) 3D rendering of all connected segmented pores space. All connected pores are separated using 8 different label colours. (D) Pore network model extracted from connected pores.

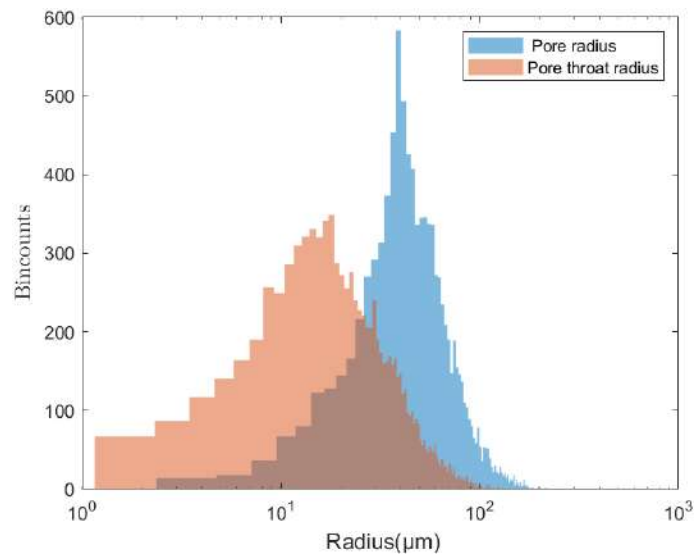


Figure 4.6 – Pore size and Pore throat size distribution extracted from the pore network model of DIBH006 Plug 01

Table 4.1 – Numerical porosimetry of Plug samples.

Sample name	Depth (m)	LFT	MFT	Lab Porosity (%)	CT Porosity (%)	Connectivity of Pore space (%)	Min PR (µm)	Max PR (µm)	Min PTR (µm)	Max PTR (µm)
Plug 01	5.40	LFT2	MFT3	35.32	29.7	94.2	0.26	473.5	0.13	231.7
Plug 02	5.75	LFT2	MFT3	41.62	37.5	88.3	0.38	377.6	0.32	254.8
Plug 03	6.50	LFT1	MFT4	41.99	26.1	86.6	2.32	350.1	1.61	293.62
Plug 04	8.62	LFT3	MFT4	42.66	25.9	77.2	0.24	479.7	0.01	257.6
Plug 05	10.07	LFT3	MFT4	44.39	35.6	99.2	0.24	443.8	0.02	253.3
Plug 06	13.72	LFT1	MFT4	24.03	23.4	73.9	0.03	458.9	0.01	289.9

\*PTR = Pore throat radius ; PR = Pore radius.

#### 4.4.2 Sample 2 (10 – 10.2 m): subsection T, Lithofacies - 3 – Plug 05

The 2D slice in figure 3.6B shows predominantly a cross-section of dissolved coral (*Porites Sp.*) fragments and large touching vugs. The section is also dominated by interparticle pore space from red algae mesh network visually showing higher connectivity than sample 1. Figure 4.7C shows the strands of coral fragments dominating the top portion of the core section, while being occluded by a cloud of highly interconnected pore mesh from encrusting red algae. The subplug is dominated with large touching vugs porosity (Fig 4.7E). The measured porosity from the CT subplug data is 35.5% and pore connectivity of about 99 % (Table 4.1; Fig 4.8B-D). The subplug is characterized by mainly interparticle and touching-vugs porosity with radii ranging four orders of magnitudes. Pore radii and pore throat sizes range from 0.26 µm to 443.8 µm and 0.02 µm to 253.3 µm respectively (Fig. 4.6). Most of the pores throats have a radius of 14 µm and the average throat radius

size is 28.5  $\mu\text{m}$  (Fig. 4.6). The dominant pore radius size for the investigated subplug is approximately 50  $\mu\text{m}$  and the average pore radius size is 58.7  $\mu\text{m}$ .

Two main pore classes are also observed in the pore size distribution (Fig. 4.9) according to the pore classification by Moore and Wade (2013), micropores ( $< 62.5 \mu\text{m}$ ) and mesopores ( $62.5 \mu\text{m} - 4\text{mm}$ ; Fig. 4.8). The third class of pores are observed in figure 4.7B-C, which are megapores ( $> 4 \text{ mm}$ )

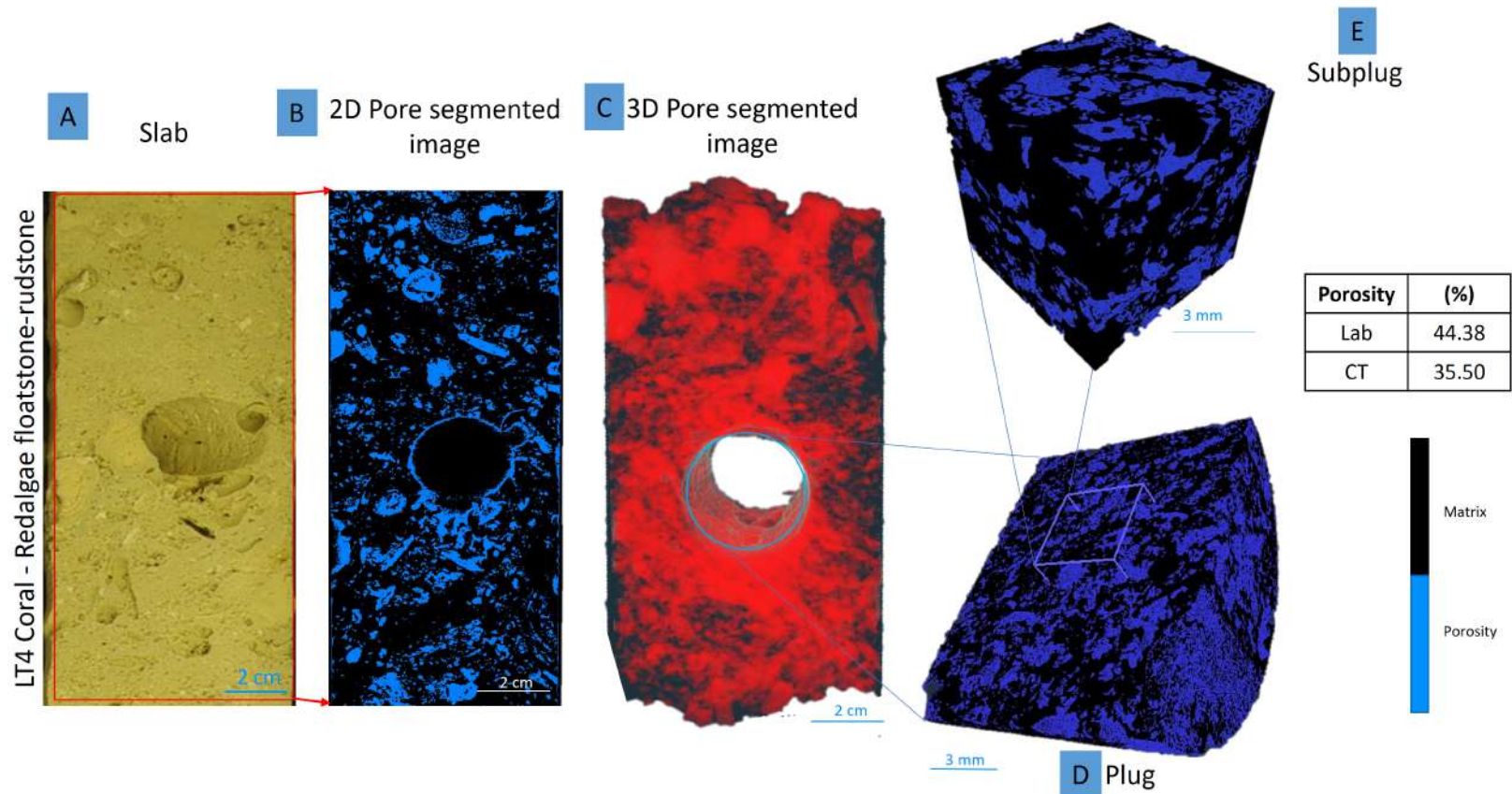


Figure 4.7 – Pore and pore types visualization of sample 2 (10 – 10.2 m). Example with core section (10 -10.20 m) showing the resulting images; (A) Slab image of core. (B) Shows coral redalgae dominated 2D slice with segmented pore spaces. (C) 3D rendering of segmented pore spaces. (D) 3D plug rendering with segmented pores. (E) Subplug from plug for pore network modelling. *(The whole core sections were scanned at 115  $\mu$ m while the plug and subplug images were scanned 20  $\mu$ m. All features highlighted in blue represents porosity except image C; porosity in rendered red for better visualization of pore network)*

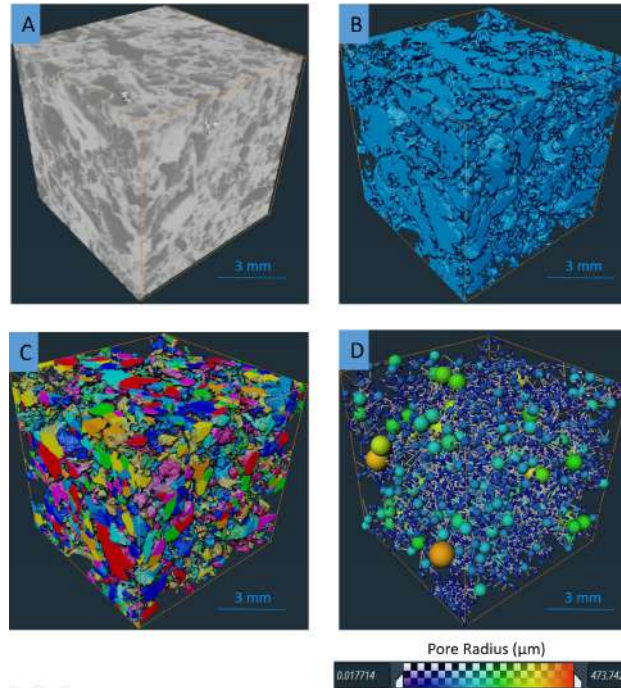


Figure 4.8 – Pore space representation of pores segmented from extracted 300 x 300 x 300 voxel subplug from DIBH006 Plug 5. (A) Grayscale rendering of subplug. (B) 3D Rendering of all segmented pore spaces of subplug. (C) 3D rendering of all connected segmented pores space. All connected pores are separated using 8 different label colours. (D) Pore network model extracted from connected pores

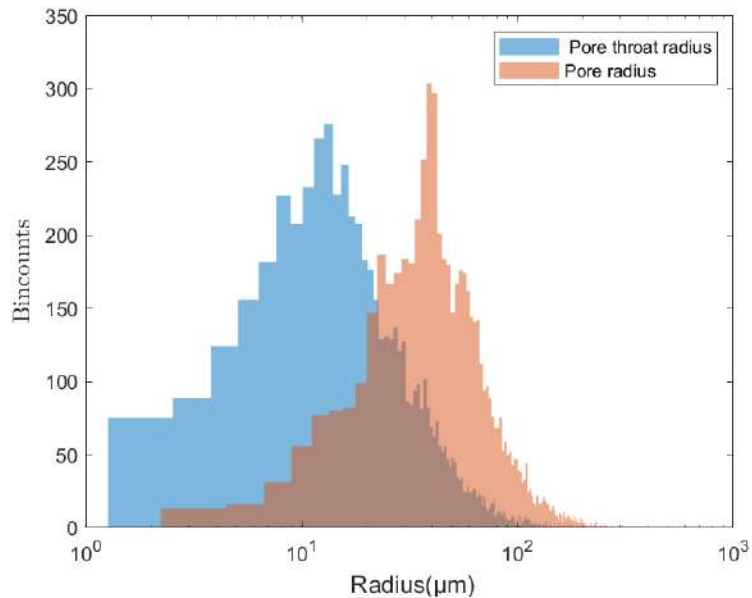


Figure 4.9 - Pore size and Pore throat size distribution for DIBH006 Plug 05

#### **4.4.3 Sample 3 (13.7 – 10.2 m): subsection L, Lithofacies -4 – Plug 06**

This section is dominated by bioclasts and shells of bivalves (Fig. 4.6B). Vugs and interparticle pores spaces are sparsely observed. The top portion shows less porosity than the portion below the plug (Fig. 4.10C). The extracted plug (Fig. 4.10D) shows separate vugs and interparticle pore space (megapores), which can be observed in the subplug (Fig. 4.10E). The pore connectivity is about 73.9 % (Fig. 4.11B-D).

Pore radius and pore throat sizes range from 0.26  $\mu\text{m}$  to 443.8  $\mu\text{m}$  and 0.01  $\mu\text{m}$  to 289.9  $\mu\text{m}$  respectively (Fig. 4.5). The dominant pores and pore throat radius have is about 35  $\mu\text{m}$  and 14  $\mu\text{m}$  (Fig. 4.12). The average pore and pore throat radius size are 48  $\mu\text{m}$  and 23.4  $\mu\text{m}$ .

Two main pore classes are also observed in the pore size distribution plot in Figure 4.12 according to the pore classification made by Moore and Wade (2013), micropores (< 62.5  $\mu\text{m}$ ) and predominantly mesopores (62.5  $\mu\text{m}$  – 4 mm) (Fig. 4.12). Megapores are also sparsely observed (Fig. 4.10B-C).

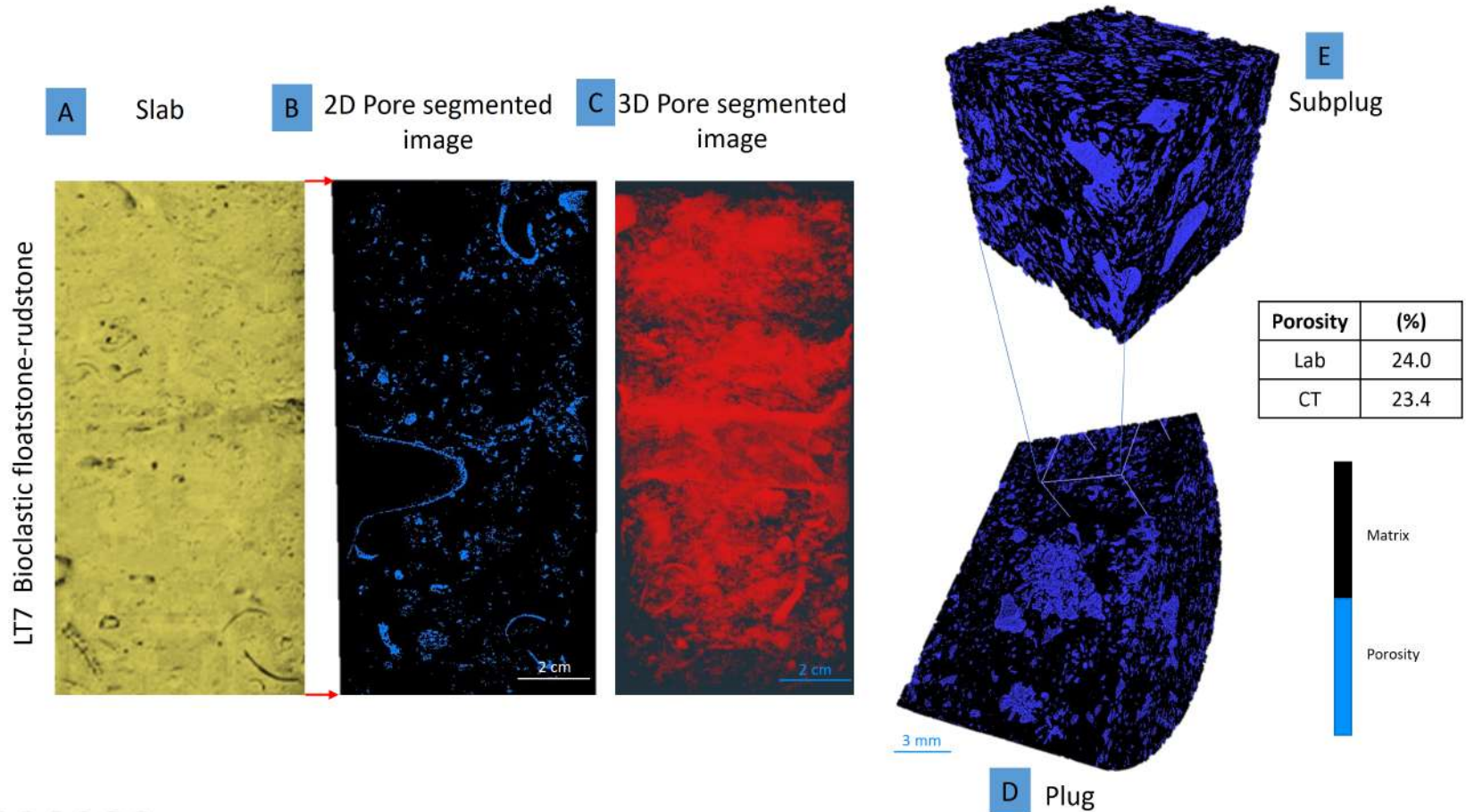


Figure 4.10 – Pore and Pore types visualization methodology for core section (13.6 -13.80 m) showing the resulting images; (A) Slab image of core. (B) Shows coral red algae dominated 2D slice with segmented pore spaces. (C) 3D rendering of segmented pore spaces. (D) 3D plug rendering with segmented pores. (E) Subplug from plug for pore network modelling. (The whole core sections were scanned at 115  $\mu\text{m}$  while the plug and subplug images were scanned 20  $\mu\text{m}$ . All features highlighted in blue represents porosity except image C; porosity in rendered red for better visualization of pore network

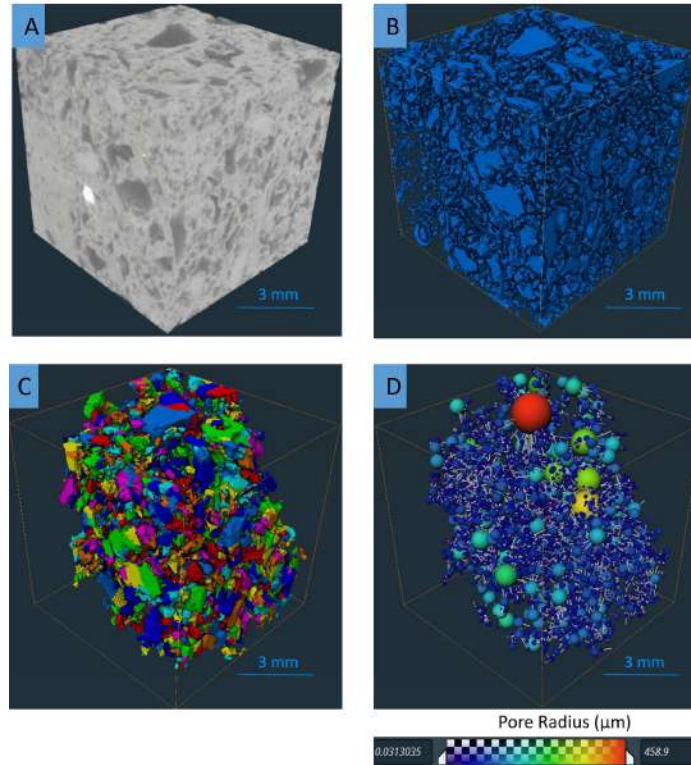


Figure 4.11 – Pore space representation of pores segmented from extracted 300 x 300 x 300 voxel subplug from DIBH006 Plug 6. (A) Grayscale rendering of subplug. (B) 3D Rendering of all segmented pore spaces of subplug. (C) 3D rendering of all connected segmented pores space. All connected pores are separated using 8 different label colours. (D) Pore network model extracted from connected pores

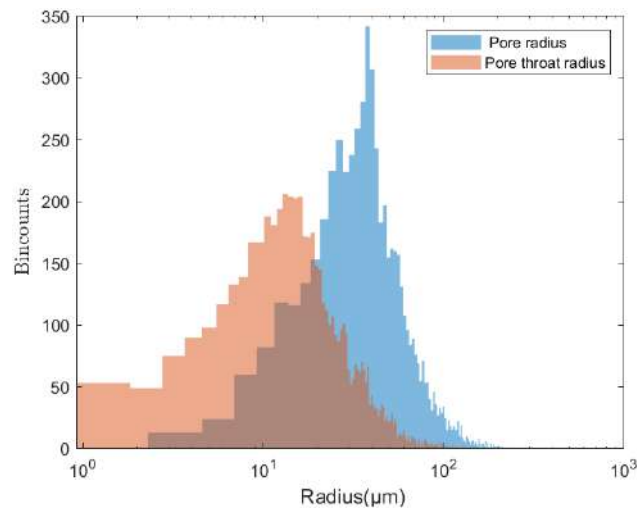


Figure 4.12 - Pore size and pore throat size distribution for DIBH006 Plug 06

## **Chapter 5**

### **Discussion**

Measured porosity along the core is relatively high and almost constant (Fig. 4.1- 4.2; Table 4.1). The thin section images analyses conducted by MS candidate Tojo Chirakal indicates that most of the primary porosity remains conserved (Append B5), and highlights the young age of the limestone succession. Significant leaching porosity from the dissolution of allochems are also observed explaining the high mean porosity and subsequently the permeability of the investigated core. Porosity measurements from 2D images using Image-J software (Chirakal, in prep.) did not correlate with the laboratory measurements, especially at lower depths deeper than 13 m (Fig 4.1C). This is because 2D images contain less detail in comparison with 3D images hence the heterogeneities from 2D images are not fully represented.

#### **5.1 Facies vs. Poroperm**

Depositional fabrics and facies control primary pore formation and the resulting modifications to pore geometry and connectivity (Rankey et al., 2018). This subsequently affects petrophysical properties of carbonate rocks significantly. The cross-plots (Fig. 4.1 and 4.2) indicate the possible dependence of permeability on the lithofacies and microfacies types though a clear notable trend is not observed. However, the variability of the different clusters consisting of similar LFT and MFT are observed to have high or relatively low poro-perm values. This means that samples with similar LFT and MFT have

similar poro-perm values. Different facies at different depths exhibit varying poro-perm relationship (Hazard et al., 2017) i.e. LFT 2 (coral rudstone) and MFT3 (encrusted sediments covered coral framestone) which occurs mainly in LFT2 are observed to have the highest porosity-permeability (48.9 % Poro, 4196 mD Perm). LFT2 is dominated by corals (*Porites Sp.*), which represents regions with high porosity and permeability as established in section 4.1.1. In comparison, LFT 4 and MFT5 show relatively low permeability (8.96 – 41.3 mD), and are characterized by the abundance of red algae encrustation and show signs of pore filling and pore bridging cementation.

Corals (*porites Sp.*) decreases with depth from subsection T to M (Fig. 2.4), while red algae increases with depth, indicating an influence of facies and reef assemblages on permeability. Given the above, corals (*Porites Sp.*) characterizes sample 1 (5.4 m) and sample 2 (10.07 m) depth is characterized by corals (*Millepora Sp.*)

The high-resolution CT data points to a strong influence of the coral frameworks on connectivity resulting in high permeability (282 – 3463 mD) pathways. Based on the diagenetic analysis (Chirakal, in prep), the original aragonitic coral frameworks were dissolved and only partially replaced by calcite crystals leading to an enhancement of the dominant primary porosity. These pores were formed during the first exposure of the island as a consequence of the sea level fall after the MIS 5e highstand documented by Gowan et al., (2021). Compared to that, the neomorphosed high magnesium calcite mineralogy of the red algae to low magnesium calcite (Bathurst, 1994) while retaining its initial structure enabled a constant poroperm values after neomorphism. This does not exclude the role of diagenesis in the pore and pore geometry formation in the different successions of the

investigated core, however, the modification, trends and variability in the poro-perm relationship along the core session is facies controlled as also proposed by Goodner, (2013). LFT 5 and LFT 7 are transitional facies located on the crossplots at the boundary between clusters with high permeability and low permeability. These LFTs are found at all subsections along the core (Fig. 2.4, 4.2B). They are characterized by MFT4 and 11 with stabilized red algae and dissolved presumably originally aragonitic bioclastic allochems (up to 60 % in thin sections; Fig. 2.5) forming interparticle, intraparticle and mouldic porosity. These lithofacies types show a wide range of porosity values (30 % - 46%) with a moderate permeability (65 – 659 mD). The diversity of components suggests this facies are likely found at the reef slope (James, 2015).

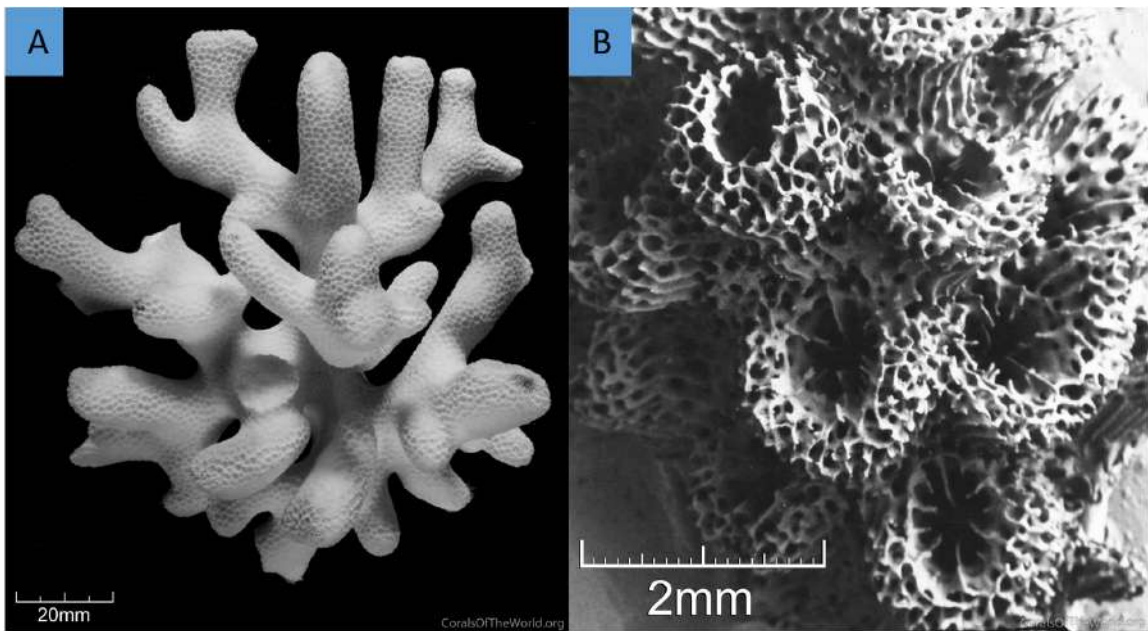


Figure 5.1 – Sample images of Porites Sp. and Millepora Sp. (A) A hand sample image of a fragment of Porites sp . (B) Sample image of Millepora sp. *Modified image from Veron and Stafford-Smith, (2016)*

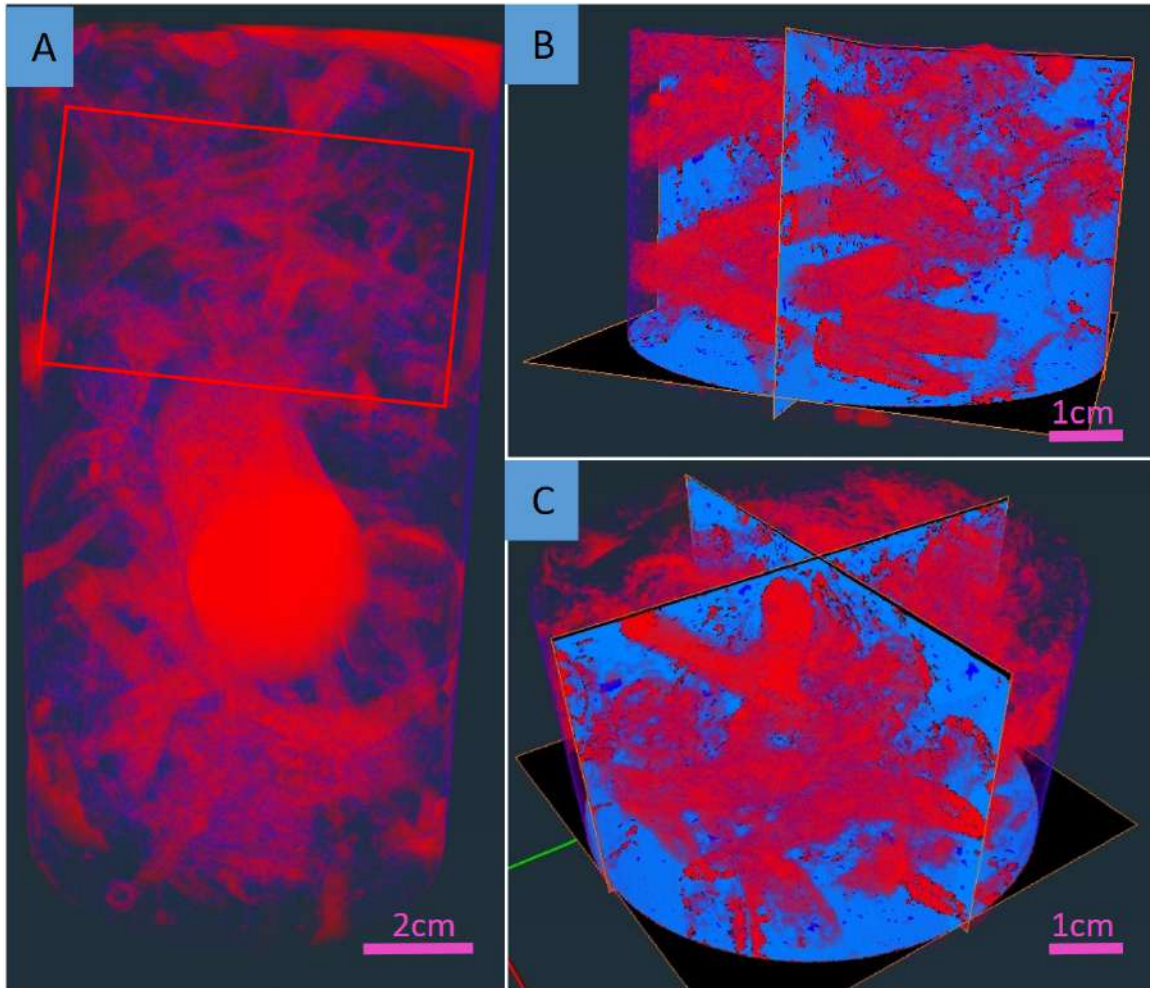


Figure 5.2 3D rendering of Corals (*Porites* Sp.) showing High K in LFT2 at 5.27-5.44 m core depth. (A) 3D rendering of core section showing the overall coral structures (Red cylinder represents drilled plug location). (B) Cropped image showing the full length of corals (*porites* Sp.) and their connectivity. (C) Image B inclined to see lateral view.

*(Porosity is indicated in red)*

### 5.2 3D visualization of Pore Types

Using the C & P pore type classification, three pore types were identified (1) Interparticle, (2) intraparticle and (3) mouldic porosity. They are present in all samples representing each subsection of the core (Fig 5.3 A-C) as observed in the thin section images (Fig. 2.5).

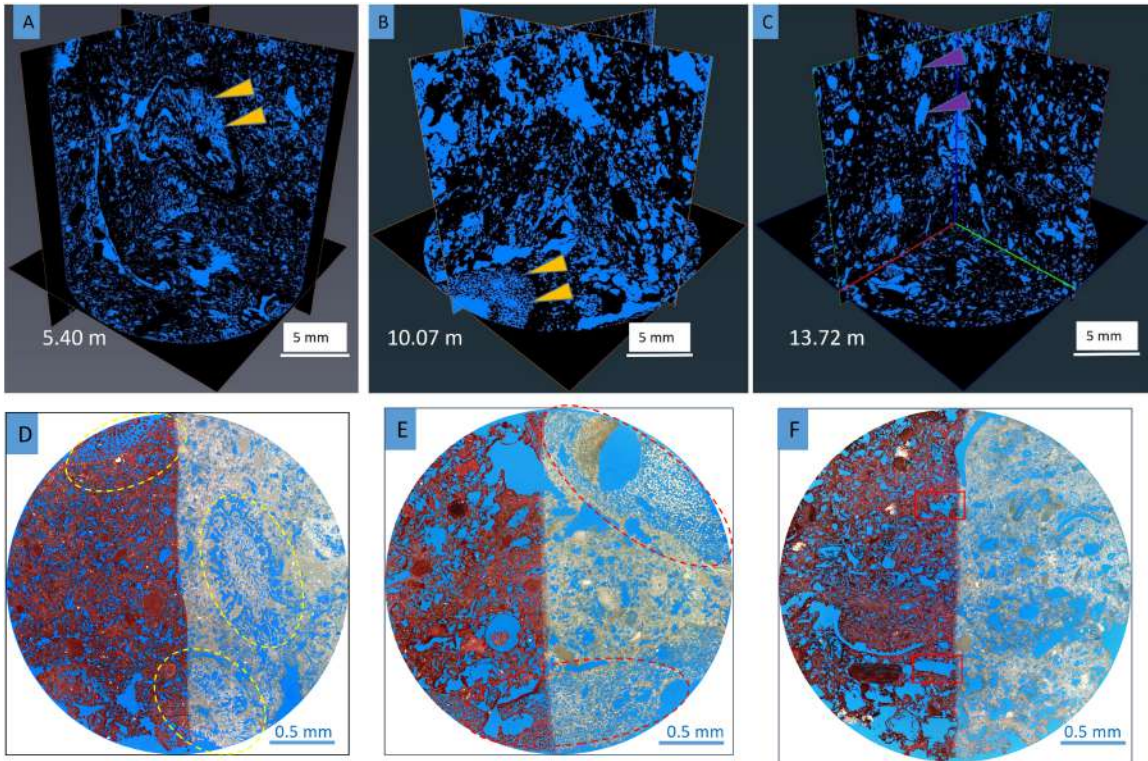


Figure 5.3 - 3D cross section of investigated core plugs showing porosity. (A) Sample 1 showing corals (*Porites Sp.*) (yellow triangles). (B) Sample 2 showing corals (*Millepora Sp.*) (orange triangles). (C) Sample 3 ( plug 6) showing bioclasts (purple triangles). (D) Thinsection from sample 1 (5.4 m) showing *porites Sp* (yellow ovals). (E) Thinsection from sample 2 (10.07 m) showing *Millepora Sp* (red ovals). (F) Thinsection from sample 3 (13.72m) showing isolated bioclast pores (red rectangle).

### 5.2.1 Intraparticle and touching vugs porosity (Sample 1 ( 5.4 m) and Sample 2 (10.07 m) )

The abundance of corals in sample 1 (5.4 m) ( MFT3) and sample 2 (10.07 m) (MFT4) characterizes them with intraparticle pore spaces of varying sizes (from  $\mu\text{m}$  to mm scales), due to the internal structure of the original skeletal grain of the corals pre-deposition (Flügel, 2010). *Porites Sp.* dominates sample 1, while *Millepora Sp.* is abundant in sample 2. The coral frameworks create megapores and smaller fragments of the corals increase

pore matrix connectivity in both samples (Fig 4.2A & B; Table 4.1) The connectivity in sample 1 and 2 (10.07 m) are significantly higher at 94% and 99% in comparison with 73.9% connectivity in sample 3 (13.72 m). This pore connectivity is enhanced by voids related to meteoric diagenesis dissolving the original aragonitic mineralogy of the corals (Fig 4.3-4.4). *Porites Sp.* is characterized by thicker inner structures (apprx. 100-120  $\mu\text{m}$  radius; Fig. 5.1A, 5.4A-C) and larger pores, while thinner walls with less pore throat sizes (apprx. 25-30  $\mu\text{m}$ ) characterizes *Millepora Sp.* (Fig 5.1B, 5.5A-C). The pore space connectivity between the outer walls of the corals and the matrix may be limited due to the possible micritic envelope around the walls of the corals. In contrast, the core plug digital pore flow measurements from the CT image data and pore network model show that the plugs are dominated by subvoxel pores (micropores) (Fig. 4.7, 4.9 & 4.12), which cannot be observed with the 20  $\mu\text{m}$  resolution for minimum detectable pore diameter of CT scans. Accurate measurements are stationed at twice the scanning resolution (Vergés et al., 2011). The significant difference (up to 27% in sample 1 and 20% in sample 2, Table 4.1) between the laboratory and CT measured porosity of these plugs can also be explained by the presence of microporosity, which is not captured within the CT scanning resolutions. Porosity in both cases measured in 1  $\text{mm}^3$  subplugs corals have porosity of approximately 50% with 100% pore connectivity. This confirms that the corals are high permeability regions and contribute significantly to the porosity and permeability of the whole cores.

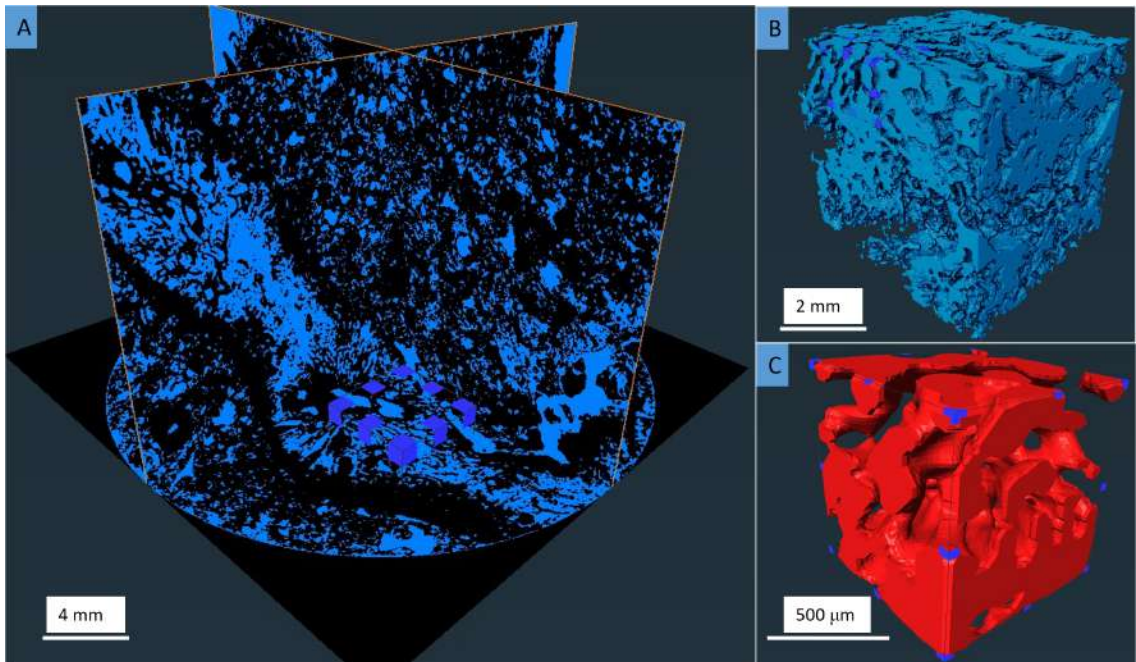


Figure 5.4 – Sample 1 (plug 1) showing the internal structure of Corals (*Porites Sp.*). (A) Plug showing the coral (*Porites Sp.*). (B) 200 x 200 x 200 pixel subplug of the investigated coral showing the high connectivity of the pore spaces. (C) a subvolume (50 x 50 x 50 pixel subplug) of the plug showing the pores and pore throats of the coral (*note, in this case red is for porosity to aid visualization*).

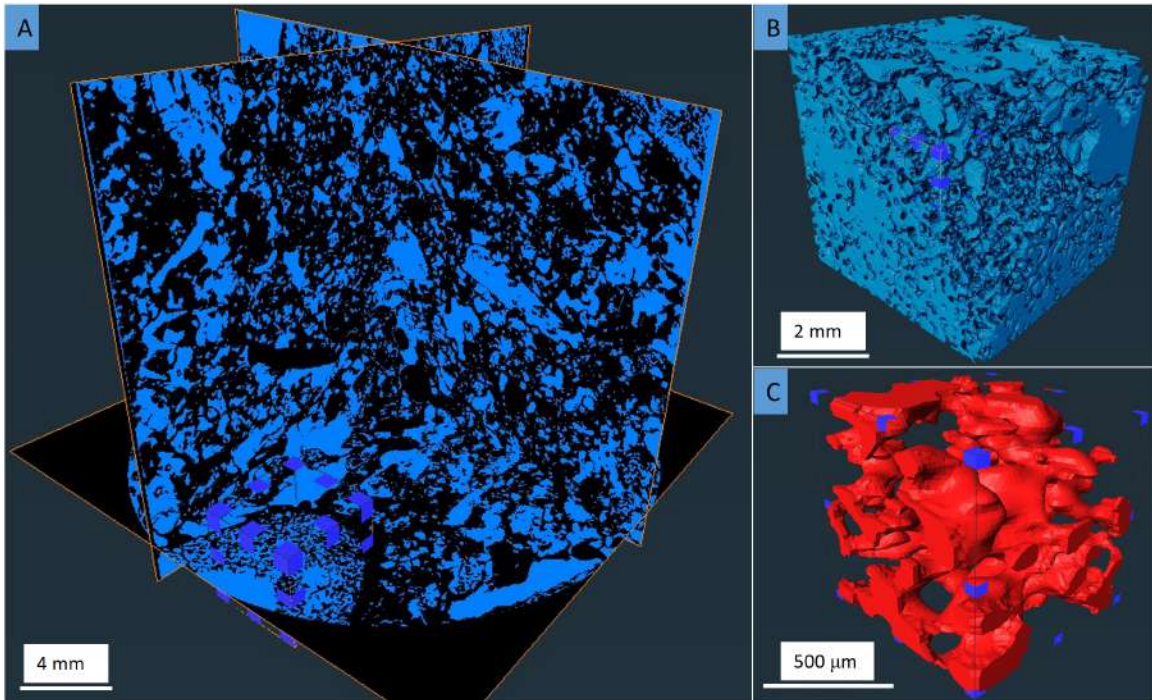


Figure 5.5 – Sample 2 (10.07 m) showing the internal structure of Corals (*Millepora Sp.*).  
 (A) Plug showing the coral (*Millepora Sp.*). (B) 200 x 200 x 200 pixel subplug of the investigated coral showing the high connectivity of the pore spaces. (C) a sub volume (50 x 50 x 50 pixel subplug) of the plug showing the pores and pore throats of the coral  
*(Red is for porosity to aid visualization)*

The matrix of sample 1 (5.4 m) and 2 (10.07 m) consist of micro, meso and megapores. from the pore properties obtained from the pore network modelling in chapter 3.4 the matrix has less connectivity (94 % and 99 %) than the high K coral regions (100 % connectivity). This further confirms the important roles of the syndepositional grains in pore and network formation.

### 5.2.2 Interparticle - Separate vugs porosity (Sample 3)

Sample 3 (MFT 4, 13.72 m) is dominated by bioclastic debris consisting mainly of shells of bivalves and gastropods. These dissolved bioclasts dominate the matrix forming mainly separate vug pores, but also interparticle porosity (Fig. 5.3C, F). This significantly affects the connectivity of the overall pore network system of the plug. Pore clusters with no connectivity to other clusters characterize sample 3 (13.72 m). The pore connectivity is limited by the high cementation that characterizes the MFT4. The matrix as well is dominated by separate non-touching vugs (Fig. 5.3C,F and 4.10B). The measured connectivity is around 73.9%. As noted this is for a cluster of pores with limited connection to the surrounding matrix. The sample is mostly dominated by bottleneck pore throats (Fig. 5.6A &B) possibly influenced by pore bridging equant and drusy calcite cements which reduces pore interaction during fluid flow significantly up to ten times more than pore filling cements (Panda & Lake, 1995) (see appendix D1).

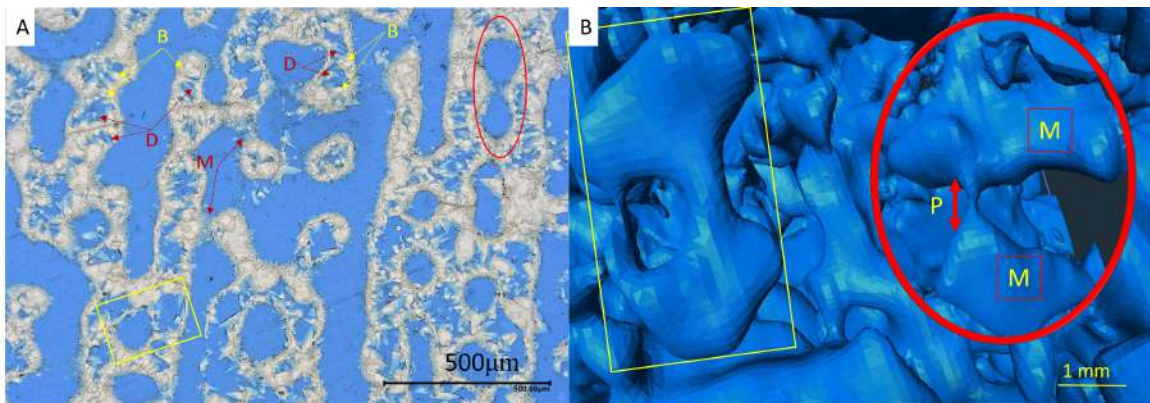


Figure 5.6 – Pore morphology. A) Thin section showing diagenetic features in core DIBH006. (B) Showing resulting pore shapes due to cementation (Yellow rectangle pore formed from pore filling cements; red sphere shows the formation of bottleneck pore throats as a result of cement precipitation). (*B* – bladed cements, *D* – dogtooth cement, *M* – meniscus cements)

### 5.3 Pore Morphology

Pore throat structure is mainly controlled by initial sediment composition/mineralogy and diagenetic processes. Based on the CT image analysis all samples investigated are characterized by centralized unimodal pore throat structure according to the classification from LI et al., (2020) (Fig. 4.7, 4.9, 4.12). However, it must be noted that the micro-CT image based pore analysis is limited to resolve pores above 20 micrometer, which is the maximum resolution of the plug CT scans. Besides, typically the pore radius distribution with respect to the depositional setting is such that in a restricted platform with intense dissolution by meteoric water leading to the formation of pore throats with different sizes. The discussion carried out from here only refers to pores above micro-CT resolution, and hence excludes the visualization of microporosity. Microporosity is observed all along the core, however, it is dominant in sections composed of LFT 5 (Fig. 4.3G) with visual estimates of more than 50% of observed total porosity. This will play a significant role in explaining the high porosity (39 %) and permeability (659 mD) measured at 16.9 m. Further imaging of sub-samples to resolve microporosity using confocal and scanning electron microscopy is work in progress, but not within the scope of the present study.

Sample 1 (5.4 m) is characterized by the highest pore size ( $> 470 \mu\text{m}$  in subplug CT PNM and  $> 1\text{cm}$  in plug image) due to the dissolution enhanced mega pores from dissolved corals and other bioclasts. It is characterized by large interparticle pores spaces with large pore throat sizes ( $> 5 \text{ mm}$ ) with low eccentricity due to low burial depth and more primary porosity (Fig. 5.7A). This indicates larger surface areas for fluid exchange, hence high permeability. Sample 2 (10.07 m) is characterized by mega pores from bioclasts and corals ( $> 400 \mu\text{m}$  in subplugs and  $> 3 \text{ mm}$  in plug) (Fig 4.8 and 5.5), with higher eccentricity and

connectivity of pores (Fig. 5.7C), due to dissolution and minor cementation. This enhances the permeability significantly. Sample 3 (13.72 m) is characterized by large and small pores but with cementation (see appendix D1, Table D.1), which results to the formation of smaller pore throats (bottleneck pores Fig. 4.5) and leading to lower permeability (Fig. 5.7B). This influences the morphology of the pores and pore throats significantly.

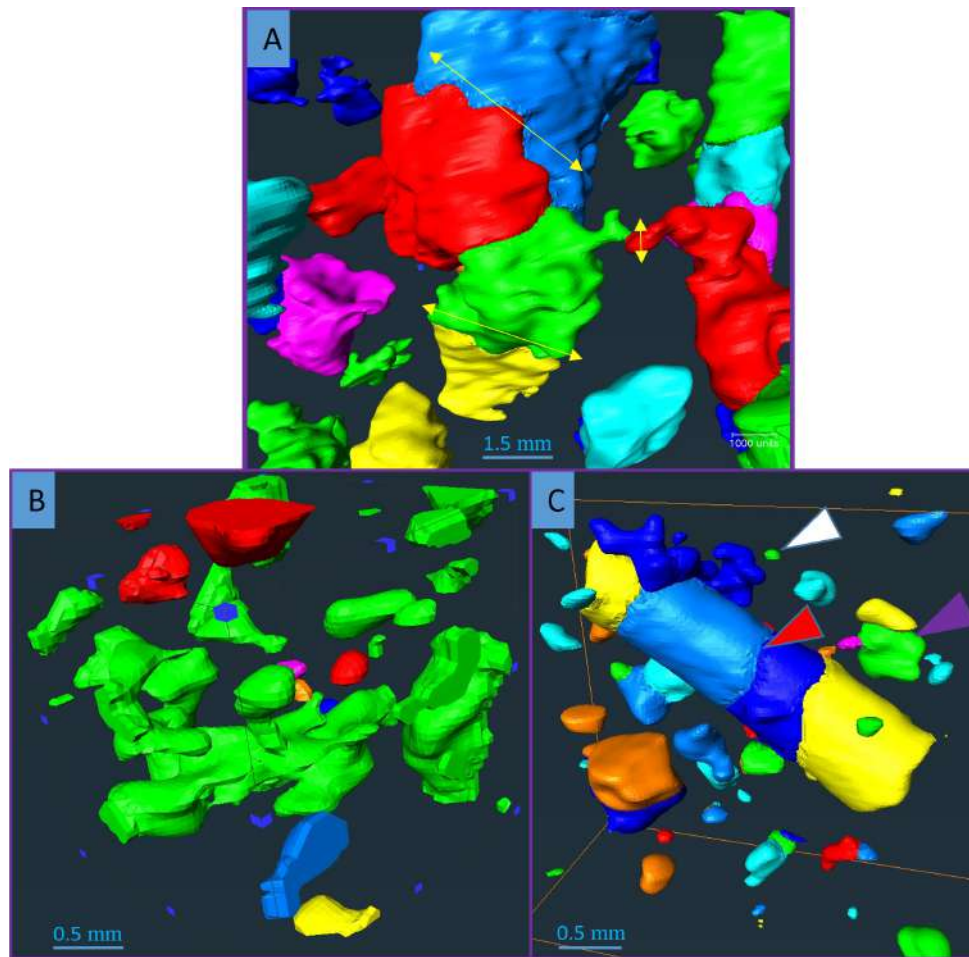


Figure 5.7 – Pore shapes and interconnectivity; (A) Sample 1 showing large pores with low eccentricity and pore throats with high connectivity (Yellow arrows indicate pore throat). (B) Sample C showing separate vugs with almost no connectivity. (C) Sample B showing pore formed from echinoderm spine with high connectivity. (*White, purple and red triangles indicate meso and mega pores respectively*).

## Chapter 6

### Conclusions

In this study, facies analysis mapping and pore characterization based on porosity-permeability (poro-perm) measurements and x-ray computed tomography were conducted. Protocols were established for CT image acquisition and processing of whole core sections and core plugs for young carbonate rocks. MS candidate, Tojo Chirakal identified Five microfacies types and seven lithofacies types were identified. Microfacies types: Porites Framestone (MFT2), Encrusted sediments covered coral framestone (MFT3), Encrusted coral rudstone (MFT4), Encrusted coral framestone (MFT5), Bioclastic packstone (MFT11). Lithofacies types: Bioclastic wackestones – packstones (LFT1), Coral Rudstones (LFT2), Bioclastic floatstone- rudstones (LFT3), Coral Floatstone-rudstone (LFT4), Red Algae bindstone (LFT5), Coral framestone (LFT6), algae-coral framestones (LFT7). LFT2, MFT3 shows the highest poro-perm values while LFT 4, MFT5 show the relatively lowest poro-perm values. Microfacies and lithofacies types dominated by corals fragments presented the highest poro-perm values, while microfacies types with less coral fragments and higher cementation presented the lowest poro-perm values. The studied reef was characterized by a very high average porosity of 41% and permeability of 804 mD. Using the Lucia (1995) pore classification three main pore types were identified:

interparticle/intraparticle pore space, touching vug and separate vug porosity. Three main pore classes according to Moore & Wade, (2013) characterized the three pore types; micropores, mesopores, and megapores. Samples with lower porosity and separate vugs were characterized by bottleneck pore throat structures due to the presence of pore bridging drusy calcitic cements. It can be concluded that meteoric diagenetic processes significantly influences the pore and pore throat morphology and connectivity. 2D images from thinsections in comparison with 3D CT plug images are not fully representative of the spatial and lateral heterogeneities associated with carbonate rocks. At such shallow depths in young carbonate sediments, the lateral and spatial heterogeneities remain predominant. As future work it is recommended to supplement the CT image analysis with confocal and SEM imagery to be able to characterize microporosity adequately. A similar analysis can be conducted for new cores from other locations on the island to characterize the combinatorial pattern of the petrophysical properties of the Shurayrah island and possibly the entire Al Wajh platform as similarly done by LI et al., (2020) for the Pre-Caspian basins.

## REFERENCES

- Algive, L., Békri, S., Nader, F. H., Lerat, O., & Vizika, O. (2012). Impact of Diagenetic Alterations on the Petrophysical and Multiphase Flow Properties of Carbonate Rocks Using a Reactive Pore Network Modeling Approach. *Oil Gas Sci. Technol. – Rev. IFP Energies Nouvelles*, 67(1), 147–160. <https://doi.org/10.2516/ogst/2011171>
- Antonellini, M., & Aydin, A. (1994). Effect of Faulting on Fluid Flow in Porous Sandstones: Petrophysical Properties. *AAPG Bulletin*, 78(3), 355–377. <https://doi.org/10.1306/BDF90AA-1718-11D7-8645000102C1865D>
- Bathurst, R. G. C. (1994). Neomorphic processes in diagenesis. *Carbonate Sediments and Their Diagenesis*, Edited by: Bathurst, RG C., 7th Edn., Elsevier, Amsterdam, 475–516.
- Betzler, C., & Eberli, G. P. (2019). Miocene start of modern carbonate platforms. *Geology*, 47(8), 771–775. <https://doi.org/10.1130/G45994.1>
- Blunt, M. J. (2017). *Multiphase flow in permeable media: A pore-scale perspective*. Cambridge University Press.
- Blunt, M. J., Bijeljic, B., Dong, H., Gharbi, O., Iglauer, S., Mostaghimi, P., Paluszny, A., & Pentland, C. (2013). Pore-scale imaging and modelling. *Advances in Water Resources*, 51, 197–216. <https://doi.org/10.1016/j.advwatres.2012.03.003>
- Bruckner, A., Rowlands, G., Riegl, B., Purkis, S. J., Williams, A., & Renaud, P. (2013). *Atlas of Saudi Arabian Red Sea Marine Habitats*.
- Buades, A., Coll, B., & Morel, J. M. (2005). A non-local algorithm for image denoising. *Proceedings - 2005 IEEE Computer Society Conference on Computer Vision and Pattern Recognition, CVPR 2005, II(0)*, 60–65. <https://doi.org/10.1109/CVPR.2005.38>
- Burns, S. J., Fleitmann, D., Matter, A., Neff, U., & Mangini, A. (2001). Speleothem evidence from Oman for continental pluvial events during interglacial periods. *Geology*, 29(7), 623–626. [https://doi.org/10.1130/0091-7613\(2001\)029<0623:SEFOFC>2.0.CO;2](https://doi.org/10.1130/0091-7613(2001)029<0623:SEFOFC>2.0.CO;2)
- Chandra, V., Petrovic, A., Khanna, P., Ramdani, A. I., Yalcin, B., Vahrenkamp, V., & Finkbeiner, T. (2021). Impact of depositional and diagenetic features on petrophysical and rock mechanical properties in Arab-D reservoir equivalent upper Jubaila Formation, Saudi Arabia. *Marine and Petroleum Geology*, 129, 105076. <https://doi.org/10.1016/j.marpetgeo.2021.105076>
- Chandra, V., Wright, P., Barnett, A., Steele, R., Milroy, P., Corbett, P., Geiger, S., & Mangione, A. (2015). Evaluating the impact of a late-burial corrosion model on

reservoir permeability and performance in a mature carbonate field using near-wellbore upscaling. *Geological Society, London, Special Publications*, 406(1), 427–445.

- Choquette, P. W., & Pray, L. C. (1970). Geologic Nomenclature and Classification of Porosity in Sedimentary Carbonates. *AAPG Bulletin*, 54(2), 207–250.  
<https://doi.org/10.1306/5D25C98B-16C1-11D7-8645000102C1865D>
- Dejam, M., Hassanzadeh, H., & Chen, Z. (2017). Pre-Darcy Flow in Porous Media. *Water Resources Research*, 53(10), 8187–8210.  
<https://doi.org/10.1002/2017WR021257>
- Ehrenberg, S. N., Nadeau, P. H., & Steen. (2009). Petroleum reservoir porosity versus depth: Influence of geological age. *American Association of Petroleum Geologists Bulletin*, 93(10), 1281–1296. <https://doi.org/10.1306/06120908163>
- El Husseiny, A., & Vanorio, T. (2017). Porosity-permeability relationship in dual-porosity carbonate analogs. *Geophysics*, 82(1), MR65–MR74.  
<https://doi.org/10.1190/geo2015-0649.1>
- Evan J. Gowan, Alessio Rovere, Deirdre D. Ryan, Sebastian Richiano, Alejandro Montes, Marta Pappalardo, and M. L. A. (2021). Last interglacial (MIS 5e) sea-level proxies in southeastern South America. *Earth System Science Data*, 171–197.  
<https://essd.copernicus.org/articles/13/171/2021/>
- Fengchao Yao, Ibrahim Hoteit, Larry J. Pratt, Amy S. Bower, Ping Zhai, Armin Kohl, G. G. (2014). Journal of Geophysical Research Oceans. *Journal of Geophysical Research: Oceans*, 119, 3868–3882. <https://doi.org/10.1002/2013JC009331>.Key
- Flannery, B. P., Deckman, H. W., Roberge, W. G., & D'AMICO, K. L. (1987). Three-dimensional X-ray microtomography. *Science*, 237(4821), 1439–1444.
- Fleitmann, D., Burns, S. J., Pekala, M., Mangini, A., Al-Subbary, A., Al-Aowah, M., Kramers, J., & Matter, A. (2011). Holocene and Pleistocene pluvial periods in Yemen, southern Arabia. *Quaternary Science Reviews*, 30(7–8), 783–787.  
<https://doi.org/10.1016/j.quascirev.2011.01.004>
- Flügel, E. (2010). Microfacies of Carbonate Rocks. In *Microfacies of Carbonate Rocks* (Issue 1971). <https://doi.org/10.1007/978-3-642-03796-2>
- Gischler, E., Dietrich, S., Harris, D., Webster, J. M., & Ginsburg, R. N. (2013). A comparative study of modern carbonate mud in reefs and carbonate platforms: Mostly biogenic, some precipitated. *Sedimentary Geology*, 292, 36–55.  
<https://doi.org/10.1016/j.sedgeo.2013.04.003>
- Grammer, G. M., Harris, P. M., & Eberli, G. P. (2001). Carbonate platforms: Exploration-and production-scale insight from modern analogs in the Bahamas. *The Leading Edge*, 20(3), 252–261.

- Hall, B. J., Gulick, S., Mccall, N., Rae, A. S. P., Morgan, J., Gebhardt, C., & Christeson, G. (2017). Dual Energy CT Scanning and Processing of Core from the Peak Ring of the Chicxulub Impact Structure: Results from IODP-ICDP Expedition 364. *Lunar and Planetary Science, XLVIII*.
- Halley, R. B., & Schmoker, J. W. (1983). High-Porosity Cenozoic Carbonate Rocks of South Florida: Progressive Loss of Porosity with Depth1. *AAPG Bulletin*, 67(2), 191–200. <https://doi.org/10.1306/03B5ACE6-16D1-11D7-8645000102C1865D>
- Hamilton Miller Goodner ( University of Kansas. (2013). *Rock Fabric Controls on Pore Evolution and Porosity-Permeability Trends in Oolitic Grainstone Reservoirs and Reservoir Analogs*. 53(9), 1689–1699.
- Hamylton, S. (2012). Hyperspectral Remote Sensing of the Geomorphic Features and Habitats of the Al Wajh Bank Reef System, Saudi Arabia, Red Sea. *Seafloor Geomorphology as Benthic Habitat*, 357–363. <https://doi.org/10.1016/B978-0-12-385140-6.00023-2>
- Harbaugh, J. W. (1967). Chapter 7 Carbonate Oil Reservoir Rocks. In G. V Chilingar, H. J. Bissell, & R. W. B. T.-D. in S. Fairbridge (Eds.), *Carbonate Rocks Origin, Occurrence and Classification* (Vol. 9, pp. 349–398). Elsevier. [https://doi.org/https://doi.org/10.1016/S0070-4571\(08\)71115-4](https://doi.org/https://doi.org/10.1016/S0070-4571(08)71115-4)
- Harris, P., & Purkis, S. (2020). Impact of facies and diagenetic variability on permeability and fluid flow in an oolitic grainstone—Pleistocene Miami Oolite. *Depositional Record*, 6(2), 459–470. <https://doi.org/10.1002/dep2.104>
- Hassan, A., Chandra, V., Yutkin, M. P., & Patzek, T. W. (2020). *3D Confocal Imaging Methodology Optimized for Pore Space Characterization of Microporous Carbonate Reservoirs* . <https://doi.org/10.2523/IPTC-19615-MS>
- Hassan, A., Chandra, V., Yutkin, M. P., Patzek, T. W., & Espinoza, D. N. (2017). *Improving Pore Network Imaging & Characterization of Microporous Carbonate Rocks Using Multi-Scale Imaging Techniques* . <https://doi.org/10.2118/188786-MS>
- Hazard, C. S., Ritter, S. M., McBride, J. H., Tingey, D. G., & KEACH II, R. W. (2017). Ground-penetrating-radar characterization and porosity evolution of an Upper Pleistocene oolite-capped depositional cycle, Red Bays, northwest Andros Island, Great Bahama Bank. *Journal of Sedimentary Research*, 87(5), 523–545.
- Hazlett, R. D. (1995). Simulation of capillary-dominated displacements in microtomographic images of reservoir rocks. *Transport in Porous Media*, 20(1–2), 21–35. <https://doi.org/10.1007/BF00616924>
- Jiang, H., Farrar, J. T., Beardsley, R. C., Chen, R., & Chen, C. (2009). Zonal surface wind jets across the Red Sea due to mountain gap forcing along both sides of the Red Sea. *Geophysical Research Letters*, 36(19), 1–6.

<https://doi.org/10.1029/2009GL040008>

- Jin, P., Bouman, C. A., & Sauer, K. D. (2015). A Model-Based Image Reconstruction Algorithm With Simultaneous Beam Hardening Correction for X-Ray CT. *IEEE Transactions on Computational Imaging*, *1*(3), 200–216. <https://doi.org/10.1109/tci.2015.2461492>
- Jones, B., & Pemberton, S. G. (1988). Lithophaga borings and their influence on the diagenesis of corals in the Pleistocene Ironshore formation of Grand Cayman Island, British West Indies. *Palaios*, *3*(1), 3–21. <https://doi.org/10.2307/3514541>
- Kronig, R. (1925). Optical Society of America Review of Scientific Instruments. *Journal of the Optical Society of America*, *12*(6), 547. <http://www.osapublishing.org/abstract.cfm?uri=josa-12-6-547>
- Langodan, S., Cavaleri, L., Vishwanadhapalli, Y., Pomaro, A., Bertotti, L., & Hoteit, I. (2017). The climatology of the Red Sea – part 1: the wind. *International Journal of Climatology*, *37*(13), 4509–4517. <https://doi.org/10.1002/joc.5103>
- Langodan, S., Viswanadhapalli, Y., Dasari, H. P., Knio, O., & Hoteit, I. (2016). A high-resolution assessment of wind and wave energy potentials in the Red Sea. *Applied Energy*, *181*, 244–255. <https://doi.org/10.1016/j.apenergy.2016.08.076>
- Leighton, Mw., & Pendexter, C. (1962). *Carbonate rock types*.
- LI, W., MU, L., ZHAO, L., LI, J., WANG, S., FAN, Z., SHAO, D., LI, C., SHAN, F., ZHAO, W., & SUN, M. (2020). Pore-throat structure characteristics and its impact on the porosity and permeability relationship of Carboniferous carbonate reservoirs in eastern edge of Pre-Caspian Basin. *Petroleum Exploration and Development*, *47*(5), 1027–1041. [https://doi.org/10.1016/S1876-3804\(20\)60114-8](https://doi.org/10.1016/S1876-3804(20)60114-8)
- Liu, N., Wang, Z. feng, Li, X. shen, Liu, L., Zhang, D. jun, You, L., Luo, W., & Liu, X. yu. (2019). Reef-carbonate diagenesis in the Pleistocene–Holocene of the well Xike#1, Xisha Islands, South China Sea: implications on sea-level changes. *Carbonates and Evaporites*, *34*(4), 1669–1687. <https://doi.org/10.1007/s13146-019-00515-1>
- Lucia, F J. (1983). Petrophysical Parameters Estimated From Visual Descriptions of Carbonate Rocks: A Field Classification of Carbonate Pore Space. *Journal of Petroleum Technology*, *35*(03), 629–637. <https://doi.org/10.2118/10073-PA>
- Lucia, F Jerry. (1995). Rock-Fabric/Petrophysical Classification of Carbonate Pore Space for Reservoir Characterization1. *AAPG Bulletin*, *79*(9), 1275–1300. <https://doi.org/10.1306/7834D4A4-1721-11D7-8645000102C1865D>
- Manaa, A. A., Jones, B. G., McGregor, H. V, Zhao, J., & Price, D. M. (2016). Dating Quaternary raised coral terraces along the Saudi Arabian Red Sea coast. *Marine Geology*, *374*, 59–72.

- Martinez, F., & Cochran, J. R. (1988). Structure and tectonics of the northern Red Sea: catching a continental margin between rifting and drifting. *Tectonophysics*, 150(1–2), 1–31. [https://doi.org/10.1016/0040-1951\(88\)90293-4](https://doi.org/10.1016/0040-1951(88)90293-4)
- McPhee, C., Reed, J., & Zubizarreta, I. (2015). Routine Core Analysis. In *Developments in Petroleum Science* (Vol. 64). <https://doi.org/10.1016/B978-0-444-63533-4.00005-6>
- Melim, L. A., Swart, P. K., & Maliva, R. G. (1995). Meteoric-like fabrics forming in marine waters: implications for the use of petrography to identify diagenetic environments. *Geology*, 23(8), 755–758. [https://doi.org/10.1130/0091-7613\(1995\)023<0755:MLFFIM>2.3.CO;2](https://doi.org/10.1130/0091-7613(1995)023<0755:MLFFIM>2.3.CO;2)
- Montaggioni, L. F., Behairy, A. K. A., El-Sayed, M. K., & Yusuf, N. (1986). The modern reef complex, Jeddah area, Red Sea: a facies model for carbonate sedimentation on embryonic passive margins. *Coral Reefs*, 5(3), 127–150. <https://doi.org/10.1007/BF00298180>
- Moore, C. H., & Wade, W. J. (2013). The nature and classification of carbonate porosity. *Developments in Sedimentology*, 67, 51–65. <https://doi.org/10.1016/B978-0-444-53831-4.00004-5>
- Nicholson, S. L., Pike, A. W. G., Hosfield, R., Roberts, N., Sahy, D., Woodhead, J., Cheng, H., Edwards, R. L., Affolter, S., Leuenberger, M., Burns, S. J., Matter, A., & Fleitmann, D. (2020). Pluvial periods in Southern Arabia over the last 1.1 million-years. *Quaternary Science Reviews*, 229. <https://doi.org/10.1016/j.quascirev.2019.106112>
- Noel P. James, B. J. (2015). Origin of carbonate sedimentary rocks. In *American geophysical union*.
- Panda, M. N., & Lake, L. W. (1995). A physical model of cementation and its effects on single-phase permeability. *AAPG Bulletin*, 79(3), 431–443.
- Petrovic Alexander, Manuel Ariza Fuentes, Liyana Nur Yahaya, Putri Indah, Pankaj Khanna1, Sam J.Purkis, V. V. (2020). Holocene sediment distribution in the Al Wajh platform lagoon (N Red Sea, Saudi Arabia), a modern analogue for large rift basin carbonate platforms. *Sedimentology*.
- Purkis, S., Casini, G., Hunt, D., & Colpaert, A. (2015). Morphometric patterns in Modern carbonate platforms can be applied to the ancient rock record: Similarities between Modern Alacranes Reef and Upper Palaeozoic platforms of the Barents Sea. *Sedimentary Geology*, 321, 49–69.
- Rankey, E. C., Goodner, H., & Doveton, J. (2018). Depositional Architecture and Petrophysical Variability of an Oolitic Tidal Sand Shoal: Pennsylvanian (Missourian), Kansas, USA Ec Rankey Et Al. PETROPHYSICAL TRENDS, PENNSYLVANIAN, KANSAS. *Journal of Sedimentary Research*, 88(9), 1114–

1131.

- Rasul, N. M. A., Stewart, I. C. F., & Nawab, Z. A. (2015). *Introduction to the Red Sea: Its Origin, Structure, and Environment* (N. M. A. Rasul & I. C. F. Stewart (eds.); pp. 1–28). Springer Berlin Heidelberg. [https://doi.org/10.1007/978-3-662-45201-1\\_1](https://doi.org/10.1007/978-3-662-45201-1_1)
- Regnet, J.-B., Robion, P., David, C., Fortin, J., Brigaud, B., & Yven, B. (2015). Acoustic and reservoir properties of microporous carbonate rocks: Implication of micrite particle size and morphology. *Journal of Geophysical Research: Solid Earth*, *120*(2), 790–811.
- Regnet, J. B., David, C., Robion, P., & Menéndez, B. (2019). Microstructures and physical properties in carbonate rocks: A comprehensive review. *Marine and Petroleum Geology*, *103*(February), 366–376. <https://doi.org/10.1016/j.marpetgeo.2019.02.022>
- Reijmer, J. J. G., Mulder, T., & Borgomano, J. (2015). *Carbonate slopes and gravity deposits*. Elsevier.
- Riegl, B. M., Bruckner, A. W., Rowlands, G. P., Purkis, S. J., & Renaud, P. (2012). Red Sea coral reef trajectories over 2 decades suggest increasing community homogenization and decline in coral size. *PLoS One*, *7*(5), e38396.
- Rios, E. H., Moss, A. K., Pritchard, T. N., Beatriz, A., Domingues, G., Bagueira, R., & Azeredo, D. V. (2015). Carbonate Nmr Permeability Estimates Based on the Winland-Pittman Micp Approach. *Society of Core Analysts*, *1*, 6–7.
- Sheppard, C., Price, A., & Roberts, C. (1992). *Marine ecology of the Arabian region: patterns and processes in extreme tropical environments*.
- Shouxiang Ma, N. R. M. (1996). Relationship between porosity and permeability in Porous Rocks. *International Symposium of the Society of Core Analysts*, PN 9610. <https://www.ux.uis.no/~s-skj/ipt/Proceedings/SCA.1987-2004/1-SCA1996-10.pdf>
- Siddall, M., Rohling, E. J., Almogi-Labin, A., Hemleben, C., Meischner, D., Schmelzer, I., & Smeed, D. A. (2003). Supplementary Information: Sea-level fluctuations during the last glacial cycle. *Nature*, *423*(June), 0–5. <https://doi.org/10.1038/nature01687.1>.
- Sok, R. M., Knackstedt, M. A., Varslot, T., Ghous, A., Latham, S., & Sheppard, A. P. (2010). Pore Scale Characterization of Carbonates At Multiple Scales: Integration of Micro-CT, BSEM, And FIBSEM. *Petrophysics - The SPWLA Journal of Formation Evaluation and Reservoir Description*, *51*(06).
- Strasser, A., Strohmenger, C., Davaud, E., & Bach, A. (1992). Sequential evolution and diagenesis of Pleistocene coral reefs (South Sinai, Egypt). *Sedimentary Geology*, *78*(1–2), 59–79. [https://doi.org/10.1016/0037-0738\(92\)90113-6](https://doi.org/10.1016/0037-0738(92)90113-6)

- Taslimi, M., Bohloli, B., Kazemzadeh, E., & Kamali, M. R. (2008). *Determining Rock Mass Permeability in a Carbonate Reservoir , Southern Iran Using Hydraulic Flow Units and Intelligent Systems*. 132–139.
- Theologou, P. N., Skalinski, M., & Mallan, R. K. (2015). An micp-based pore typing workflow – Core scale to log scale. *SPWLA 56th Annual Logging Symposium 2015*.
- Touliabah, H. E., El-Kheir, W. S. A., Kuchari, M. G., & Abdulwassi, N. I. H. (2010). Phytoplankton composition at Jeddah Coast-Red Sea, Saudi Arabia in relation to some ecological factors. *Journal of King Abdulaziz University*, 22(1), 115.
- Vergés, E., Tost, D., Ayala, D., Ramos, E., & Grau, S. (2011). 3D pore analysis of sedimentary rocks. *Sedimentary Geology*, 234(1–4), 109–115.  
<https://doi.org/10.1016/j.sedgeo.2010.12.005>
- Veron J.E.N., Stafford-Smith M.G., T. E. and D. L. M. (2016). *Corals of the world*.  
[http://www.coralsoftheworld.org/species\\_factsheets/species\\_factsheet\\_summary/porites-porites/?version=0.01](http://www.coralsoftheworld.org/species_factsheets/species_factsheet_summary/porites-porites/?version=0.01)
- Vidal, F. P., Létang, J. M., Peix, G., & Cloetens, P. (2005). Investigation of artefact sources in synchrotron microtomography via virtual X-ray imaging. *Nuclear Instruments and Methods in Physics Research Section B: Beam Interactions with Materials and Atoms*, 234(3), 333–348.
- Vollbrecht, R., & Meischner, D. (1993). Sea level and diagenesis: a case study on Pleistocene beaches, Whalebone Bay, Bermuda. *Geologische Rundschau*, 82(2), 248–262. <https://doi.org/10.1007/BF00191831>
- Wang, Y., & Sun, S. (2021). Multiscale pore structure characterization based on SEM images. *Fuel*, 289(July 2020), 119915. <https://doi.org/10.1016/j.fuel.2020.119915>
- Yang, Y., & Aplin, A. C. (2007). Permeability and petrophysical properties of 30 natural mudstones. *Journal of Geophysical Research: Solid Earth*, 112(B3).  
<https://doi.org/https://doi.org/10.1029/2005JB004243>

## 1. APPENDICES

### A – Image acquisition methodology

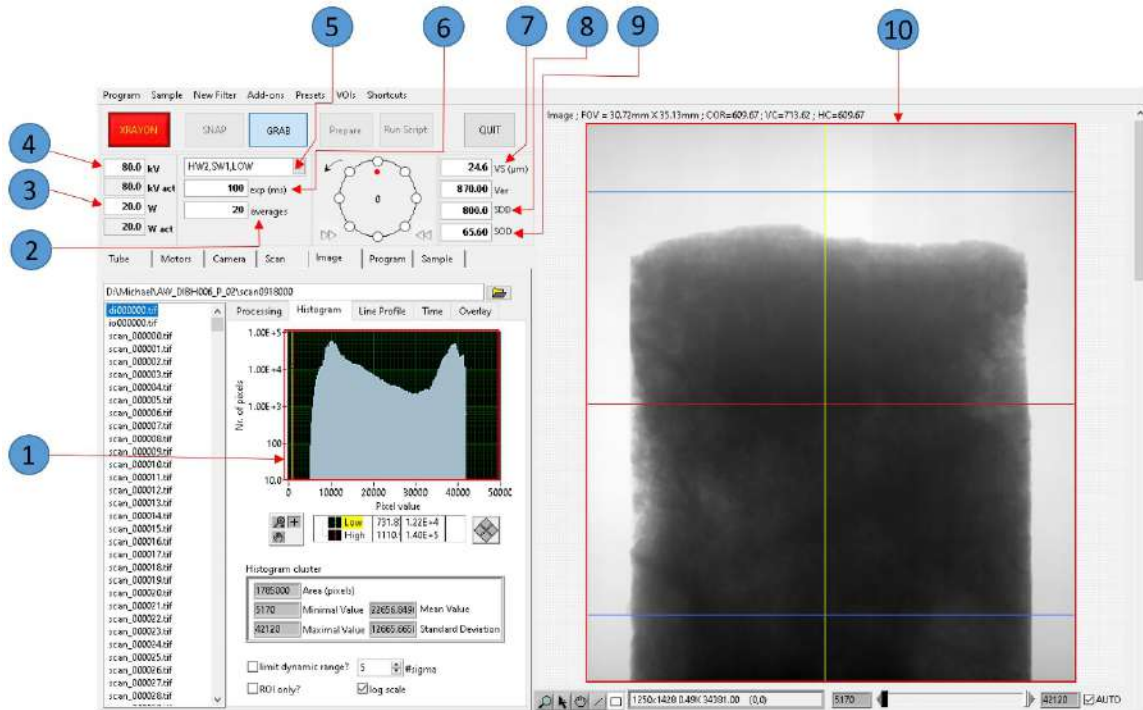


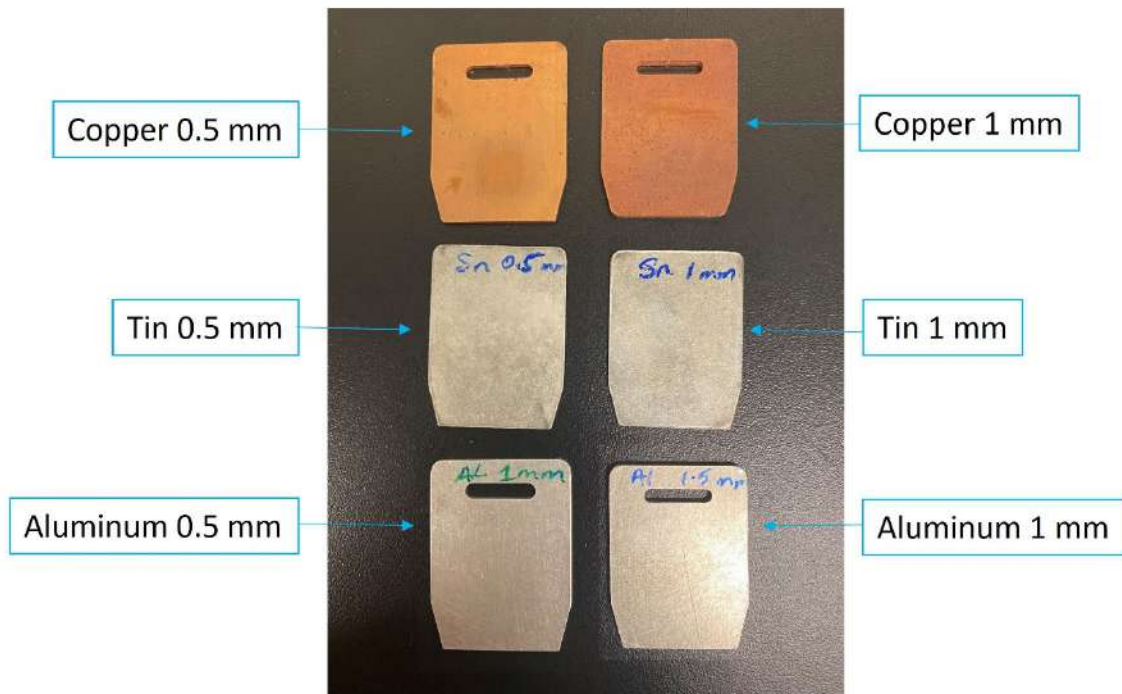
Figure A.1 – General X-ray Imaging window in Aquila.

*1 – Histogram plot of Intensity ; 2 – Number of image Averages; 3 – Power; 4 –X-ray Energy ; 5 – Detector Mode; 6 – Exposure Time ; 7 – Voxel Size; 8 - Source Detector Distance ; 9 – Source Object Distance; 10 – Frame for Projected Image*

#### *Determining optimum scanning parameters:*

After the successful loading of the sample into the chamber, the X-ray is turned on and the grab button on the Aquila software interface is selected to visualize the sample object, see the real time changes in the scanning parameters. The object is brought into the field of view (FOV) using the motors tab. To avoid the overexposure of the detector during the power amount determination, a 45000-limit count is appropriate for the primary intensity open beam image (IO), provided the desired voxel size is not attained. This is achieved by

moving the FOV outside the perimeters of the sample core section and adjusting the power to the desired value. Then the exposure time is adjusted such that the histogram plot of the intensity profile has a bulk intensity of approximately 45000 counts (A2.1). The voxel size (image resolution) is dependent on the SOD and the SDD. Depending on the material of the investigated sample, hardware (HW) filters (Fig A1.2) of various thickness are used to remove lower energy spectrum, which are attenuated easily when travelling through dense sections of the sample. The non-usage of filters can lead to thickening of the edges of the images (Beam Hardening; Jin et al., 2015), which could be erratic. The optimum scanning parameters for the image acquisition of a 115 $\mu\text{m}$  and 20  $\mu\text{m}$  voxel size are displayed in Table 2.1 and 2.2.



A.2 – CoreTOM Hardware Filters showing the different materials and their thickness

## B 3D images of processed CT images of samples from DIBH006

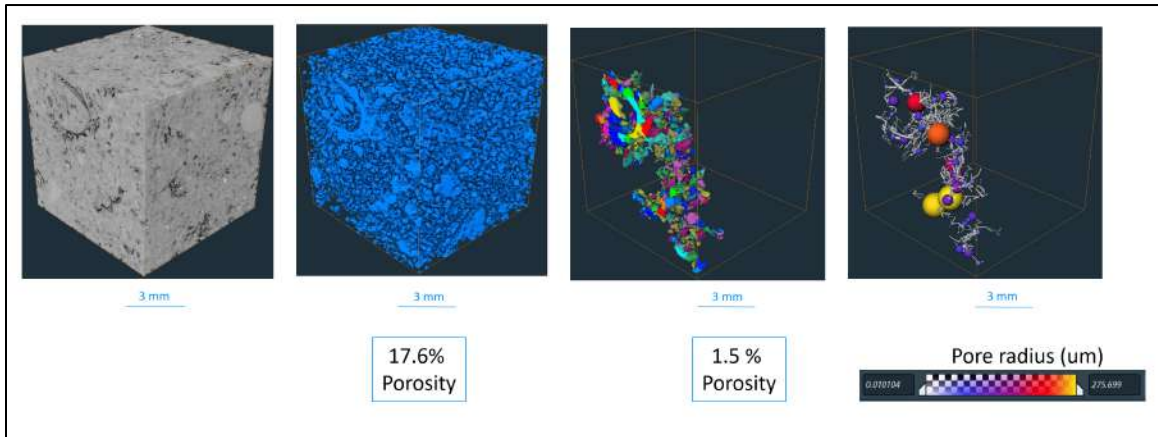


Figure B.1 – Pore structure and pore connectivity at 16.90 m depth. High porosity with low permeability and pore interactions

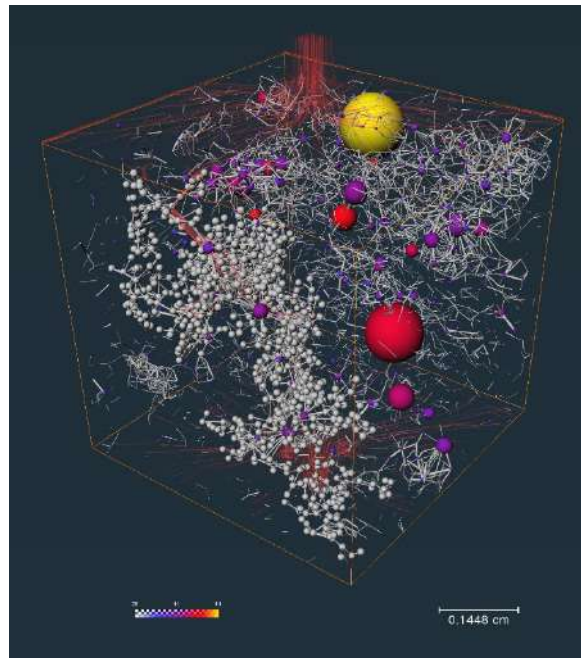
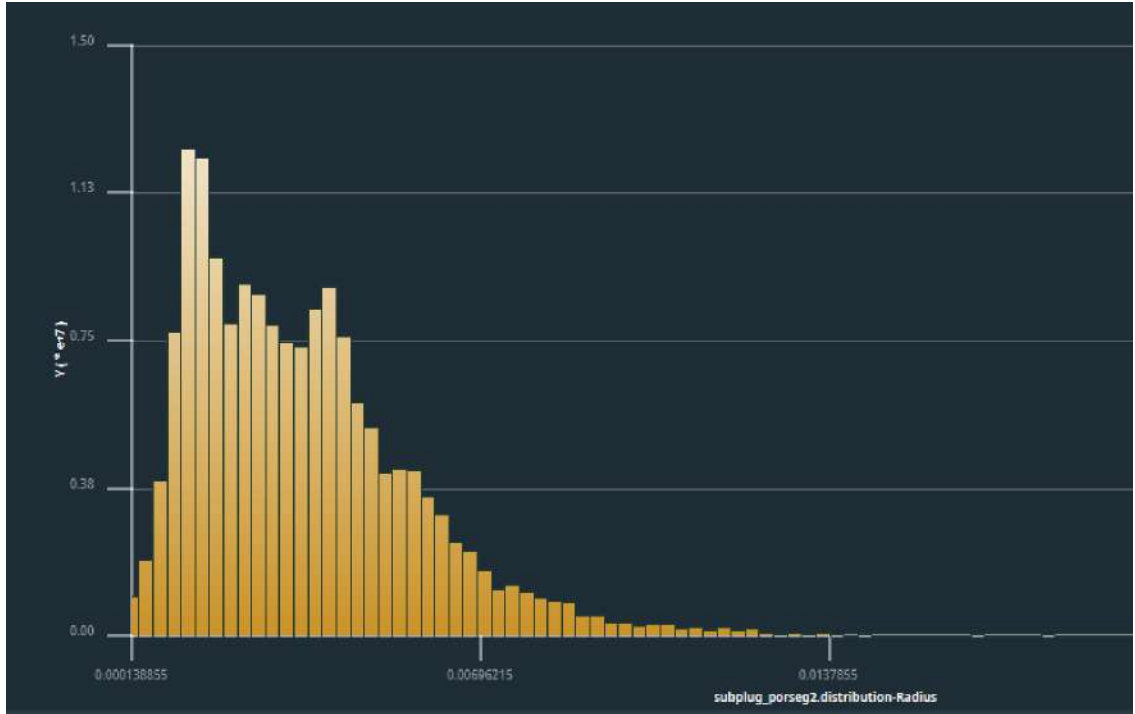
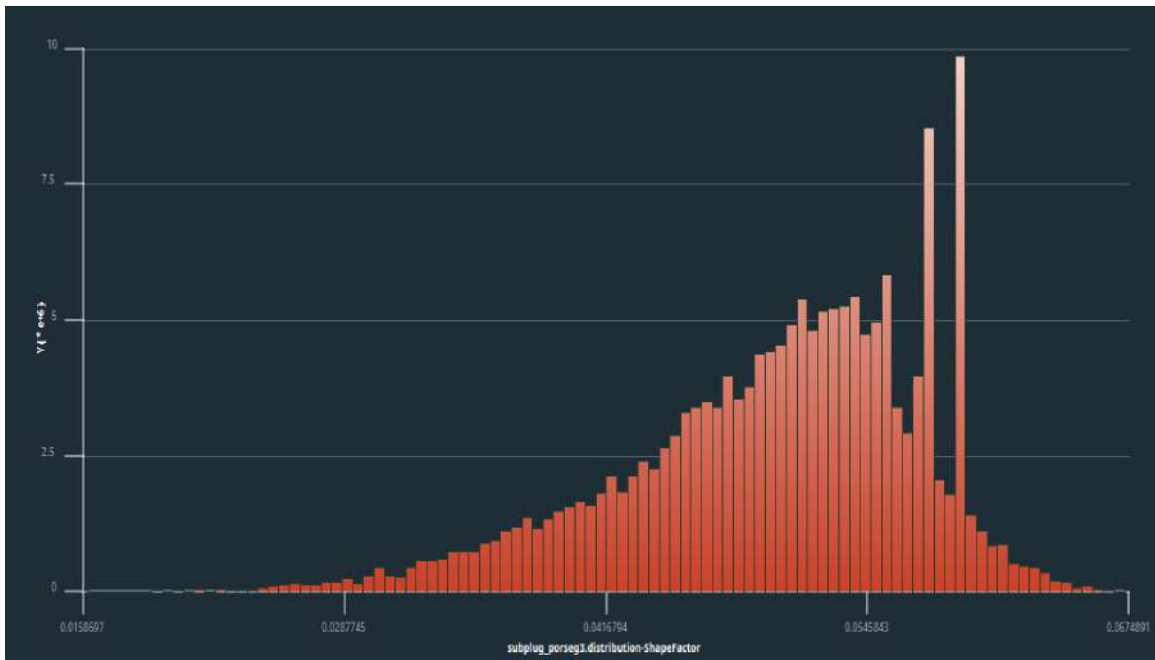


Figure B.2 – Pore structure and effective connectivity simulation of subplug from 16.90 m depth. (*High porosity with low permeability and pore interactions.*) (*red lines indicating flow lines, white line indicating pore throat skeleton*)

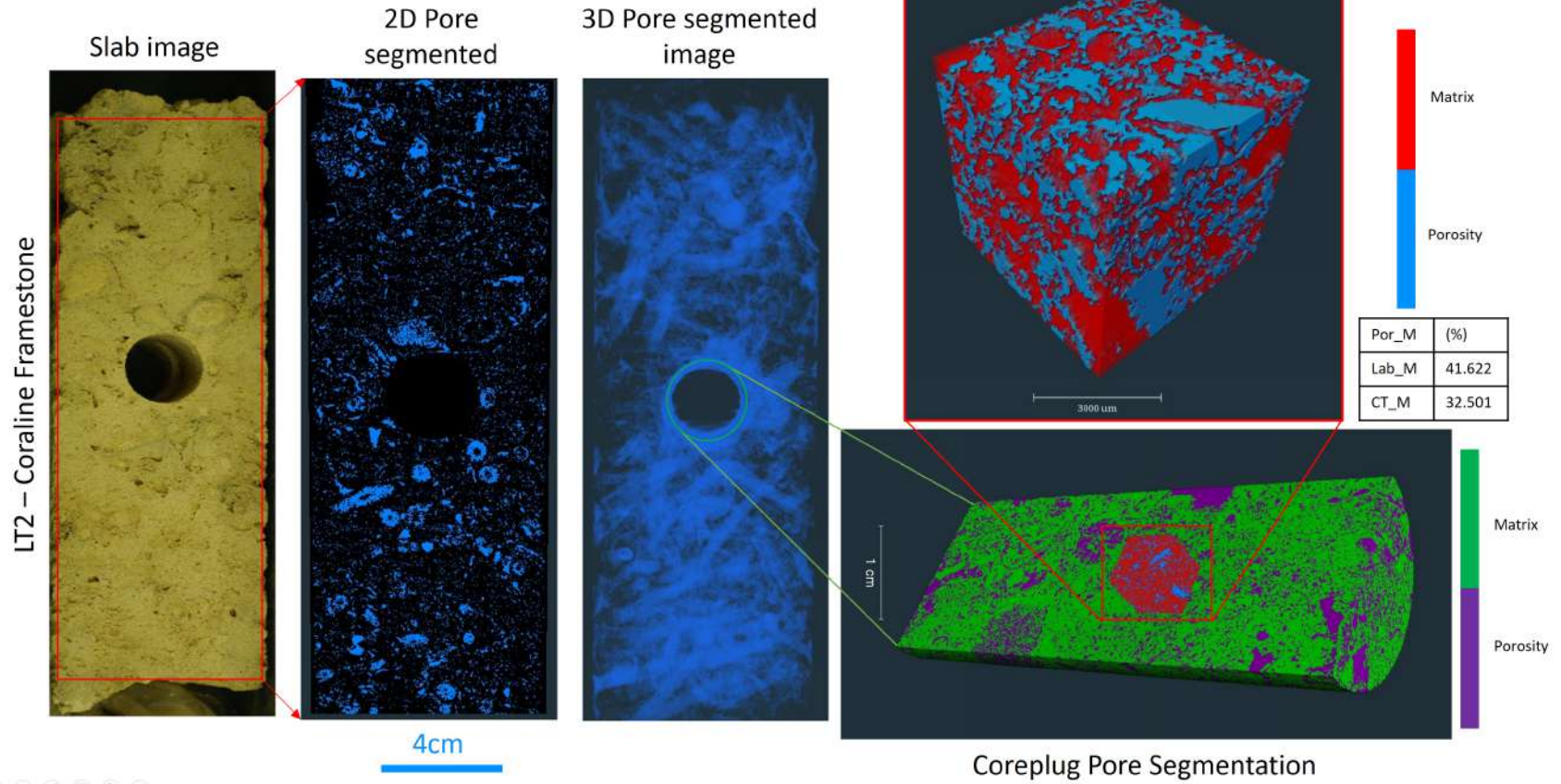


B.3 - Pore radius distribution for plug at 16.90 m depth (x- axis (cm))



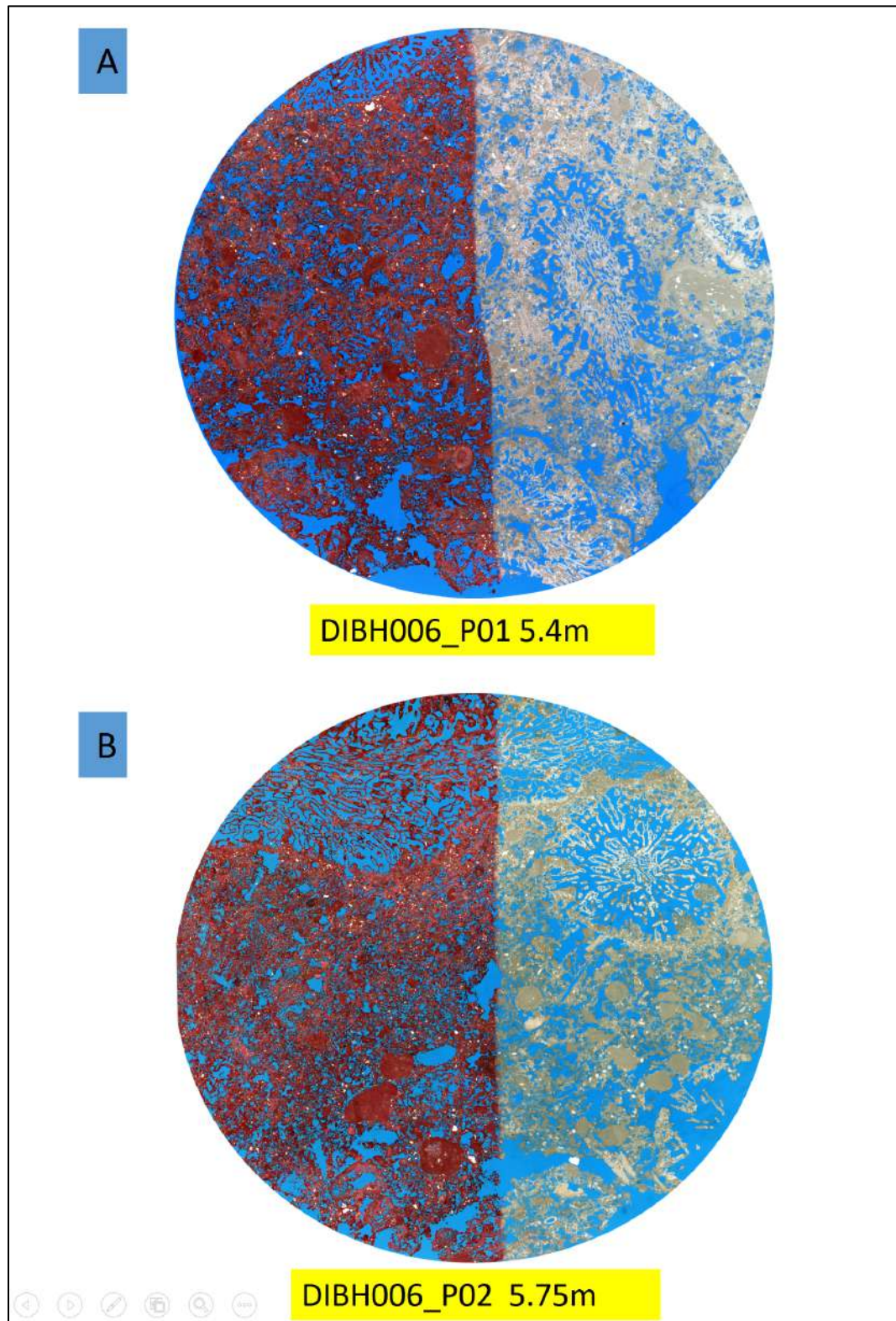
B.4 - Pore shapefactor distribution for plug at 16.90 m depth (x- axis (cm))

# AW\_DIBH006-02\_5\_75m

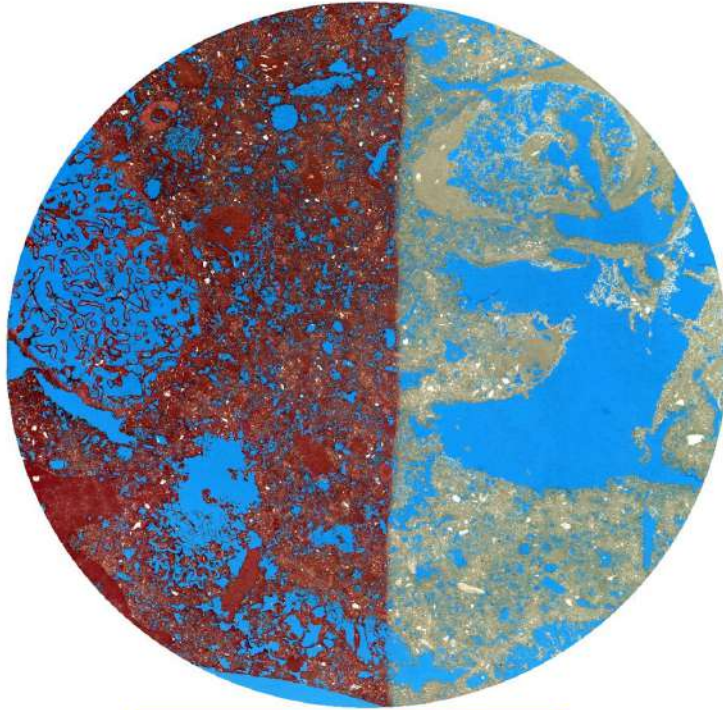


B.5 - Multiscale pore imaging of core section 5.75 m

C Thin section images of investigated coreplugs (Diameter 2.5 cm)

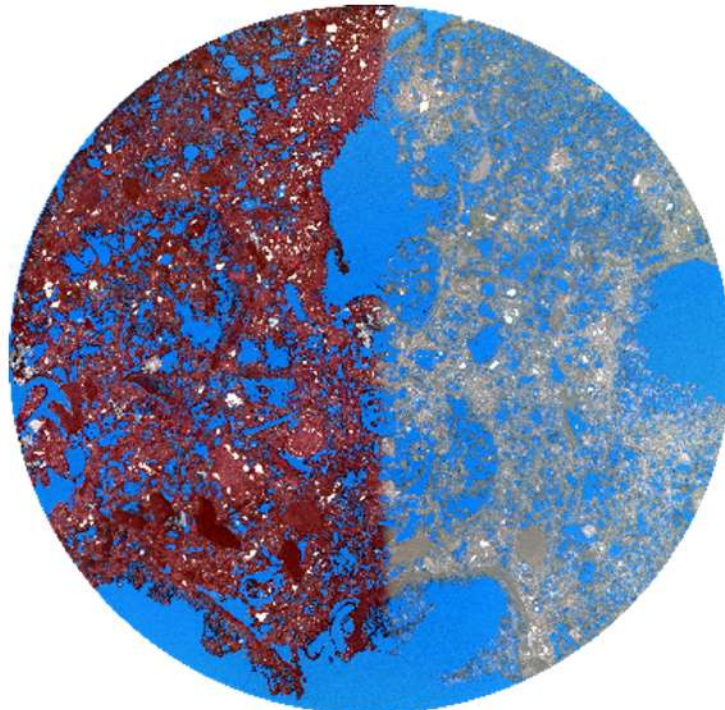


C



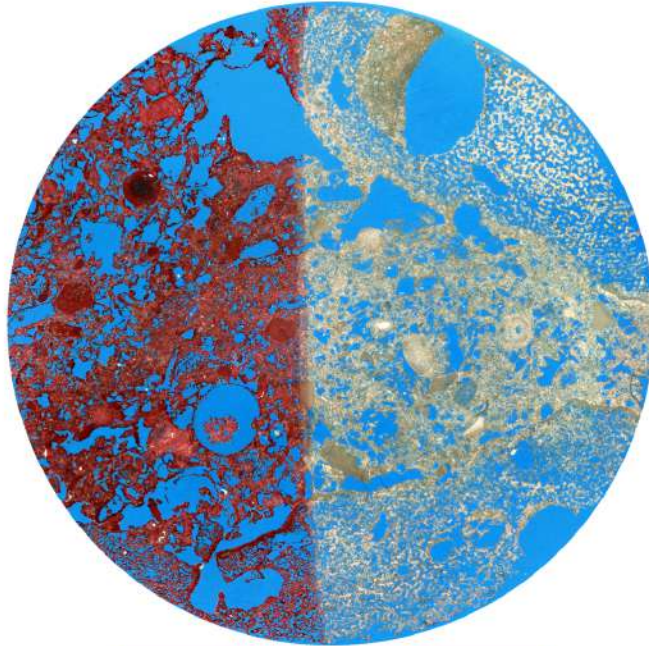
DIBH006\_P03 6.5m

D



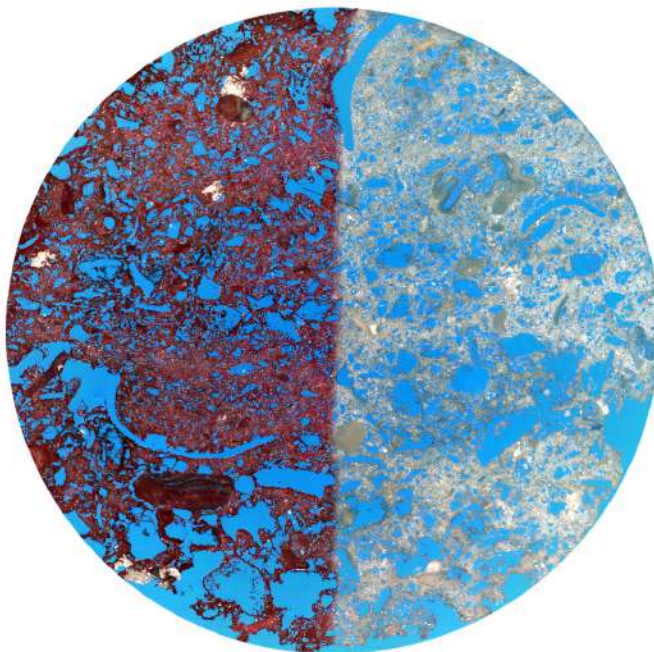
DIBH006\_P04 8.62m

E



DIBH006\_P05\_ 10.07m

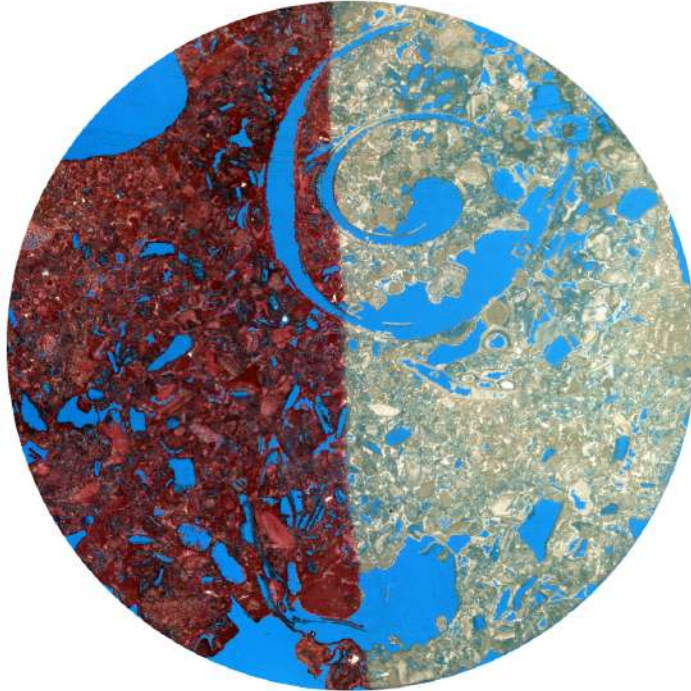
F



DIBH006\_P06 13.72m

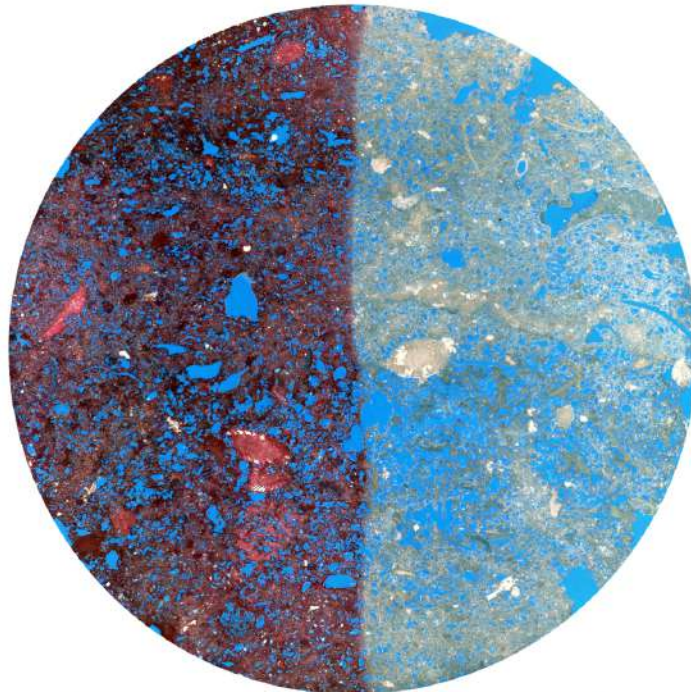


G



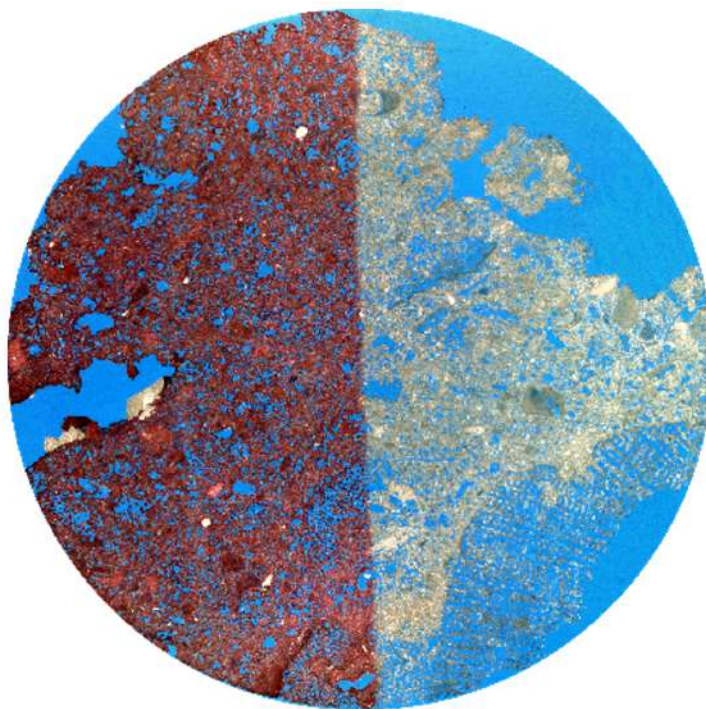
DIBH006\_P07 13.93m

H



DIBH006\_P08 15.91m

I



DIBH006\_P08 16.90m

**D – Cementation Features (16.1 m) (Chirakal, in prep.)**

**Figure D1 Thinsection showing high cementation and pore filling cements.**

*(F – foraminera, orange triangles showing pore filling cements)*

Table D.1 - Diagenetic features from thin section analysis (Chirakal, in prep.)

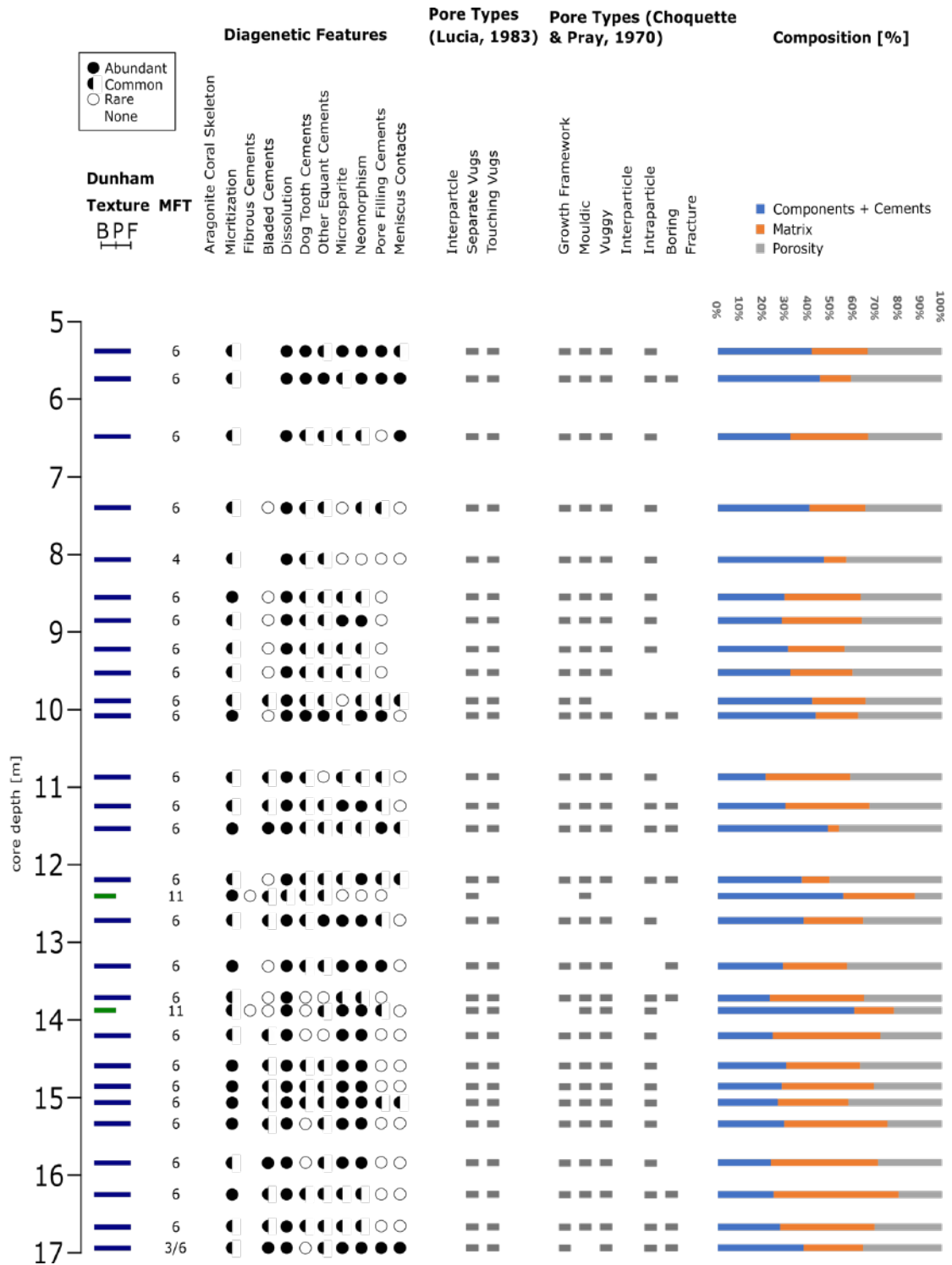


Figure 1: Diagenetic features pore types and composition of DIBH 006. Note: Certain core depths had two thin sections, resulting up to two MFT's at this particular depth. For composition and porosity, the mean values of two thin sections were plotted in this figure.